



THE UNIVERSITY OF QUEENSLAND
AUSTRALIA

Biotechnological Applications of Spider Venom Peptides

Sing Yan Er

Bachelor of Biotechnology majored in Microbial Biotechnology
(Honours)

*A thesis submitted for the degree of Doctor of Philosophy at
The University of Queensland in 2016
Institute for Molecular Bioscience*

Abstract

Spider venoms are a rich source of bioactive compounds with potential biotechnological applications. The overall aim of this project was to isolate and characterise novel spider-venom peptides (SVPs) with potential in two key areas: (1) insect control using orally active insecticidal peptides; (2) improvement of human health with peptide modulators that target acid-sensing ion channels (ASICs).

Insect pests are a worldwide problem as they threaten crop yields and spread a multitude of insect-borne diseases. Unfortunately, the armament of commercially available chemical insecticides is rapidly diminishing due to the emergence of insecticide-resistant insect strains as well as deregistrations and use restrictions by regulatory authorities due to environmental and health concerns. This has created an unmet need for new eco-friendly insecticides. Spiders are highly efficient insect predators that utilise venom to rapidly incapacitate prey. As such, many SVPs have potent insecticidal properties. However, as SVPs are injected by the spider, they are generally perceived to lack sufficient oral efficacy to be of practical agrochemical use. Recently, several orally-active insecticidal peptides (OAIP 1–5) were isolated from the venom of the Australian tarantula, *Selenotypus plumipes*, and shown to be lethal when fed to the termites. **Chapter 2** describes the characterisation and structure determination of one of these peptides, OAIP3. The peptide was produced using an efficient *E. coli* periplasmic expression system that promotes disulfide bond formation *in vivo*. The insecticidal activity of the recombinant peptide was tested in mealworms, while the structure of the peptide was solved using heteronuclear nuclear magnetic resonance spectroscopy. Structural studies indicated that OAIP3 contains a canonical inhibitor cystine knot motif commonly found in spider venom peptides. In comparison to its native form, recombinant OAIP3 is markedly less potent in mealworms, with ~53% moribund at a dose of 7.6 nmol/g. Sequence and structural homologies with other spider venom peptides indicated that OAIP3 is likely to target insect voltage-gated sodium channels.

Spider venoms are a rich source of peptides that target therapeutically-relevant ion channels such as ASICs. **Chapter 3** describes the isolation and characterisation of a novel ASIC1a modulator, Hm3a, isolated from spider venom. ASICs are proton-gated ion channels that respond to acidosis. Since their initial discovery more than a decade ago,

they have been implicated in many neurodegenerative diseases, neuronal damage resulting from ischemia, and pain. Given that spider venoms are a rich source of ion channel modulators, we screened a panel of 30 spider venoms for inhibitory activity on ASIC1a. Through an assay-guided fractionation using reverse-phase high performance liquid chromatography, we isolated a peptide modulator of ASIC1a from the venom of the tarantula *Heteroscodra maculata*. Recombinant peptide was produced and characterised using two-electrode voltage-clamp electrophysiology studies of ASICs expressed in *Xenopus laevis* oocytes. The peptide, named π -TRTX-Hm3a (Hm3a), is highly selective for ASIC1a over other ASIC subtypes. Hm3a is a close homolog of PcTx1, sharing similar electrophysiological effects on ASICs, but it proved to be more resistant to high temperatures as well as proteolytic degradation by human serum and cerebrospinal fluid. An engineered variant of Hm3a resulted in improved potency and efficacy on ASIC1a.

Since the population of ASIC1a that is therapeutically relevant is located in the brain, an efficient method of administration is needed to deliver the peptide across the blood-brain barrier. Invasive methods are often required to deliver drugs into the brain. An alternative approach is intranasal administration that bypasses the blood-brain barrier and allows direct delivery to the brain via the olfactory bulb. Thus, we hypothesised that intranasal administration may also be an effective method for delivery of ASIC1a modulators into the CNS. As described in **Chapter 4**, several engineered variants of the prototypical ASIC1a modulator, PcTx1, were produced recombinantly or chemically synthesised. These peptides were then conjugated to moieties for PET, MRI and optical imaging *in vivo*. The addition of various imaging moieties at the N-terminal of PcTx1 had minimal effect on its activity on ASICs. A pharmacokinetics and biodistribution study of PcTx1 was performed using *in vivo* PET/CT imaging and traditional *ex vivo* tissue sampling after intravenous and intranasal administration. We show that brain delivery of PcTx1 in mice can be achieved through intranasal but not intravenous administration.

In summary, the work presented in this thesis demonstrates that spider venoms provide a diverse library of peptides with potential biotechnological applications. In addition, we show that unconventional intranasal delivery is a plausible route for delivering peptide drugs to target sites in the CNS.

Declaration by author

This thesis is composed of my original work, and contains no material previously published or written by another person except where due reference has been made in the text. I have clearly stated the contribution by others to jointly-authored works that I have included in my thesis.

I have clearly stated the contribution of others to my thesis as a whole, including statistical assistance, survey design, data analysis, significant technical procedures, professional editorial advice, and any other original research work used or reported in my thesis. The content of my thesis is the result of work I have carried out since the commencement of my research higher degree candidature and does not include a substantial part of work that has been submitted to qualify for the award of any other degree or diploma in any university or other tertiary institution. I have clearly stated which parts of my thesis, if any, have been submitted to qualify for another award.

I acknowledge that an electronic copy of my thesis must be lodged with the University Library and, subject to the policy and procedures of The University of Queensland, the thesis be made available for research and study in accordance with the Copyright Act 1968 unless a period of embargo has been approved by the Dean of the Graduate School.

I acknowledge that copyright of all material contained in my thesis resides with the copyright holder(s) of that material. Where appropriate I have obtained copyright permission from the copyright holder to reproduce material in this thesis.

Publications during candidature

RESEARCH ARTICLES

Koehn L.M., Dong Q, **Er S.Y.**, Rash L.D., King G.F., Dziegielewska K.M., Saunders N.R. and Habgood M.D. (2016) Selective inhibition of ASIC1a confers functional and morphological neuroprotection following traumatic spinal cord injury. *F1000Research* **5**, 1822.

Klint, J.K., Smith, J.J., Vetter, I., Rupasinghe, D.B., **Er, S.Y.**, Senff, S., Herzig, V., Mobli, M., Lewis, R.J., Bosmans, F. and King, G.F. (2015) Seven novel modulators of the analgesic target Na_v1.7 uncovered using a high-throughput venom-based discovery approach. *British Journal of Pharmacology* **172**: 2445–2458

CONFERENCE ABSTRACTS

Er S.Y., Zoltan D., Klintzing J.R., Lau H.Y., Tesiram Y., Bhalla R., Rash L.D., King G.F. (2015) Developing PcTx1 as an imaging probe for acid-sensing ion channel 1a (ASIC1a). 7th International Peptide Symposium, Biopolis, Singapore. December 9–11 (Poster)

Er S.Y., Cristofori-Armstrong B., Escoubas P., King G.F., Rash L.D. (2015) Isolation and pharmacological characterisation of π -TRTX-Hm3a, a potent modulator of acid-sensing ion channel 1a (ASIC1a) from venom of the spider *Heteroscodra maculata*. 10th Peptide Therapeutic Symposium. Salk Institute, United States. October 22–24 (Poster)

Er S.Y., Hardy M., King G.F. (2014) Spider-venom peptides as bioinsecticides: orally active insecticidal peptides from an Australian tarantula. 5th Annual Early Career Researcher Symposium, University of Queensland, Australia. November 24 (Poster)

Er S.Y., Hardy M., King G.F. (2014) Spider-venom peptides as bioinsecticides: orally active insecticidal peptides from an Australian tarantula. 5th Venoms to Drugs Meeting, Kingscliff, Australia. October 19–24 (Poster)

Publications included in this thesis

No publications included

Contributions by others to the thesis

Chapter Two: NMR spectra collection and spectral editing of OAIP3 was Dr Mehdi Mobli (Centre for Advance imaging, Australia). Dr Mobli also provided expert guidance and opinions in chemical shift analysis and structure calculations. The insecticidal bioassay on mealworms was performed and the results were verified and recorded by Dr Volker Herzig (Institute for Molecular Bioscience (IMB), Australia).

Chapter Three: (Incorporated as manuscript for submission) Collaborative work with Mr Ben Cristofori-Armstrong (IMB) who produced the recombinant peptide, performed the electrophysiology experiments to elucidate the mechanism of actions, on-rates on ASIC1a, activity of the peptide on rASIC1a chimeras and off-targets as well as the stability of Hm3a and hANP in human CSF. The peptide sequence was provided by Dr Pierre Escoubas (VenomeTech, France). Dr Lachlan Rash (University of Queensland (UQ), Brisbane, Australia) provided expert guidance, opinions, advices and reviewed the manuscript. The manuscript was largely written by the candidate with contributions and revisions from Mr Crisotofori-Armstrong and Dr Lachlan Rash.

Chapter Four: Mr Zoltan Dekan (IMB) synthesised azPcTx1 and 1xDOTA tag as well as guided in the design and synthesis of the 4xDOTA tag and chemical coupling reactions. Dr Carus Lau (Victor Chang Cardiac Research Institute, Sydney, Australia) collected NMR spectra for the PcTx1–albumin NMR CSM experiment, analysed and interpreted the data. Dr Yas Tesiram (UQ Centre for Advanced Imaging (CAI) collected MR images of DOTA-tagged peptides and provided expert guidance in the interpretation of the data from the MR relaxation studies. Radioiodination and TLC purification of peptide was performed by A/Prof. Rajiv Bhalla (CAI). Peptide administration, PET/CT imaging, data collection, image acquisition, post mortem biodistribution and data analyses were performed jointly with Dr Karine Mardon (CAI) and/or Ms Xin Song (CAI).

Unless otherwise stated, all remaining works including sample preparation, data collections, analyses, interpretation, generation of figures, graphs and tables were performed by the candidate. In all the cases outlined above where others have contributed to work presented in this thesis, I was involved in sample preparation and assisted as much a possible in the process, thus was involved as much as practicable.

Statement of parts of the thesis submitted to qualify for the award of another degree

None

Acknowledgements

First and foremost, I would like to express my deepest gratitude to Prof. Glenn King for his guidance and support throughout these years. Thank you for introducing me to the exciting world of venom and ion channel research; providing opportunities to attend international conferences and collaborations; freedom to pursue my various research interests; meticulously reviewing both my oral and written presentations; and most importantly, creating a conducive lab which I am honoured to be a member for the past seven years.

Next I would like to thank my co-supervisor, Dr Lachlan Rash for his mentorship, taking me into the world of ASICs, oocyte electrophysiology (painful though undoubtedly useful), explaining pharmacology, and for ploughing together through the uncharted territories of peptide pharmacokinetics and imaging. Thank you for your patience, time and advice.

I would also thank Dr Maggie Hardy for her input regarding the insecticidal work and her support as a co-supervisor; Dr Mehdi Mobli for determination of OAIP3 structure; Dr Yas Tesiram, Dr Karine Mardon, A/Prof. Rajiv Bhalla, and Mr Zoltan Dekan for their help with imaging studies; Dr Amanda Carozzi and the IMB postgrad team for their support; and UQ, GSITA and IMB for scholarships and travel grants.

Special thanks to all the past and current members (too numerous to cite) of the King Group for the all help rendered over the years, invaluable advice, and daily doses of entertainment that made the lab a great place to work in. Particular thanks to the folks working in the ephys room, Lachy, Ben, Jennifer and Irene, for weekly oocyte surgery and preparation. Last, but not least, a big thanks to friends and family in Brisbane, Singapore and everywhere else for your love, trust and support

Keywords

Insecticide, Orally-active insecticidal peptide, Spider venom peptide, PcTx1, Acid-sensing ion channel, Intranasal administration, Blood–brain barrier, Two-electrode voltage clamp, Pharmacokinetics, Biodistribution

Australian and New Zealand Standard Research Classifications (ANZSRC)

ANZSRC code: 111501, Basic Pharmacology, 25%

ANZSRC code: 030403, Characterisation of Biological Macromolecules, 50%

ANZSRC code: 060110, Receptors and Membrane Biology, 25%

Fields of Research (FoR) Classification

FoR code: 1115, Pharmacology and Pharmaceutical Sciences, 25%

FoR code: 0304, medicinal and biomolecular chemistry, 50%

FoR code: 0601, Biochemistry and cell biology, 25%

Table of Content

ABSTRACT	II
DECLARATION BY AUTHOR	IV
PUBLICATIONS DURING CANDIDATURE	V
PUBLICATIONS INCLUDED IN THIS THESIS	VI
CONTRIBUTIONS BY OTHERS TO THE THESIS	VII
STATEMENT OF PARTS OF THE THESIS SUBMITTED TO QUALIFY FOR THE AWARD OF ANOTHER DEGREE	VIII
ACKNOWLEDGEMENTS	IX
LIST OF FIGURES	XV
LIST OF TABLES	XVI
LIST OF ABBREVIATIONS USED IN THE THESIS	XVII
CHAPTER ONE	1
LITERATURE REVIEW: BIOTECHNOLOGICAL APPLICATION OF SPIDER VENOMS	2
1.1 Animal venoms in biotechnology	2
1.2 Venom diversity and composition	2
1.3 Spider venoms as a source for novel peptides	3
1.4 The need for new insecticides	3
1.5 Problems with current insecticides	4
1.6 Natural products as bioinsecticides	6
1.7 Venom peptides as bioinsecticides	6
1.8 Venom peptides as therapeutic leads	7
1.9 Acid-Sensing Ion Channels (ASICs)	8
1.10 Overall electrophysiological properties and structure of ASICs	9
1.11 Modulation of ASICs	11
1.12 ASICs as analgesic target	15
1.13 ASIC modulation for neuroprotection	17
1.14 Targeting ASICs for the treatment of neurological diseases	19
1.15 ASICs as molecular target for cancer therapeutics	20
1.16 Hurdle of CNS drug delivery — The blood-brain barrier	21
1.17 Methods to overcome the blood brain barrier	23
1.18 Intranasal administration as alternative for CNS drug delivery	24
1.19 Mechanisms of CNS delivery via intranasal administration	25
AIMS OF PHD PROJECT	27
Overall aim:	27
Specific aims:	27
CHAPTER TWO	28

FUNCTIONAL AND STRUCTURAL CHARACTERISATION OF AN ORALLY ACTIVE INSECTICIDAL PEPTIDE 3 (OAIP3) ISOLATED FROM THE VENOM OF THE AUSTRALIAN FEATHERLEG TARANTULA, <i>SELENOTYPUS</i> <i>PLUMIPES</i> -----	29
2.1 Introduction -----	29
2.2 Materials and Methods-----	31
2.2.1 Bacterial transformation, recombinant expression and purification of OAIP3 -----	31
2.2.2 Structure determination-----	32
2.2.3 Insecticidal assay -----	33
2.2.4 Mass spectrometry -----	34
2.3 Results -----	34
2.3.1 Recombinant expression of OAIP3-----	34
2.3.2 NMR structure determination-----	36
2.3.3 Sequence and structural homologs of OAIP3 -----	39
2.3.4 Insecticidal activity of recombinant OAIP3-----	43
2.4 Discussion-----	44
2.4.1 Production of recombinant OAIP3 -----	44
2.4.2 Determination of the 3D structure of OAIP3-----	45
2.5 Conclusions-----	46
CHAPTER THREE-----	48
DISCOVERY, MOLECULAR INTERACTION AND STABILITY STUDIES OF A SECOND ACID-SENSING ION CHANNEL 1 MODULATOR FROM TARANTULA VENOM -----	49
ABSTRACT -----	50
RESULTS AND DISCUSSION-----	52
Identification and Purification of Hm3a-----	52
Recombinant Production of Hm3a -----	54
Effects of Hm3a on ASICs -----	55
The mechanism of action of Hm3a on ASIC1 -----	58
Characterizing the molecular interactions involved in subtype and species selectivity of Hm3a on ASIC1-----	61
Stability of Hm3a and PcTx1 -----	64
METHODS -----	67
Venom Peptide Purification and Characterization-----	67
RP-HPLC and MALDI-TOF Mass Spectrometry.-----	67
Peptide Sequencing -----	68
Production of Recombinant Hm3a -----	68
Electrophysiology-----	68
Stability Assays -----	69
Deposition of Protein and cDNA Sequence Information.-----	70

Materials	70
Animal Welfare and Ethics Statement.	70
Data Analysis and Statistical Procedures	70
ASSOCIATED CONTENT	72
CHAPTER FOUR	77
ELUCIDATING THE PHARMACOKINETICS AND BIODISTRIBUTION OF PcTx1 FOLLOWING INTRAVENOUS AND INTRANASAL ADMINISTRATION	78
4.1 Introduction	78
4.2 Materials and Methods	82
4.2.1 Recombinant expression and purification of PcTx1 and Tyr _N PcTx1	82
4.2.2 Solid-Phase Peptide Synthesis of AHA-PcTx1 (azPcTx1)	82
4.2.3 Synthesis of alkyne DOTA (1,4,7,10-tetraazacyclododecanetetraacetic acid) tags	83
4.2.4 Azide-alkyne Huisgen cycloaddition	84
4.2.5 Relaxation studies of DOTA-labelled peptides	84
4.2.6 Iodination of Tyr _N PcTx1	85
4.2.7 Two-electrode voltage clamp electrophysiology (TEVC)	85
4.2.8 Thermal, serum and cerebrospinal fluid stability assay	86
4.2.9 Iodine-124 iodination and TLC purification	86
4.2.10 in vivo PET/CT imaging	86
4.2.11 Post mortem biodistribution study	88
4.2.12 Reversed-phase high performance liquid chromatography	88
4.2.13 Mass determination	89
4.2.14 Animals	89
4.3 Results	89
4.3.1 Recombinant expression and purification of PcTx1 variants	89
4.3.2 Chemical synthesis of azPcTx1	91
4.3.3 Synthesis, derivatisation and bioconjugation of imaging moieties	92
4.3.4 Iodination of PcTx1	94
4.3.5 Longitudinal (T ₁) and transverse (T ₂) relaxation of Gd ³⁺ loaded DOTA-azPcTx1	96
4.3.6 Activity of labelled PcTx1 variants on rASIC1a and hASIC1a	97
4.3.7 Stability profile of PcTx1	98
4.3.8 Interaction between PcTx1 and serum albumin	98
4.3.9 Radiolabelling of Tyr _N PcTx1	101
4.3.10 Pharmacokinetics of ¹²⁴ I-PcTx1 after intravenous administration	101
4.3.11 Pharmacokinetics of ¹²⁴ I-PcTx1 after intranasal administration	104
4.4 Discussion	106
4.4.1 Production and characterisation of labelled PcTx1 variants for PET, MRI and fluorescence imaging	106

4.4.2	Stability of PcTx1-----	108
4.4.3	Interaction with serum albumin-----	109
4.4.5	Pharmacokinetics of PcTx1-----	111
4.5	Conclusion-----	114
CHAPTER FIVE	-----	115
	FINAL CONCLUSION AND FUTURE DIRECTIONS-----	116
	Development of OAIPs as bioinsecticides-----	116
	Development of spider venom peptides as therapeutics-----	117
	REFERENCES-----	119

List of Figures

Figure 1.1: Evolutionary timeline of selected venomous animals.....	3
Figure 1.2: Total number of insecticide resistance cases grouped according to molecular target.....	5
Figure 1.3. Properties of ASICs.....	11
Figure 1.4. Schematic of the pain signalling pathway in humans.....	16
Figure 1.5. Schematic of the BBB endothelium.....	22
Figure 1.6. Anatomy of the human nasal cavity.....	26
Figure 1.7. A schematic of the pathways to CNS following intranasal administration.....	26
Figure 2.1. Expression and purification of recombinant OAIP3.....	35
Figure 2.2. 2D ¹ H- ¹⁵ N HSQC spectrum of OAIP3 acquired at 900 MHz. Peaks are labelled according to the residue number of OAIP3.....	38
Figure 2.3. NMR solution structure of OAIP3.....	39
Figure 2.4. Sequence alignment of OAIP3 with orthologs from other spider venoms.....	41
Figure 2.5. Structural homologs of OAIP3.....	42
Figure 2.6. Insecticidal activity of OAIPs in mealworms and termites.....	43
Figure 3.1. Isolation of Hm3a from <i>H. maculata</i> venom.....	54
Figure 3.2. Production of recombinant Hm3a.....	55
Figure 3.3. Concentration-effect curves of Hm3a.....	58
Figure 3.4. The mechanism of action of Hm3a on rASIC1.....	61
Figure 3.5. Molecular interactions involved in species and subtype selectivity.....	63
Supplementary figure 3.1. Trace of Hm3a on rASIC1a and IC ₅₀ curves of PcTx1 vs Hm3a.....	64
Supplementary figure 3.2. Act and SSD curves for channel mutants.....	64
Figure 3.6. Comparative stability studies of Hm3a and PcTx1.....	65
Supplementary figure 3.2: The effect of Hm3a on the voltage dependence activation of voltage-gated ion channels.....	66
Supplementary figure 3.3: HPLC profile of PcTx1 following incubation in human serum.....	66
Figure 4.1. Recombinant expression and purification of Tyr _N -PcTx1.....	90
Figure 4.2 Synthesis of azPcTx1.....	91
Figure 4.3. Schematic of 1xDOTA and 4xDOTA synthesis.....	93
Figure 4.4. Labelling of azPcTx1 with various imaging moieties.....	94
Figure 4.5. Iodination of Tyr _N -PcTx1.....	95
Figure 4.6: Nuclear relaxation of PcTx1 at 9.4 T.....	97
Figure 4.7. Concentration-effect curves for inhibition on rat and human ASIC1a.....	98
Figure 4.8. ITC experiment of PcTx1 and BSA interaction.....	99
Figure 4.9. NMR CSM experiment of PcTx1 and BSA interaction.....	100
Figure 4.10. Residue of PcTx1 affected by BSA titration.....	100
Figure 4.11. Radioiodination of Tyr _N -PcTx1.....	101
Figure 4.12 Pharmacokinetics of ¹²⁴ I-PcTx1 following IV administration.....	103
Figure 4.13. Uptake (%ID/g) of ¹²⁴ I-PcTx1 after IN administration.....	105
Supplementary Figure. 4.1. Influence of BSA on PcTx1 inhibition of rASIC1a.....	110
Figure 4.14. Interaction between residues of the PcTx1 pharmacophore and Helix 5 of cASIC1.....	111

List of Tables

Table 1.1: Venom-derived compounds in clinical trials or approved by the FDA.....	8
Table 1.2: Summary of ASIC subtypes.....	9
Table 1.3: Summary of ASIC modulators isolated from animal venoms.....	14
Table 2.1: Statistics for the OAIP3 structure.....	40
Table 4.1: Comparison of PET, MRI and NIR imaging	81
Table 4.2: IC ₅₀ values for inhibition of rASIC1a by PcTx1 and Tyr _N PcTx1	95
Table 4.3: Summary of the longitudinal and transverse relaxation times	96
Table 4.4: Formulation strategies for improving absorption across the nasal epithelium	113

List of Abbreviations used in the thesis

%ID/g	Percentage of injected dose per gram
DOTA	1,4,7,10-tetraazacyclododecanetetraacetic acid
ACT	Activation
ASICs	Acid-sensing ion channels
ATP	Adenosine triphosphate
BBB	Blood–brain barrier
BgNav _v 1	<i>Blattella germanica</i> voltage-gated sodium channel
BSA	Bovine serum albumin
BT	<i>Bacillus thuringiensis</i>
CED	Convection enhanced diffusion
CHCA	α -cyano-4 hydroxycinnamic acid
CNS	Central nervous system
CSF	Cerebrospinal fluid
CSM	Chemical shift mapping
CT	X-ray computed tomography
CuAAC	Azide-alkyne Huisgen cycloaddition
DEG	Degenerin
DIEA	N,N-Diisopropylethylamine
DRG	Dorsal root ganglion
DUM	Dorsal unpaired median
EB	Equilibration Buffer
EC ₅₀	Concentration of a drug that gives half-maximal response
ENaC	Epithelial sodium channel
EPA	Environmental Protection Agency (United States)
ESI	Electron-spray ionisation
FCA	Freud's complete adjuvant
FOV	Field-of-view
GABA	γ -aminobutyric acid
Gd	Gadolinium
GMQ	2-Guanidine-4-methylquinazoline
hERG	Voltage-gated potassium (K _v) channel K _v 11.1
HSQC	Heteronuclear single quantum coherence
IASP	International Association for the Study of Pain

IC ₅₀	Concentration of an inhibitor where the response is reduced by half
ICK	Inhibitor cysteine knot
ICV	Intracerebroventricular
IN	Intranasal
IGF	Insulin-like growth factor
ITC	Isothermal calorimetry
IV	Intravenous
LB	Lysogeny broth
MALDI-TOF	Matrix-assisted laser desorption/ionisation time-of-flight
MBP	Maltose-binding protein
MS	Mass spectrometry
m/z	Mass-to-charge ratio
MRI	Magnetic resonance imaging
nAChR	Nicotinic acetylcholine receptor
Na _v	Voltage-gated sodium channel
NMR	Nuclear magnetic resonance
NOESY	Nuclear Overhauser effect spectroscopy
OAIP	Orally active insecticidal peptide
OEC	Olfactory ensheathing cell
OSN	Olfactory sensory neuron
PD ₅₀	Dose that paralysed 50% of injected subjects
PET	Positron emission tomography
PNS	Peripheral nervous system
RGC	Retinal ganglion cell
ROI	Region-of-interest
RP-HPLC	Reversed-phase high-performance liquid chromatography
SPAAC	Strain-Promoted [3 + 2] Azide–Alkyne Cycloaddition
SPPS	Solid-phase peptide synthesis
SSD	Steady-state desensitisation
SVP	Spider venom peptide
TAC	Time–activity curve
TEV	Tobacco Etch Virus
TEVC	Two-electrode voltage-clamp
TOCSY	Total correlation spectroscopy
WHO	World Health Organisation

Chapter One

Literature Review: Biotechnological application of spider venoms

1.1 Animal venoms in biotechnology

Biotechnology, simply defined, is the manipulation of microorganisms or biological substances to develop or improve products for the benefit of human lives or the environment. Since early civilisation, humans have harnessed the biotechnological potential of animal venoms for varied and seemingly contradictory purposes. Indigenous people lace weapons with venoms or poisonous secretions from animals to improve the efficiency of their hunting. Conversely, animal venoms have been prescribed for millennia in traditional medicines to treat many diseases and ailments. Interestingly, the detailed study of animal venoms in the last century has identified many bioactive components that may indeed be beneficial for the treatment of pain and other ailments. My thesis covers the potential biotechnological potential of venoms with a focus on use of spider-venom peptides (SVPs) as bioinsecticides and pharmacological tools (with a view to therapeutic agent development). This thesis also addresses issues that may limit the use of SVPs for their intended purpose as well as potential solutions to overcome these limitations.

1.2 Venom diversity and composition

Over the course of evolution (**Fig. 1.1**), animals have developed venoms for predation, defence and competitor deterrence¹. The ability to use venom is clearly advantageous, as indicated by the diverse range of animals that have independently developed venom systems. Venoms are typically injected directly into tissues through various apparatuses such as fangs, stingers and harpoons. Venoms contain a cocktail of biologically active compounds such as proteins (> 10 kDa), peptides (3–10 kDa), small organic molecules (< 1 kDa), and inorganic compounds². The combination of advanced separation and sequencing technologies employed in proteomics and transcriptomics analyses have highlighted the complexity of these animal venoms³. Venom peptides have evolved to be target specific molecular targets with high levels of potency and selectivity⁴⁻⁵. The incredible pharmacological diversity, complexity and potency of animal venoms has led to an explosion of venomics-based research and discovery programs for biotechnological applications such as the development of bioinsecticides and therapeutic agents⁶⁻¹⁰.

1.3 Spider venoms as a source for novel peptides

Based on their vast species diversity and the wide range of habitats in which they reside, spiders are the most successful group of venomous animals (**Fig. 1.1**) with highly complex venoms containing up to a thousand distinct peptides^{2, 11}. The majority of SVPs are small (3–8 kDa) and contain disulfide-rich scaffolds that provide excellent chemical, thermal and proteolytic stability^{2, 11-12}. The most common SVP structural scaffold is the inhibitor cystine knot (ICK) motif that is comprised of two antiparallel β -strands connected by a network of three disulfide bonds. Two of the disulfide bonds and the intervening sections of the peptide backbone form a ring while the third disulfide bond pierces the ring to form a pseudo-knot that stabilises the peptide structure¹³. Due to their relatively small molecular weight, potency and structural stability, spider venoms are a rich source of compounds with impressive biotechnological potential⁹⁻¹⁰.

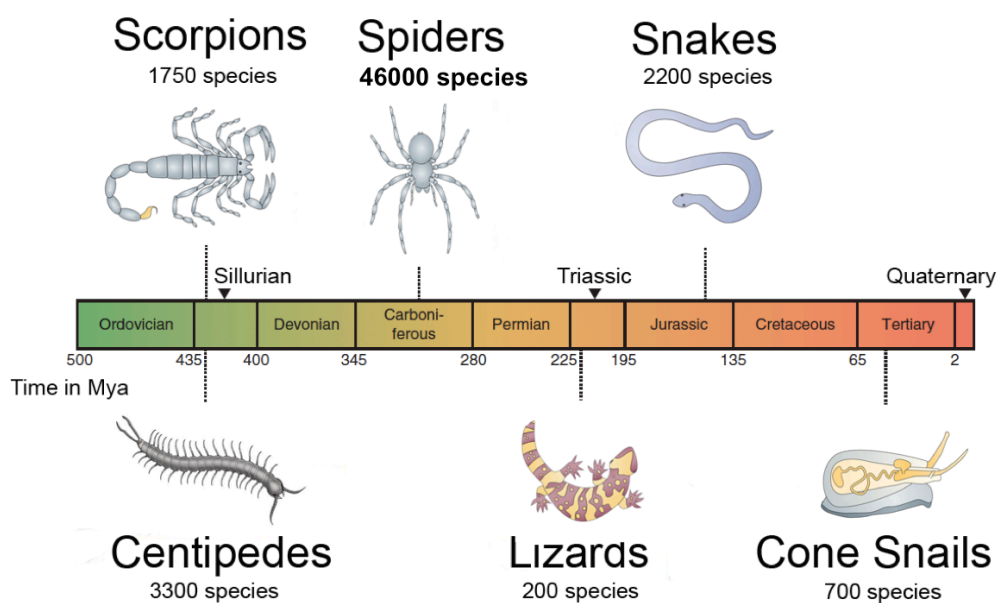


Figure 1.1: Evolutionary timeline of selected venomous animals (figure modified from Ref. ⁷).

1.4 The need for new insecticides

Food security is a major global issue as the world's population is projected to reach nine billion by 2050¹⁴. With rapid urbanisation and diminishing availability of arable land, it is important to increase crop yields to support the growing population¹⁴. Unfortunately, the effects of global warming have an immense negative influence on crop yields¹⁵, causing an increased occurrence of crop failures and global movement of insects from warm to what were previously cooler regions¹⁶⁻¹⁷. Although only a small minority of insects are

considered pests, it is estimated that herbivorous insects destroy one-fifth of the world's total crop production annually¹⁸.

The expansion of insects to colder regions has also led to increased reliance on insecticides and the escalating emergence of insecticide-resistant strains^{16, 19-20}. Besides threatening our food security, insect pests also pose a significant risk to human health as they are highly mobile vectors of a variety of human and animal pathogens²¹⁻²². Mosquitoes cause more suffering than any other organisms as they transmit a variety of disease-causing parasites and viruses²³. A classic example is *Anopheles gambiae*, the major vector of the malarial parasite *Plasmodium falciparum*. According to a 2015 World Health Organisation (WHO) report, there were an estimated 214 million cases of malaria in 2015 leading to an estimated 438,000 deaths. The majority of the cases occurred in sub-Saharan Africa with children under the age of 5 being the most susceptible (see WHO report at www.who.int/malaria/media/world-malaria-report-2015/en/). Tropical fevers such as dengue fever, Chikungunya and Zika fever caused by flaviviruses are transmitted by *Aedes* sp. mosquitoes²³. The outbreak of Zika virus infection in Brazil was linked to a spike in cases of babies born with microcephaly and Guillain-Barre syndrome that affects the nervous system (see WHO report at www.who.int/emergencies/zika-virus/articles/mosquito-control/en/). In the absence of effective antiviral therapies, vector control using chemical insecticides remains the most effective way to decrease disease transmission. Unfortunately, insecticide-resistant strains of mosquito have been identified in multiple countries, increasing the difficulty of pest control²⁴⁻²⁵.

1.5 Problems with current insecticides

Despite the increasing use of transgenic crops and other biological measures, chemical insecticides remain the primary method of insect pest control²⁶. Prolonged and widespread use of insecticides has promoted the evolution of insecticide resistance, with more than 600 arthropod species now resistant to one or more chemical insecticides^{10, 27} (**Fig. 1.2**). With selection pressure, it was shown that insecticide resistance could be acquired in as little as 22 generations with relatively few mutations in the gene to maintain the overall function and survivability²⁸⁻²⁹. Superficially, there appear to be a vast array of chemical insecticides but there are actually only five major insecticide targets: glutamate- and γ -aminobutyric acid (GABA)-gated chloride channels, insect voltage-gated sodium (Na_V) channels, nicotinic acetylcholine receptors (nAChRs), and acetylcholinesterase^{24, 30}.

Insensitivity to pyrethroid or dichlorodiphenyltrichloroethane (DDT) is acquired by a single point mutation of leucine to phenylalanine (L1014F) in housefly (*Musca domestica*) Na_v channels, resulting in 10–20-fold decrease in sensitivity. Resistance is further enhanced (> 500-fold) by a methionine (Met) to threonine substitution (M918T) in insect Na_v channels³¹. Similarly, an alanine to serine substitution (A302S) in the GABA receptor of the fruit fly *Drosophila melanogaster* confers resistance to cyclodienes³², while there are four point mutations in acetylcholinesterase (G265A, F330Y, G368A, and I1161V) associated with insensitivity to acetylcholinesterase inhibitors. These latter mutations individually or in combination conferred varying degrees of resistance in fruit fly³³.

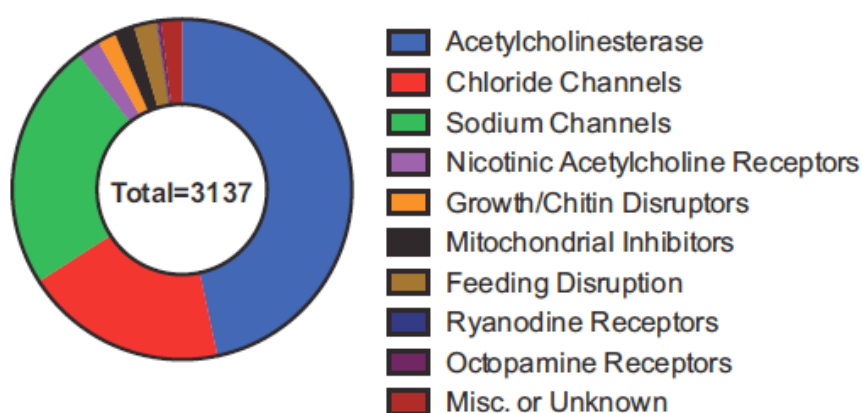


Figure 1.2: Total number of insecticide resistance cases grouped according to molecular target. The four main targets of insecticides are acetylcholinesterase (blue), GABA/glutamate-gated chloride channels (red), Na_v channels (green), and nAChRs (purple) (figure from Ref.³⁴).

In addition to issues related to the development of insecticide resistance, there are safety and environmental concerns regarding the use of certain chemical insecticides. Acetylcholinesterase inhibitors such as organophosphates pose ecological and health risks due to high toxicity and poor species selectivity. Exposure to organophosphates has been shown to have adverse effects on reproduction, development and cancer onset³⁵⁻³⁷. Some insecticides such as organochlorines are persistent organic pollutants that resist degradation leading to detrimental environment effects and bioaccumulation³⁸⁻³⁹. Due to health, safety and environmental concerns, the USA Environmental Protection Agency (EPA) deregistered 169 chemical insecticides between the years 2006 to 2009, while only nine new insecticides were approved during this period¹⁰.

1.6 Natural products as bioinsecticides

Due to the problems of chemical insecticides mentioned above, there is an urgent need to develop new, eco-friendly insecticides. In recent years, there has been a paradigm shift towards natural product-derived bioinsecticides as opposed to synthetic chemical insecticides. Pyrethrins, from which the synthetic pyrethroid insecticides are derived, are found in the seeds of *Chrysanthemum cinerariaefolium*; they are effective against many insects and have low toxicity in mammals⁴⁰. Azadirachtin, a Neem-seed extract, can be used as an insect repellent, anti-feedant and growth regulator with low non-target effects⁴¹. Bacterial products such as spinosad and avermectin which target the insect nervous system are also commonly employed to control insect pest populations⁴²⁻⁴³. However, a major downside with some natural insecticides is their relatively low efficiency, often requiring several days and repeated applications. An alternative approach is the use of potent insecticidal proteins or peptides that can be produced recombinantly or engineered into plants or entomopathogens. The best-known example of this approach is the use of pore-forming toxins secreted by the gram-positive soil bacterium, *Bacillus thuringiensis* (Bt)⁴⁴. When ingested, the alkaline and proteolytic environment of an insect gut liberates the virulent factor from Bt toxins enabling it to bind to the gut epithelium. The binding causes pore formation leading to the eventual death of the insect from starvation and septicemia⁴⁵. However, increasing resistance towards Bt transgenic crops had been reported in 5 of 14 major pest species⁴⁶. Moreover, Bt crops are resistant to a limited range of pests (primarily lepidopterans) as Bt is ineffective against sap-sucking pests such as aphids, which are a major agricultural pest⁴⁷. Thus alternative sources of bioinsecticides are constantly being assessed, of which arthropod venoms show great promise.

1.7 Venom peptides as bioinsecticides

Arthropods such as spiders, scorpions and centipedes are master insect predators. Based on a conservative estimate from ArachnoServer (www.arachnoserver.org) approximately 70% of SVPs are predicted to have insecticidal activity⁴⁸. These peptides typically target the nervous system causing rapid incapacitation or paralysis, and they can be highly insect selective. Some peptides isolated from Australian funnel-web spiders are lethal to multiple insect genera (Coleoptera, Orthoptera, Lepidoptera and Diptera) but harmless when injected into mice⁴⁹⁻⁵¹. Recently, a SVP was approved by the EPA for sale as a bioinsecticide in the United States (see www.vestaron.com/epa-approval/). Although

venoms are typically injected and not thought to be orally active, several SVPs isolated from an Australian tarantula were found to be insecticidal when fed to termites (*Coptotermes acinaciformis*), mealworm beetle (*Tenebrio molitor*) larvae and ticks (*Amblyomma americanu*), further highlighting the potential of SVPs as bioinsecticides⁵²⁻⁵³.

1.8 Venom peptides as therapeutic leads

Venomous animals have unintentionally become medicinal chemists. Their venoms contain numerous highly specific and potent peptides, many of which target vertebrate ion channels. The use of animal venoms as therapeutics is clearly evident in multiple traditional medicines across varied cultures. Many oriental medicines featured the use of animal venoms or poisonous secretions from bees or toads (*Venenum Bufonis*) for their touted pain relieving and anti-inflammatory properties⁵⁴⁻⁵⁵. Ayurveda (traditional Indian medicine) uses snake venoms to prolong life and treat arthritis and gastrointestinal problems⁷. The use of venoms in traditional medicines has been based on folklore and empirical observations rather than an understanding of the pharmacological basis of their effects. Recent advances in the molecular identification and functional understanding of ion channels and their roles in various diseases (channelopathies) has ignited interest in the discovery of ion channel modulators as research tools and potential therapeutic leads. This trend is exemplified by the increasing number of venom-derived drugs approved by the Food Drug Authority (FDA) and the many venom peptides currently in preclinical development and clinical trials (**Table 1.1**).

The current suite of drugs on the market can be broadly grouped into two main categories—traditional “small molecule” drugs (< 500 Da) that are generally administered orally and “biologics” (> 5 kDa), which are typically injected⁵⁶. Due to their small size, small molecule drugs have favourable pharmacokinetic properties, but often have poor target selectivity leading to undesirable side-effect profiles. In contrast, biologics are more selective but have low bioavailability, poor membrane permeability, and are metabolically unstable⁵⁶. A third and growing class of drugs, peptides (5–50 amino acid residues), may address some of the shortcomings from both drug categories⁵⁷. Peptide drugs can provide the selectivity and potency of biologics but with better bioavailability, lower immunogenicity and lower cost of production⁵⁸. They can also be made to be more stable and orally available using specific chemical modifications⁵⁸. Peptides have traditionally been

considered poor drug candidates due to their poor oral bioavailability. However, with recent advances in drug delivery, oral efficacy is often not a limiting factor for drug development and design⁵⁹ and has led to a revival of interest in peptidic drugs in recent years. There are now more than 34 peptide-based drugs available and 24 in various phases of clinical trial⁶⁰. In 2014 alone, 41 new molecular entities were approved by the FDA, of which one-tenth were peptide-based⁶¹.

Table 1.1: Venom-derived compounds in clinical trials or approved by the FDA^{7, 62-64}.

Compound	Status	Source	Molecular Target	Indication
Captopril	Approved	Arrowhead viper	angiotensin-converting enzyme (ACE) inhibitor	Hypertension
Tirofban	Approved	Saw-scaled viper	glycoprotein lib/IIIa inhibitor	Acute coronary syndrome
Eptifibatide	Approved	Pygmy rattlesnake	glycoprotein lib/IIIa inhibitor	Acute coronary syndrome
Bivalirudin	Approved	Leech	thrombin inhibitor	Anticoagulant
Ziconotide	Approved	Cone snail	inhibitor of voltage-gated calcium channel Ca _v 2.2	Chronic pain
Exenatide	Approved	Gila monster	glucagon-like peptide-1 agonist	Type 2 diabetes
Batroxobin	Approved	Lancehead snake	Fibrinogen protease	Haemostatic agent
Dalazatide	Phase IIa	Sea anemone	Inhibitor of voltage-gated potassium channel K _v 1.3	Autoimmune diseases
Cenderitide	Phase II	Green mamba	natriuretic peptide receptor	Chronic heart failure
Tumour Paint (BLZ-100)	Phase I	Death stalker scorpion	Chloride channels, matrix metalloprotease 2, annexin A2	Tumour imaging

1.9 Acid-Sensing Ion Channels (ASICs)

Acid-sensing ion channels are the primary acid sensors in mammals⁶⁵. As acidosis is a key feature of many pathological conditions, ASICs are promising molecular targets for the treatment of various pathological conditions such as trauma, ischemia, tumours, pain and inflammation⁶⁶. ASICs are proton-gated, cation-permeable (mainly Na⁺) ion channels that belong to the degenerin/epithelial sodium channel (DEG/EnaC) superfamily⁶⁷. Six ASIC subtypes (ASIC1a/b, ASIC2a/b, ASIC3 and ASIC4) assemble as homotrimeric (ASIC1a/b, ASIC2a and ASIC3 only) or heterotrimeric channels that are widely distributed in both the central and peripheral nervous system⁶⁸⁻⁷⁰ (**Table 1.2**). The combination of various subunits in a trimeric channel affords different channel characteristics such as cation permeability, proton sensitivity, and activation/inactivation kinetics⁷¹⁻⁷⁶. The first ASIC (ASIC2a) was cloned from human brain and named Brain Sodium (Na⁺) channel (BnaC1) as it was found to conduct Na⁺ ions⁷⁷. It was also cloned separately by another group and named mammalian degenerin 1 (MDEG1) based on sequence similarity with the

C. elegans degenerin channel⁷⁸. It was later found that these channels are proton-gated after the cloning of a homologous channel, ASIC1a (previously known as ASIC), with 67% similarity to ASIC2a⁷⁹. Subsequently, several homologous, proton-gated, Na⁺-permeable channels and splice variants were cloned from brain and dorsal root ganglia of human, rodents and other high-order vertebrates. The group of channels were collectively renamed as acid-sensing ion channels (ASICs) (**Table 1.2**). ASIC1a is the most abundant ASIC subunit in the central nervous system of rodents and humans. Unlike other ASICs, ASIC1a is also slightly permeable to calcium (Ca²⁺) and protons (H⁺)^{74, 80}. ASIC1a has been implicated in a variety of pathophysiological conditions such as inflammatory and neuropathic pain, psychiatric illness, multiple sclerosis, epileptic seizures, and ischemic stroke, and hence it is considered a promising therapeutic target^{66, 81}.

Table 1.2: Summary of ASIC subtypes^{71, 77-79, 82-87}.

Subtype	Alias	Gene	pH range	Distribution
ASIC 1a	ASIC- α / BnaC2	ACCN2	5.8–6.8	CNS, PNS ¹
ASIC 1b	ASIC- β	ACCN2	6.1–6.2	PNS
ASIC 2a	BnaC1/ MDEG1	ACCN1	4.5–4.9	CNS, PNS
ASIC 2b	MDEG2	ACCN1	NA	CNS, PNS
ASIC 3	DRASIC	ACCN3	6.4–6.6	PNS, Brain
ASIC 4	SPASIC	ACCN4	NA	CNS, PNS

¹CNS = central nervous system. PNS = peripheral nervous system.

1.10 Overall electrophysiological properties and structure of ASICs

As their name suggests, ASICs are highly sensitive to acidic environments (i.e. acidosis) and are activated upon rapid protonation. Combinations of various ASIC subunits exhibit characteristic electrophysiological profiles and sensitivities to protons, allowing a wide dynamic range for sensing perturbations to pH (**Fig. 1.3A**). As proposed by Gründer and Pusch (2015), ASICs exist as three distinct conformational states. At physiological proton concentrations (~pH 7.4), they exist in the resting state, in which they do not conduct ions. The channels are activated upon protonation of the channel (pH₅₀ for activation of ASIC1a is ~6.5), resulting in a conformational change from the resting state to an “open” state, allowing an influx of ions (mainly Na⁺) in the cell. Following activation (within 6–13 ms), the channels then promptly enter a desensitised state in which there is no further influx of ions despite the continuous presence of protons. ASICs can also become desensitised (a process known as steady-state desensitisation, SSD) without an apparent initial activation (pH₅₀ for SSD of ASIC1a is ~7.2). During SSD, the probability of proton binding is low and

thus channel activation is disorganised (hence accounting for the lack of apparent channel activation in electrophysiology experiment). The slow recovery time for SSD (~70 s) means that most channels exist in the desensitised conformation (*i.e.* they do not conduct ions). Some ASICs modulators, such as the spider toxin PcTx1, binds preferentially to the desensitised state of ASIC1a, induces SSD at physiological pH (**Fig. 1.3B**)⁶⁵.

The structure of ASIC1 was first solved using a non-functional, truncated version of the chicken ASIC1 (cASIC1) channel⁶⁹. A short time later, the structure of a functional, less truncated cASIC1 was obtained⁸⁸. As both structures were obtained at low pH, it is presumed that these crystal structures represent the desensitised state of the channel^{69, 88}. Overall, the two structures are highly similar and thus provide a definitive overview of ASIC structure. Three ASIC subunits combine to form a trimer with threefold symmetry; the channel has a large extracellular domain and a smaller transmembrane I domain comprised of two TM helices from each subunit^{69, 88}. A dominant feature of the surface of the extracellular domain is an acidic pocket, defined by the high density and close proximity of acidic residues Arg191, Glu220, Asp238, Glu239, Glu243, Gln271, Asp346, Asp350 and Asp408. The acidic pocket is important for proton sensing and thereby gating of the channel (**Fig. 1.3B**). Specifically, the acidic pocket contains three pairs of negatively charged residues (Asp238–Asp350, Glu239–Asp346 and Glu220–Asp408) that form carboxyl-carboxylate interactions^{69, 88}. The short distance between carboxyl-carboxylate pair suggested binding of protons at these sites⁶⁹. This was verified using mutagenesis of residues at the proposed protonation sites (Asp238Ala and Glu239Ala), which resulted in a significant shift in the pH-dependence of activation of ASIC1a to higher proton concentrations (EC_{50} 6.42 for wild-type compared to EC_{50} 3.92 for the double mutant)⁸⁹. Thus, the acidic pocket plays a vital role in pH sensing and is responsible for inducing the conformational changes which lead to activation of the channel⁹⁰. Peptide modulators such as PcTx1 bind at the acidic pocket (**Fig. 1.3B**) of ASIC1a, thereby inducing SSD at physiological pH⁹¹⁻⁹². In contrast, some modulators such as MitTx preferentially bind to the open state, resulting in channel activation⁹³.

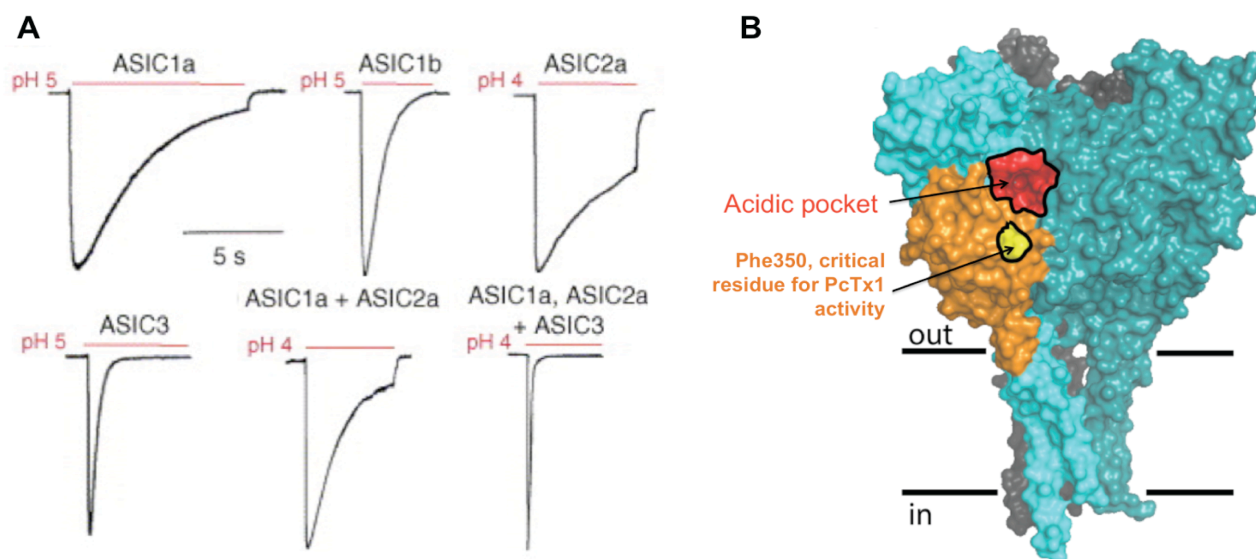


Figure 1.3. Properties of ASICs. (A) Electrophysiological profiles of ASICs: shown are sodium currents following a drop in pH to pH 5.0⁸¹. (B) Surface representation of cASIC1 channel. The acidic pocket is shown in red while one of the functionally critical residues for PcTx1 activity, Phe350, is highlighted in yellow.

1.11 Modulation of ASICs

The known modulators of ASICs can be broadly categorised as metal ions, small molecules, inflammatory mediators and venom peptides⁹⁴. Although there are several small-molecule modulators of ASICs, none of them has the high specificity and potency of ASIC modulators that have been isolated from animal venoms⁹⁴.

Divalent and trivalent ions (including but not limited to zinc, calcium and gadolinium) are able to modulate channel activity. Zinc inhibits homomeric ASIC1a and heteromeric ASIC1a/2a at nanomolar concentrations⁹⁵. However, at higher (micromolar) concentrations, it potentiates ASIC1a/2a currents⁹⁵. Calcium inhibits ASIC3 but has a dual effect on ASIC1a⁹⁶⁻⁹⁷, potentiating the channel at low concentration but inhibiting the channel at high concentration⁹⁶. Gadolinium inhibits homomeric ASIC2a with an IC_{50} of ~ 1 mM and heteromeric ASIC2a/3 with $IC_{50} \sim 40 \mu M$ ⁷⁶.

There are several small molecule drugs that inhibit ASICs. Amiloride, a commonly used diuretic drug, non-specifically inhibits all ASICs as well as members of the EnaC/DEG superfamily and Na^+/H^+ and Na^+/Ca^{2+} exchangers with an IC_{50} ranging from 10 to 50 μM ⁷⁹. Recent pilot studies revealed that treatment with amiloride reduced aura and headache symptoms in four of seven patients with otherwise intractable migraine⁹⁸. A-317567 is a novel small molecule that is more potent and selective for ASICs as compared to

amiloride⁹⁹. Animal studies indicated that A-317567 is useful for reducing post-operative and chronic inflammatory pain⁹⁹. Non-steroidal anti-inflammatory drugs (NSAIDs) such as ibuprofen, diclofenac, salicylic acid and aspirin are also non-selective inhibitors of ASIC1a and ASIC3 (IC₅₀ 90–250 μM)¹⁰⁰. An NSAID-derived small molecule, CHF5074 was shown to inhibit acid-evoked ASIC currents in hippocampal pyramidal neurons (IC₅₀ ~50 nM) and demonstrated neuroprotection against *in vitro* ischemia-induced cell death¹⁰¹. The small molecule 2-guanidine-4-methylquinazoline (GMQ) was found to induce sustained activation of ASIC3 (EC₅₀ ~ 0.06–3.34 mM) dependent on the dose as well as proton and Ca²⁺ concentrations¹⁰².

In addition, there are many endogenous modulators that are known to potentiate (increase or enhance current amplitude or duration) or increase pH sensitivity. These modulators include neuropeptides such as dynorphins and Phe-Met-Arg-Phe (FMRF) amide; polyamines such as spermine and agmatine; inflammatory mediators such as arachidonic acid (AA), lactate and nitric oxide (NO); neurotransmitters such as serotonin; and adenosine triphosphate⁶⁶.

To date, the most potent and selective ASIC modulators have been isolated from animal venoms (**Table 1.3**). Psalmotoxin 1 (PcTx1 or π-theraphotoxin-Pc1a) was the first described venom peptide modulator of ASICs. It was isolated from the venom of the South American tarantula *Psalmopoeus cambridgei*¹⁰³. PcTx1 consists of 40 amino acid residues with six cysteines, and it forms an ICK fold¹⁰⁴. It is the most potent and specific inhibitor of homomeric ASIC1a and heteromeric ASIC1a/2b (IC₅₀ of ~ 0.7 and 2.6 nM, respectively) and it has become an indispensable pharmacological tool for the study of ASIC1a function^{94, 103, 105}. PcTx1 increases the apparent affinity of ASIC1a to protons and stabilises ASIC1a in its desensitised state, preventing acid-induced currents at physiological pH¹⁰⁶⁻¹⁰⁷. Subsequently, it was found that PcTx1 also binds to ASIC1b, however, it appears to stabilise ASIC1b in its open state instead, thereby producing a potentiating or agonistic effect (albeit only at high concentrations) as opposed to its inhibitory effect on ASIC1a¹⁰⁷. Studies of the interaction of PcTx1 on chimeric channels indicated that PcTx1 binds to the thumb and palm domains of ASIC1a in the region of the acidic pocket¹⁰⁸; this suggestion was supported by several docking studies^{104, 109}) and finally confirmed upon co-crystallisation of truncated cASIC1 and PcTx1⁹¹⁻⁹². Molecular dynamics and mutagenesis studies based on the co-crystal structure further refined our knowledge on the interaction

of PcTx1 with ASIC1a by identifying all the peptide residues that are important for functional activity¹¹⁰.


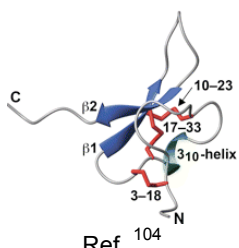

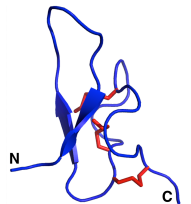

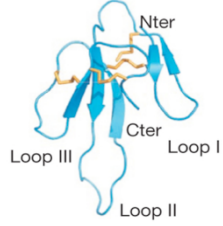

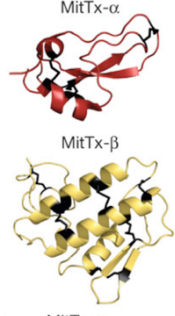

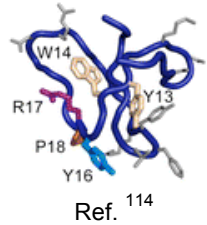

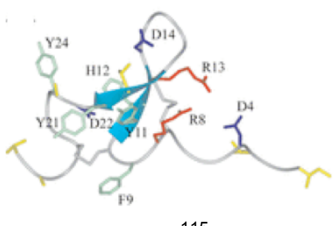
APETx2 is a 42-residue peptide isolated from the sea anemone *Anthopleura elegantissima* that inhibits homomeric ASIC3 with an IC₅₀ of 63 nM as well as the heteromeric ASIC3-containing channels ASIC2b/3, ASIC1b/3 and ASIC1a/3 with an IC₅₀ of 117 nM, 0.9 μM, 2 μM, respectively¹¹¹. At higher concentrations, APETx2 has also been shown to inhibit non-ASIC channels including Na_v channels and the voltage-gated potassium (K_v) channel K_v11.1 (also known as hERG)¹¹²⁻¹¹⁴.

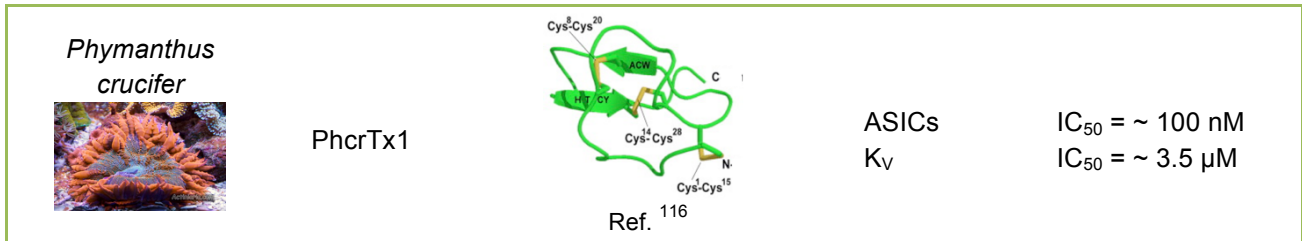
Several other sea anemone toxins have been reported to inhibit ASICs. These include Ugr-9-1 (π-AnmTxUgr 9a-1) from *Urticina grebelnyi*, which inhibits ASIC3 with an IC₅₀ of ~10 μM¹¹⁵, and PhcrTx1 from *Phymanthus crucifer* which partially inhibits native ASIC currents in sensory neurons (IC₅₀ ~100 nM). At micromolar concentrations, PhcrTx1 also inhibits K_v channels¹¹⁶.

Mambalgins are a family of homologous three-finger toxins (57-residue peptides) isolated from venom of black mamba (*Dendroaspis polylepis*) and green mamba (*Dendroaspis angusticeps*) snakes¹¹⁷⁻¹¹⁸. They have similar pharmacological profiles, inhibiting both ASIC1a and ASIC1b-containing channels with IC₅₀ values ranging from 11 to 252 nM¹¹⁷. As such, mambalgins inhibit a greater proportion of native ASIC currents (~60% inhibition) in rodent central neurons than PcTx1 (~40% inhibition)¹¹⁷. Mambalgins also appear to bind near the acidic pocket of ASIC1a¹¹⁹⁻¹²⁰; however, unlike PcTx1, they decrease the apparent affinity for protons, thereby inducing a shift in the pH-dependence activation of ASIC1a to lower pH, making the channel more resistant to acidosis¹¹⁷.

MitTx is a heterodimeric peptide complex isolated from the venom of the Texas coral snake (*Micrurus tener tener*)⁹³. It strongly activate ASICs, particularly ASIC1a, ASIC1b and ASIC3 with EC₅₀ values of ~9, 23 and 830 nM, respectively. Co-crystallisation of MitTx with cASIC1a revealed that it binds mostly to the thumb domain (overlapping with the PcTx1 binding site) and stabilises the channel in its open state¹²¹.

Table 1.3: Summary of ASIC modulators isolated from animal venoms¹²²

Species	Peptide	Structure	Targets	Activity
<i>Psalmopoeus cambridgei</i> 	PcTx1	 Ref. 104	ASIC1a ASIC1b ASIC1a/2b	IC ₅₀ = ~ 0.7 nM EC ₅₀ = ~ 101 nM IC ₅₀ = ~ 2.64 nM
<i>Heteroscodra maculata</i> 	Hm3a	 Homology model of Hm3a based on PcTx1 (see Chapter 3)	ASIC1a ASIC1b ASIC1a/1b	IC ₅₀ = ~ 1.3 nM EC ₅₀ = ~ 46.5 nM EC ₅₀ = ~ 17.4 nM
<i>Dendroaspis polylepis</i> 	Mambalgins	 Ref. 117	ASIC1a ASIC1b ASIC1a/2a ASIC1a/2b ASIC1a/1b DRG	IC ₅₀ = ~ 55 nM IC ₅₀ = ~ 192 nM IC ₅₀ = ~ 246 nM IC ₅₀ = ~ 61 nM IC ₅₀ = ~ 72 nM ~ 674 nM
<i>Micrurus tener tener</i> 	MitTx	 Ref. 93	ASIC1a ASIC1b ASIC3	EC ₅₀ = ~ 9 nM EC ₅₀ = ~ 23 nM EC ₅₀ = ~ 830 nM
<i>Anthopleura elegantissima</i> 	APETx2	 Ref. 114	ASIC3 ASIC3/2b ASIC3/1b ASIC3/1a hERG DRG Na _v 1.8	IC ₅₀ = ~ 63 nM IC ₅₀ = ~ 117 nM IC ₅₀ = ~ 0.9 μM IC ₅₀ = ~ 2 μM IC ₅₀ = ~ 1.21 μM IC ₅₀ = ~ 216 nM IC ₅₀ = ~ 2.6 μM
<i>Urticina grebelnyi</i> 	Urg9-1	 Ref. 115	ASIC3	IC ₅₀ = ~ 10 μM



1.12 ASICs as analgesic target

Pain, as defined by the International Association for the Study of Pain (IASP), is “an unpleasant sensory and emotional experience associated with actual or potential tissue damage, or described in terms of such damage”. Under normal conditions, pain acts as a warning signal for the bearer; however, its functionality is lost if it becomes a chronic occurrence (> 3 months) and it can be detrimental to one’s health both physically and psychologically. The IASP reported that one-fifth of the world’s population suffers from chronic pain. It was estimated that the total economic cost of chronic pain in the USA in 2008 was about USD \$600 billion, more than the combined economic cost of cancer, heart disease and diabetes¹²³. Pain-related disabilities remain a problem as current painkillers are often inadequate in providing sufficient pain relief and/or have undesirable dose-limiting side-effects that limit their usage¹²⁴.

Pain is initiated following a noxious stimulus at nociceptors located at the peripheral terminal of primary afferent sensory neurons¹²⁵. Ion channels and receptors located at the nerve terminal are temporarily activated, allowing an influx of ions into the cell which causes membrane depolarisation and generation of small receptor potentials¹²⁵. Amplification of these receptor potentials by downstream channels (e.g. by voltage-gated sodium (Na_v) channels) leads to action potentials that are transmitted along the afferent nerve fibres, via their cell bodies in the dorsal root ganglion (DRG), to the spinal cord where they synapse with ascending secondary sensory neurons that transmit the signal to the brain where it is perceived as pain¹²⁵. As depicted in **Fig. 1.4**, there are a variety of ion channels and receptors located at the peripheral terminal of nociceptors and along the nerve axon. They respond to different stimuli such as noxious temperature, mechanical trauma, changes in pH, and chemicals. ASICs are highly expressed along the nociceptive pathway (including the nociceptors, DRG, spinal cord neurons and many brain regions)

and are involved in nociception and pain processing (**Fig. 1.4**), responding specifically to acidosis and causing acidosis-related pain¹²⁶⁻¹²⁷.

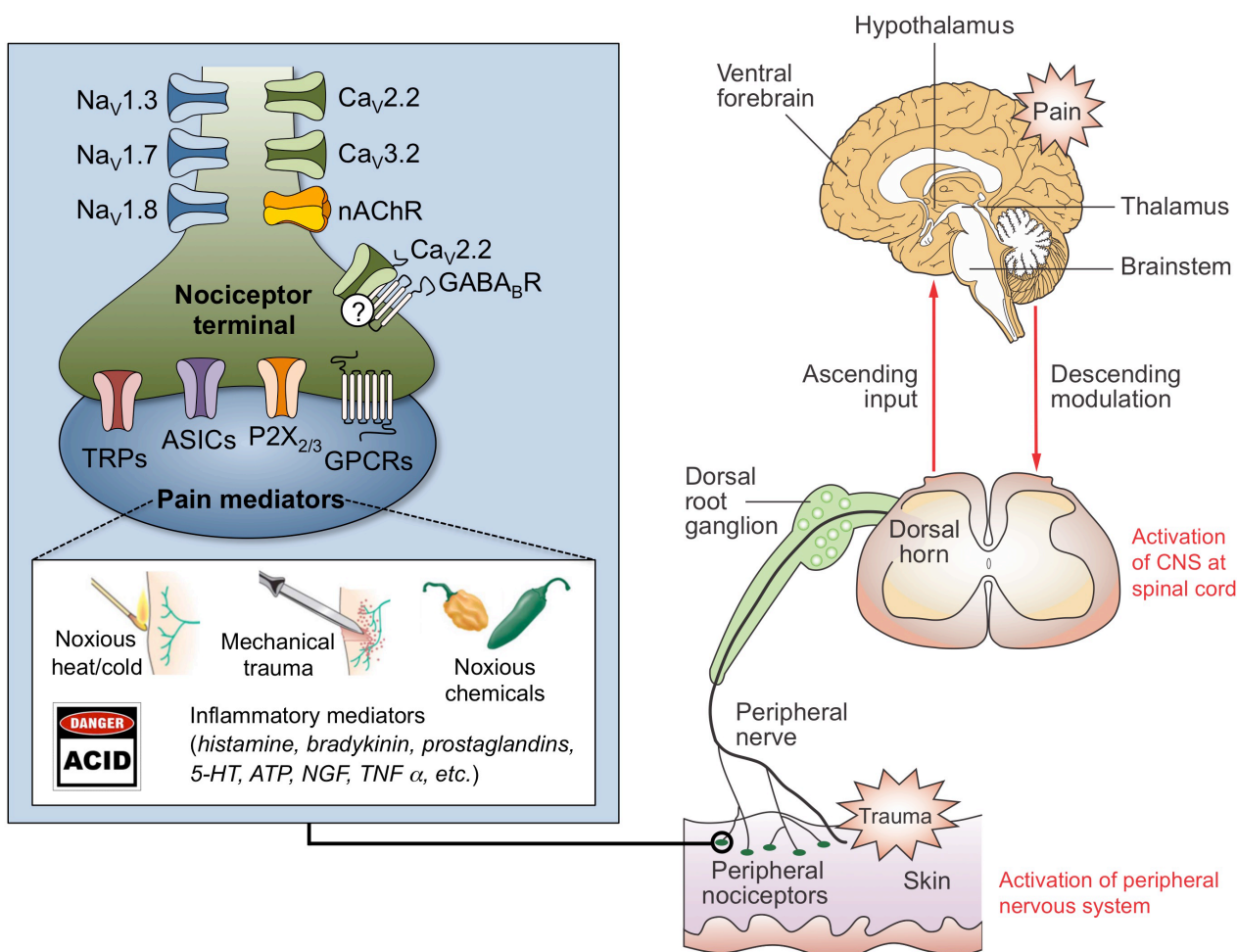


Figure 1.4. Schematic of the pain signalling pathway in humans. Noxious stimuli activate peripheral nociceptors, which leads to action potentials that are conveyed via the DRG to the spinal cord. These signals are then transmitted to the brain via ascending secondary sensory neurons. The intensity and duration of the nociceptive input can then be modulated by descending modulation from the brain. The peripheral terminals of nociceptors contain a variety of receptors and ion channels that respond to a wide range of noxious stimuli, as indicated in the inset at left.

Several early studies indicated that ASICs may be the major sensors of acid-induced pain in humans. Administration of non-selective ASIC inhibitors such as amiloride and NSAIDs (diclofenac and ibuprofen) attenuated pain induced by the application of acidic solutions in healthy human volunteers¹²⁸⁻¹²⁹. A more recent clinical study showed that the non-selective ASIC inhibitor amiloride was able to mitigate migraine pain in patients with an intractable form of the condition⁹⁸. The analgesic potential of ASIC inhibition has been better studied in animal models using more selective peptide modulators from animal

venoms. Analgesic effects were observed following introduction of PcTx1 into the CNS for both acute and neuropathic pain models as a result of ASIC1a inhibition and downstream effects mediated by the endogenous enkephalin pathway¹³⁰. It was shown that upregulation of ASIC1a in rat spinal dorsal horn neurons contributed to inflammatory pain hypersensitivity and spinal neuron sensitisation¹³¹. Thermal and mechanical pain sensitivity was attenuated with either intrathecal administration of PcTx1 or genetic suppression of ASIC1a in a rat FCA (Freud's complete adjuvant)-induced inflammatory pain model¹³¹. Mambalgin-1 produces antinociceptive effects when injected centrally (intrathecal) or peripherally (intraplantar) in mouse models of both thermal and inflammatory pain¹¹⁷. Inhibition of ASIC3 by *in vivo* knockdown using siRNA or APETx2 induces potent analgesic effects against acute inflammatory hyperalgesia¹³². ASIC3 is also the main sensor for cardiac pain. Cardiac afferents produce large acid-evoked currents in response to extracellular acidification (pH 7.1 to pH 6.7) that match those of ASIC3¹²⁷. Conversely, activation of ASIC1a, ASIC1b or ASIC3 via intraplantar injection of MitTx or GMQ elicited robust pain responses in mice^{93, 102}. The effects were significantly reduced by disruption of ASIC1a, ASIC1b or ASIC3^{93, 102}.

1.13 ASIC modulation for neuroprotection

ASICs play a significant role in the excitotoxicity of neuronal cells following ischemia. Reduction in blood supply causes localised hypoxia and the subsequent conversion from aerobic to anaerobic metabolism. This results in accumulation of hydrogen ions (H⁺) and other acidic metabolites (e.g. lactate) causing acidosis and subsequent activation and potentiation of ASICs. The consequent overexcitation of the cell (culminating in intracellular Ca²⁺ overload), initiates a cascade of downstream cytotoxic events and eventual cell death (*i.e.* excitotoxicity)¹³³⁻¹³⁴. Notably, inhibition of ASIC1a has been shown to afford neuroprotection in ischemic stroke, retinal ischemia, and traumatic spinal cord injury.

Stroke is the second leading cause of mortality worldwide, claiming more than 6.2 million lives annually. It is also the leading cause of permanent disability in many developed countries such as Australia and the USA¹³⁵⁻¹³⁶. In the USA, there are an estimated 700,000 cases of ischemic stroke each year, costing more than USD \$70 billion to society¹³⁷. Stroke is broadly categorised as ischemic or haemorrhagic¹³⁷. Ischemic stroke occurs following an occlusion of blood supply to the brain while hemorrhagic stroke is

characterised by intracranial bleeding (e.g. from ruptured blood vessels)¹³⁷. Ischemic stroke is by far the most prevalent type of stroke, accounting for ~87% of total stroke incidence in USA¹³⁸. It was estimated that ~2 million neurons are lost with every minute of artery occlusion during ischemic stroke, equivalent to the amount of neuronal loss over 26 years of normal ageing¹³⁷. The only approved treatment for ischemic stroke involves rapid reperfusion of the affected area through surgical procedures (e.g. thrombectomy) or enzymatic thrombolysis¹³⁷. Despite medical intervention for ischemic stroke, the mortality rate (~42%) and long-term disability remain high due to the narrow therapeutic window (3–4.5 hours depending on patient eligibility) and potentially adverse side-effects (e.g. intracranial haemorrhage) with the use of thrombolytic agents such as tissue plasminogen activator (tPA)¹³⁹⁻¹⁴⁰. The limitations of current treatments has sparked immense interest in the development of better stroke therapeutics.

Severe acidosis is observed following ischemic stroke with the pH in the ischemic core (brain tissue at the occlusion) and penumbral regions (brain tissues surrounding the occlusion) falling to as low as ~6, which is sufficient to robustly activate ASIC1a¹⁴¹. Multiple studies have shown that inhibition of ASIC1a through genetic knockout or acute pharmacological intervention (administration of “PcTx1 venom”, pure PcTx1 peptide or amiloride) after an occlusion of the cerebral artery (to simulate an ischemic stroke), reduced the infarct volume by ~60% in rodent models^{134, 141-142}. Moreover, neurological assessments indicated that the administration of PcTx1 after ischemic stroke significantly reduces motor deficits in rats, indicating preservation of neurons and functionality¹⁴².

Inhibition of ASIC1a results in a similar neuroprotective effect in retinal ganglion cells under ischemic stress. Retinal ischemia is a common cause of blindness arising from underlying retinal diseases such as glaucoma, diabetic retinopathy, and hypertensive vascular disease¹⁴³. It was shown that ASIC1a is expressed in retinal ganglion cells (RGCs) and is important for retinal activity¹⁴⁴. Retinal ganglion cells are highly sensitive to hypoxia; the loss of RGCs from hypoxic stress is the common etiology from these diseases leading to blindness^{143, 145}. Treatment with amiloride or PcTx1 after hypoxic stress increased the survival rates of cultured RGCs compared to non-treated RGCs¹⁴⁵.

In addition to deleterious effects of low pH during stroke and retinal ischemia, acidosis plays a significant role in the severity of secondary injury following a traumatic spinal cord

injury (SCI)¹⁴⁶. Multiple studies have suggested that the onset of secondary injury is mediated by events such as ischemia and inflammation after the initial trauma. This results in the production of inflammatory mediators (e.g. lactate and nitric oxide) which leads to the subsequent, enhanced activation of ASICs and cell death¹⁴¹. Elevated expression of ASIC1a, ASIC1a-mediated currents and Ca²⁺ influx in spinal neurons was observed in a rat model of thoracic spinal cord injury¹⁴⁶. Importantly, genetic ablation or pharmacological inhibition of ASIC1a in this model resulted in reduced tissue damage and also promoted the recovery of neurological function after a traumatic spinal cord injury¹⁴⁶. Thus, ASIC1a appears to be a promising target for neuroprotection of CNS and retinal neurons following ischemia.

1.14 Targeting ASICs for the treatment of neurological diseases

Currently, it is estimated that 48.4 million people worldwide are living with dementia, with an estimated economic burden of USD \$818 billion¹⁴⁷. The increasing life expectancy of the population is predicted to double this cost every 20 years, leading to an estimated cost of USD \$2 trillion in 2030¹⁴⁷. ASICs have been implicated in several neurological diseases such as Huntington's disease¹⁴⁸, Parkinson's disease¹⁴⁹, multiple sclerosis (MS)¹⁵⁰ and spinocerebellar ataxia 1¹⁵¹ which can lead to the onset of dementia. Besides tissue acidosis, these diseases cause the release of chemicals such as lactate and neurotransmitters that can lead to enhanced activation of ASICs¹⁴⁸. In many of these conditions, elevated expression of ASIC1a and acid-evoked currents are observed. MS is a chronic neuroinflammatory disease associated with axonal degradation and spinal cord acidosis¹⁵⁰. Increased expression of ASIC1a was observed in MS lesions and genetic ablation of ASIC1a or pharmacological blockade of ASIC1a with amiloride or PcTx1 attenuated axonal degradation, demyelination and reduced the clinical severity in mouse models of MS^{150, 152}. Huntington's disease and Parkinson's disease are neurodegenerative diseases that currently have no cure. Patients with Huntington's disease and Parkinson's disease displayed elevated levels of lactate in their brains indicating tissue acidosis¹⁵³. Parkinson's disease is characterised by motor impairment and a loss of dopaminergic neurons which have also been shown to express ASIC1a¹⁵⁴. The use of amiloride, benzamil and PcTx1 provided neuroprotection in mouse models of Huntington's and Parkinson's diseases¹⁴⁸⁻¹⁴⁹.

ASIC1a is highly expressed in the amygdala, a region of the brain important for emotional behaviour such as anxiety and fear¹⁵⁵. Characterisation of ASIC1a knockout mice revealed that expression of ASIC1a may be important for learning, synaptic plasticity and fear conditioning¹⁵⁵⁻¹⁵⁶. Overexpression of ASIC1a led to an increase in fear conditioning in animal studies¹⁵⁷. Conversely, in preclinical studies, genetic ablation or pharmacological inhibition of ASIC1a produced antidepressant-like and anxiolytic-like effects¹⁵⁸⁻¹⁵⁹. Finally, inhibition of ASIC1a with amiloride or PcTx1 was found to reduce seizures and neuronal injury in an *in vivo* model of epilepsy¹⁶⁰⁻¹⁶¹. Hence, ASICs may be novel molecular targets for antidepressants, antiepileptic drugs, and anxiolytics.

1.15 ASICs as molecular target for cancer therapeutics

Cancer is the leading cause of death worldwide with 8.2 million deaths and 14.1 million new cases identified in 2012 alone¹⁶². The microenvironment of solid tumours is often acidic as a result of poor vascularisation and high tumour cell metabolic rate, leading to hypoxia and lactate accumulation. This acidic environment has a strong influence on the progression, invasion, metastasis and responses of tumours to chemotherapy and radiation therapy¹⁶³. The expression and activation of ASIC1a has been associated with disease progression in several cancer types. Glioblastoma multiforme (i.e. glioblastoma or grade IV astrocytoma) is the most common and aggressive form of adult brain cancer for which there is currently no cure¹⁶⁴. Despite invasive treatment with resection surgery, radiotherapy and chemotherapy, the median prognosis for patient survival is 8.8–14.6 months¹⁶⁴. It was found that Glioblastoma multiforme display a constitutively active Na⁺ conductance due to a heteromeric ion channel consisting of ASIC1a, α ENaC and γ ENaC subunits¹⁶⁵⁻¹⁶⁶. This Na⁺ current is not observed in normal astrocytes or low-grade gliomas¹⁶⁵⁻¹⁶⁷. Inhibition of the current by amiloride or PcTx1 was found to regulate cell migration and cell cycle progression thus implicating the ASIC1a subunit in glioma pathogenesis¹⁶⁸⁻¹⁶⁹.

In addition to their involvement in cell migration and growth of gliomas, ASICs may also contribute to breast cancer tumorigenesis. Gupta and colleagues (2015) showed that several human breast cancer-derived cell lines had increased production of reactive oxygen species (ROS) when the cells were incubated at pH 6.5 as opposed to pH 7.4. This effect was significantly reduced in cells treated with amiloride or PcTx1 and in ASIC1a

knockdowns. Moreover, *in vivo* experiments in a mouse model of breast cancer revealed a reduction in acidosis-induced cell invasion, tumour growth and metastasis following ASIC1a inhibition¹⁷⁰. Breast cancer is the most commonly diagnosed cancer and it is the leading cause of cancer death among women, accounting for 25% and 15% of all cancer cases and deaths, respectively¹⁶². Hence, ASIC1a appears to be a novel therapeutic target to reduce breast cancer tumorigenesis.

1.16 Hurdle of CNS drug delivery — the blood-brain barrier

Multiple studies have highlighted ASICs as promising therapeutic targets, in particular the neuroprotective effects of ASIC1a antagonists observed in rodent models of CNS diseases such as ischemic stroke and multiple sclerosis. Given that venom peptides (e.g. PcTx1) are currently the most potent and selective ASIC modulators known, there is immense interest in these ASICs ligands for drug development. An important consideration for drug development is the method of delivery. Oral administration is the easiest and therefore the most common method for drug delivery. However, the relatively high molecular weight of peptides, their polar chemical characteristics, and pre-systemic enzymatic degradation severely limits their oral bioavailability¹⁷¹. Therefore, peptide/protein drugs (e.g. insulin) are typically administered via parenteral routes. Drug delivery via parenteral routes often involves injection (e.g. intravenous, intramuscular or subcutaneous) which is painful, difficult to administer, and carries a risk of infection and more severe side-effects¹⁷¹.

Additionally, the delivery of ASIC ligands to their intended site-of-action is a major hurdle for CNS diseases. Systemic delivery of therapeutics to the CNS is often challenging due to the blood–barrier barrier (BBB) which prevents the entry of >98% of small molecules and almost all large molecules¹⁷²⁻¹⁷³. Molecules that are small (< 600 Da), polar and lipophilic may be able to cross the BBB through passive transport (diffusion) across the tight junctions or endothelial cells. The movement of larger molecules are largely mediated through transport systems such as carrier-mediated transport, receptor-mediated transport or absorptive-mediated transport to cross the BBB (**Fig. 1.5**). However, in order to attain an effective drug concentration in the CNS, a substantially larger drug dose may be required, increasing the risk of systemic toxicity. Given the size and physicochemical properties of SVPs such as PcTx1, it is unlikely that such peptides would be able to cross the blood-brain barrier. Indeed, no brain uptake was observed following intravenous (IV)

administration of bovine serum albumin (66 kDa), demorphin (802 Da), chlorotoxin (4 kDa) or McoTI-II (3.3 kDa)¹⁷⁴. Hence, an efficient method of drug delivery to the CNS is required to access the required site-of-action.

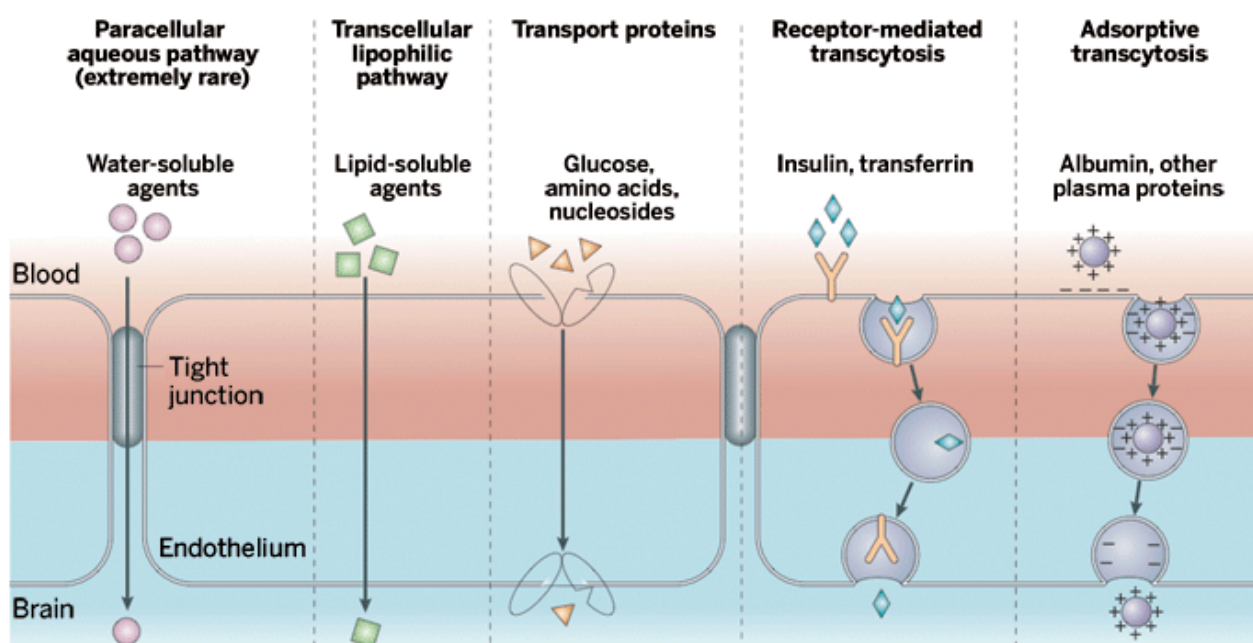


Figure 1.5. Schematic of the BBB endothelium which separates the brain from circulating blood. The BBB endothelial cells are joined by tight junctions which restricts the flow of most molecules into the brain. The main transport pathways are shown. A small amount of water-soluble agents may cross the tight junctions through the paracellular aqueous pathway. The lipid membrane surfaces may provide a transcellular lipophilic pathway for the transport of lipid-soluble molecules. Molecules such as glucose, amino acids and nucleosides are transported across the BBB via their associated transport proteins. Other molecules such as insulin and transferrin are transported via specific receptor-mediated transcytosis. Cationization of plasma proteins such as albumin may enhance brain uptake through adsorptive transcytosis. (Figure from Ref.¹⁷⁵).

The BBB is a unique microvasculature system which segregates the interstitial fluid in the CNS (brain and spinal cord) from the circulating blood¹⁷³. It consists of a single layer of endothelial cells sealed by intercellular tight junctions (TJs). BBB endothelial cells differ morphologically from their peripheral counterparts by a lack of fenestrations, and they have extremely low rates of transcytosis. Movement of molecules across the BBB is tightly regulated in order to maintain the homeostasis of the microenvironment and functioning of cells in the CNS¹⁷⁶. Compromised BBB integrity can result in increased BBB permeability, leading to increased extravasation of immune cells and unregulated influx/efflux of molecules across the BBB. Disruption of BBB integrity is a common phenomenon in many neurological diseases such as stroke, MS, Alzheimer's disease (AD), epilepsy, and

traumatic brain injuries, and this may therefore allow entry of therapeutics into the CNS. However, it remains uncertain if the disruption is a contributing causative effect or the resultant effect in some of these diseases¹⁷⁶⁻¹⁷⁷. In the case of ischemic stroke, BBB disruption occurs in a biphasic manner. The generation of excessive reactive oxygen species due to oxidative stress from ischemia and reperfusion leads to the first phase of BBB disruption. Subsequently, the compromised BBB allows infiltration of immune cells (e.g. neutrophils) which leads to the second phase of BBB disruption¹⁷⁶. Despite observations of BBB disruption in many neurological diseases, delivery to the CNS remains a bottleneck for the development of CNS-targeted therapeutics. For example, in the case of ischemic stroke, opening of the BBB does not occur until around 10–12 h post stroke, and it would seem highly beneficial to be able to deliver a neuroprotective therapeutic to the CNS as early as possible. Thus, alternative routes for CNS drug delivery are needed.

1.17 Methods to overcome the blood brain barrier

Current methods of delivering drugs to the brain include invasive methods such as intracerebroventricular (ICV), intraparenchymal, intracerebral and intrathecal injections¹⁷⁸. However, these delivery methods require high levels of technical expertise and carry the risk of infections and further tissue trauma and hence they are not practical for repeated dosing¹⁷². Moreover, the effectiveness of both routes is limited by the penetration and diffusion properties of the drug away from the injection site¹⁷². The use of convection enhanced diffusion (CED) may increase the diffusion zone by maintaining a pressure gradient during interstitial infusion of the drug, thereby generating flow through the brain¹⁷⁹.

Other methods of CNS drug delivery through the BBB are currently being investigated. BBB disruption methods (**Table 1.4**) are associated with side-effects such as severe vasculopathy, chronic neuropathologic changes, seizures and leakage of plasma proteins (e.g. albumin)¹⁷⁷. Translocation of pharmaceuticals through the BBB may also be achieved through receptor-mediated or absorptive-mediated transcytosis (**Fig. 1.5**) by coupling drugs with molecular ligands that act as a Trojan horse¹⁸⁰.

Table 1.4. Summary of blood-brain barrier disruption strategies.

BBB Disruption strategy	Methodology
Osmotic	Use of hyperosmotic solution (e.g. mannitol) to induce shrinkage of cerebrovascular endothelial cells, disrupting the tight junctions.
Biochemical	Use of vasoactive compounds (e.g. bradykinin) to selectively increase permeability in brain capillaries in diseased tissue to enhance uptake.
Ultrasound-mediated	Use of ultrasonic waves for site-focused BBB disruption.

1.18 Intranasal administration as alternative for CNS drug delivery

Intranasal (IN) administration may provide a non-invasive route for CNS drug delivery that effectively bypasses the BBB. The feasibility of IN administration of peptides and proteins for CNS delivery has been assessed in multiple preclinical and clinical studies with promising results¹⁸¹. The pioneering study by Born and colleagues showed that IN administration of melanocortin (980 Da), arginine-vasopressin (1.1 kDa) and insulin (5.8 kDa) led to their detection in cerebrospinal fluid (CSF), but not blood plasma, 30 min after administration¹⁸². IN administration of iodine-125 radiolabeled insulin (¹²⁵I-insulin) and insulin-like growth factor 1 (¹²⁵I-IGF-I) (7.65 kDa) yielded high levels of radioactivity in the trigeminal nerve branches, trigeminal ganglion, pons, and olfactory bulbs in rodents¹⁸³⁻¹⁸⁴. Even larger proteins have been successfully delivered to the CNS via the IN route. Interferon- β 1B (18.5 kDa), assessed as a treatment for MS in rodent and primate models, exhibited CNS uptake following IN administration as tracked via ¹²⁵I-labelling¹⁸⁵⁻¹⁸⁶. Furthermore, IN administration of erythropoietin (34 kDa) was shown to protect the brain against stroke in animal models¹⁸⁷⁻¹⁸⁹. Notably, ICV and IN (but not intravenous) administration of *P. cambridgei* venom (from which PcTx1 was isolated) provided neuroprotection in rodent stroke models¹⁴¹.

A search of active and completed clinical trials involving IN administration of drugs identified 751 studies of which 108 have been concluded with results (see <https://clinicaltrials.gov>). Some of these trials involve the study of the central effects of peptides such as insulin and oxytocin. Insulin acts as a neuromodulator important for cortical activity. Thus, IN administration was explored for direct CNS administration to minimise systemic exposure¹⁹⁰. IN administration of insulin elicited beneficial central effects in patients with Alzheimer's and Type 2 diabetes with minimal systemic side

effects^{191,190}. Similarly, IN administration of the neuropeptide oxytocin (1 kDa) resulted in enhanced multiple positive “pro-social” behaviours^{192, 193}: McRae-Clark, 2013 #265.

1.19 Mechanisms of CNS delivery via IN administration

Numerous studies on animals and humans have shown that IN administration provides a non-invasive method of bypassing the BBB to deliver peptide-based therapeutics to the CNS¹⁹⁴. The nasal cavity extends from the nostrils to the nasopharynx, and can be broadly divided into the vestibule, respiratory and olfactory epithelium (**Fig. 1.6A**). The regular turnover of cells may facilitate the uptake of IN-administered molecules across the nasal epithelium, enabling access to the neuronal pathways located at the respiratory or olfactory epithelium (**Fig. 1.6B**) for transport to the CNS¹⁷⁸.

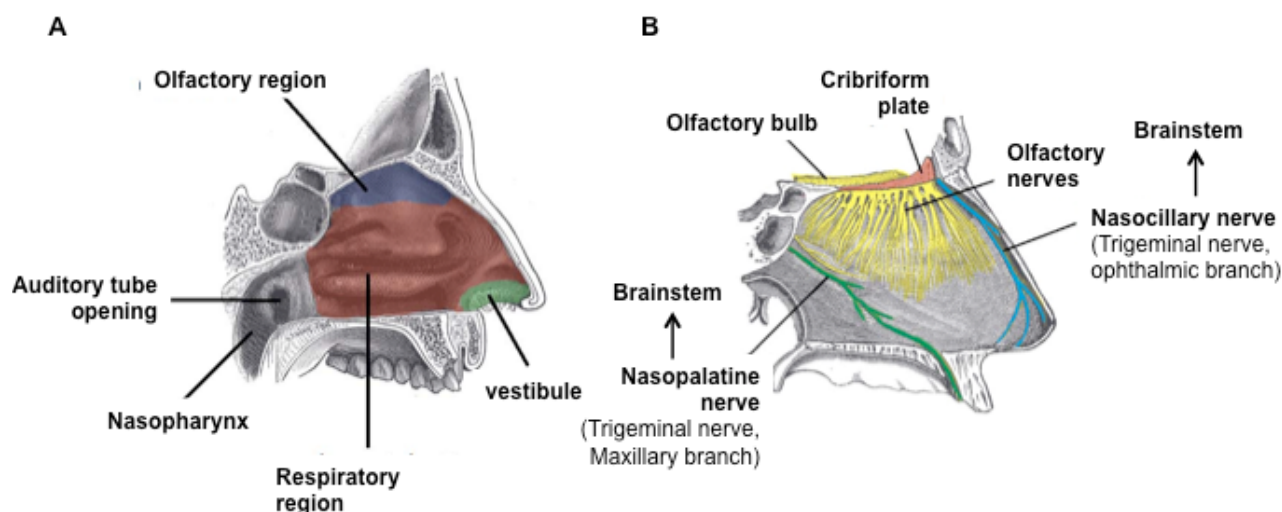


Figure 1.6. Anatomy of the human nasal cavity. (A) Sagittal section of the nasal cavity highlighting the vestibular (green), respiratory (red) and olfactory (blue) epithelial regions. (B) Lateral view showing innervations of the olfactory bulb (yellow) and trigeminal nerves (blue and green) in the nasal cavity. Figures adapted from <http://teachmeanatomy.info/head/organs/the-nose/nasal-cavity/>.

There are several possible pathways for drug delivery to the CNS following IN administration as shown in **Fig. 1.7**. Following deposition in the nasal cavity, the drugs first cross the nasal epithelium to access the olfactory and trigeminal nerve pathways which extends to the olfactory bulb or brainstem. Transport of the drug along these nerve pathways to the brain may be achieved through intracellular transport mechanisms such as endocytosis or axonal transport. However, given that the vast majority of studies reported rapid delivery (within minutes to hour) of molecules in the brain, intracellular transport is unlikely to be the main mode of transport. Instead, the extracellular channels

such as the lymphatic, perivascular or perineural spaces associated with the nerve pathways is more likely to be the predominant mode of transport for molecules to the brain, following intranasal administration^{180, 194}.

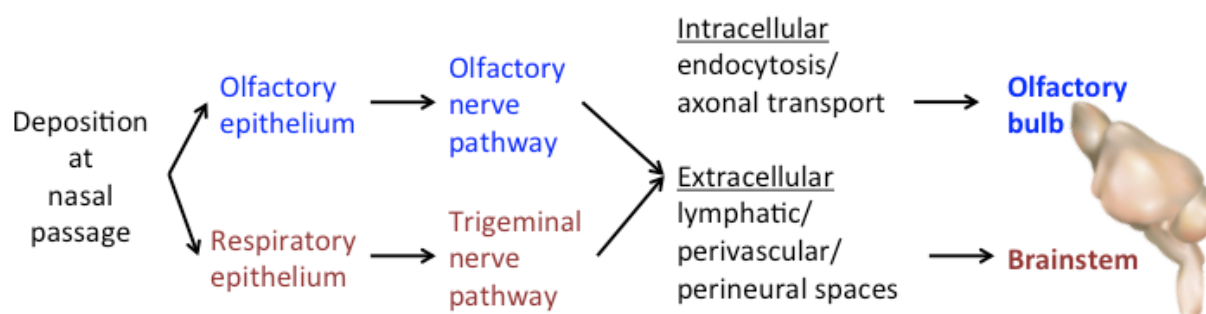


Figure 1.7. A schematic of the pathways to CNS following intranasal administration. Figure of mouse brain obtained from <http://www.clker.com/clipart-354921.html>.

The olfactory neuronal pathway is thought to be the major route involved in IN delivery to the CNS¹⁹⁵. The olfactory epithelium is interspersed with olfactory sensory neurons (OSNs) with dendrites exposed at the mucosal surface extending through the cribriform plate and terminating at the olfactory bulb. The OSNs are enveloped by olfactory ensheathing cells (OECs) that creates fluid-filled, perineural channels along the olfactory nerve pathway. Molecules can travel along these channels via extracellular bulk flow mechanisms to reach the CNS rapidly¹⁸¹. As the OSNs are first-order neurons (*i.e.* no synapses), intracellular transport of molecules may also occur following endocytosis of the administered molecule¹⁸¹.

The trigeminal pathway is another potential route to the CNS following IN delivery^{183, 185}. Both the respiratory and olfactory epithelium are innervated with fibres from trigeminal nerves (mandibular and ophthalmic), with free nerve endings located near the surface. The trigeminal nerves run along the caudal and rostral regions of the brain, terminating in the brainstem. Biodistribution studies of IN administered radiolabelled proteins recorded radioactivity along the trigeminal nerves, trigeminal ganglion, medulla pons (part of the brainstem) and cerebellum, thereby indicating the plausibility of the trigeminal nerve delivery pathway^{183, 185}.

In summary, IN administration is a promising method for delivery of venom peptides, which are typically 3–5 kDa in size. Given the therapeutic potential of spider venom peptides,

exploration of different administrations routes for their administration and understanding of their *in vivo* pharmacokinetics and biodistribution will aid in the future development of venom-peptide based therapeutics.

Aims of PHD project

Overall aim

Spider venom peptides have immense biotechnological potential in both the agrichemical and therapeutic fields. Thus, the overall aim of this project is to isolate, characterise and develop SVPs with potential for biotechnological applications in two key areas: (1) insect control using orally active insecticidal peptides; (2) improvement of human health using peptides that target acid-sensing ion channels as therapeutic leads.

Specific aims

1. Characterisation of an Orally Active Insecticidal Peptide (OAIP3) isolated from the Australian featherleg tarantula, *Selenotypus plumipes*
2. Isolation and pharmacological characterisation of a novel ASIC1a modulator from the venom of the tarantula *Heteroscodra maculata*
3. Elucidation of the biodistribution and pharmacokinetics of PcTx1 following different routes of administration (IV and IN) using positron emission tomography (PET) and computed tomography (CT).

Chapter Two

Functional and structural characterisation of an Orally Active Insecticidal Peptide 3 (OAIP3) isolated from the venom of the Australian featherleg tarantula, *Selenotypus plumipes*

2.1 Introduction

Insects are the largest and most widely distributed group of terrestrial animals. While only a small group of insects are considered pests, they are responsible for significant crop damage, economic losses, and human mortality¹⁰. Herbivorous insect pests reduce crop yields by 10–20% and damage ~20% of stored grains annually^{18, 196}. They are also vectors for a multitude of human and animal pathogens — mosquitoes alone causes more than one million deaths worldwide each year²³. Despite biological control measures such as the use of transgenic crops, chemical insecticides remained the dominant method for control of insect pests¹⁹⁷. Unfortunately, the available arsenal of chemical insecticides is rapidly diminishing due to the increasing number of resistant insect strains resulting from long-term use of chemical insecticides, as well deregistration of insecticides by regulatory authorities due to concerns about their detrimental effects on human health and the environment¹⁰. Together, these mounting problems have invigorated the search for novel and safer insecticidal compounds.

Natural products are an excellent source of insecticidal compounds¹⁹⁸. The success of transgenic crops expressing Bt toxins (orally active δ -endotoxins from *Bacillus thuringiensis*) for insect pest control⁴⁴ has fuelled interest in the discovery and development of insecticidal proteins (or peptides) as bioinsecticides. Spiders, being master insect predators, are an obvious starting point for such a search. Equipped with highly efficient venoms, they are able to achieve rapid incapacitation of prey through envenomation¹⁰. Spider venoms are a complex cocktail of small molecules, peptides and proteins. Spider-venom peptides are of particular interest as many are potently insecticidal and resilient to degradation^{51,12}. Based on a “phyletic specificity” search on ArachnoServer (www.arachnoserver.org)⁴⁸, more than 63% (234 of 368 identified toxins) are targeted towards insects. Interestingly, despite the lack of evolutionary drive (since venoms are typically injected), some spider venom peptides are also orally efficacious^{53, 199}.

A recently filed patent reported the discovery of several orally active insecticidal peptides (OAIPs 1-5) isolated from the venom of the Australian featherleg tarantula, *Selenotypus plumipes*²⁰⁰. The venom of *S. plumipes* was found to be potent on crickets (*Acheta domesticus*) and mealworms (larvae of *Tenebrio molitor*) with LD₅₀ values of ~69 and 2 µg/g respectively²⁰¹. The venom was fractionated using reversed-phase high-performance liquid chromatography (RP-HPLC) and individual fractions were fed to termites to identify insecticidal components that are orally active¹⁹⁹. This led to the isolation of five OAIPs. The potency, and more importantly, oral insecticidal activity in termites, has evoked strong commercial interest in these peptides as bioinsecticides.

OAIP1 is the most potent orally active insecticidal peptide described in the literature to date, with an LD₅₀ value of 104 pmol/g in the economically important cotton bollworm *Helicoverpa armigera*⁵². It was produced using solid-phase peptide synthesis (SPPS) as previous attempts at recombinant production were unsuccessful¹⁹⁹. However, large-scale production of peptides by SPPS for commercial use (e.g. field spraying) is impractical given the quantity needed.

OAIP3 was isolated from the same venom as OAIP1. It has a reported efficacy of 100% mortality in mealworms when injected at a dose of 3 nmol/g and ~50% mortality in termites when fed at 350 nmol/g¹⁹⁹. A recombinant expression strategy was chosen for production of OAIP3. As there is low sequence homology between OAIP1 and OAIP3 (implying there may be significant structural differences), we used multidimensional heteronuclear nuclear magnetic resonance (NMR) spectroscopy for structural determination. The recombinant peptide was also tested in mealworms for functional studies.

This chapter describes the recombinant production, insecticidal activity and solution structure of OAIP3. The functional and structural information obtained from this study may aid in the future development of peptide-based bioinsecticides as well as engineering of peptide drugs with oral efficacy and bioavailability.

2.2 Materials and Methods

2.2.1 Bacterial transformation, recombinant expression and purification of OAIP3

The gene sequence for OAIP3 was obtained by reverse translation of the peptide sequence, with optimisation of codons for *E. coli* expression. Gene construction and subcloning of the synthetic gene into the pLICC expression vector was performed by GENEART™ (ThermoFisher Scientific, USA). The plasmid was transformed into competent *E. coli* BL21 (λDE3) by heat shock at 42°C then plated onto lysogeny broth (LB) agar containing 100 µg/mL ampicillin (Astral Scientific, Australia) for positive selection. The transformed colonies were expanded in LB media containing 100 µg/mL ampicillin (unless otherwise stated, all LB media were supplemented with 100 µg/mL ampicillin) until the OD₆₀₀ reached ~2; the cell culture was then mixed 1:1 in 60% sterilised glycerol and stored at -80°C as glycerol stocks.

Production of recombinant OAIP3 was based on a published protocol for recombinant production of disulfide-rich peptides²⁰². Briefly, cultures were grown in LB media incubated at 37°C with constant agitation at 180 rpm until the OD₆₀₀ reached ~1. For production of isotopically ¹³C/¹⁵N-labeled OAIP3, the culture was first incubated in 2 L LB media until the OD₆₀₀ reached ~0.6, then cells were harvested by centrifugation at 3000 g for 15 min at 4°C. The cell pellet was gently resuspended in 500 mL of minimal medium (22 mM KH₂PO₄, 90 mM Na₂HPO₄, 17 mM NaCl, 1.6 mM MgSO₄, 80 nM CaCl₂) supplemented with ¹³C₆-D-glucose (22 mM) and ¹⁵NH₄Cl (18 mM) (as the sole carbon and nitrogen sources, respectively), 0.5 mg thiamine and 0.002% vitamins (1.1 mg biotin, 1.1 mg folic acid, 110 mg para-aminobenzoic acid, 110 mg riboflavin, 220 mg pantothenic acid, 220 mg pyridoxine HCl, 220 mg thiamine HCl, 220 mg niacinamide in 50% ethanol/water). The culture was further incubated for 2 h at 37°C. Protein expression was induced with 0.5 mM isopropyl-β-D-thiogalactopyranoside (IPTG) and the culture allowed to grow overnight at 20°C.

Cells were harvested the following day by centrifugation at 6000 g for 15 min at 4°C, then the cell pellet was resuspended in Equilibration Buffer (EB: 20 mM Tris, 200 mM NaCl, pH 8). The cells were then mechanically lysed using continuous flow cell disruption with a TS Series Constant Systems Cell Disruptor (Constant Systems Ltd, UK) at 28 kpsi. DNase (~1 µg/mL) was added to reduce the viscosity of the cell lysate. The soluble cell fraction

was then obtained by centrifuging the cell lysate at 16000 *g* for 20 min at 4°C. The His₆-containing fusion protein was captured on Ni-NTA Superflow resin (Qiagen, Germany) loaded into a gravitational flow column. Non-specifically bound components were removed with Wash Buffer (EB containing 10 mM imidazole) and then the fusion protein was eluted with Elution Buffer (EB containing 250 mM imidazole). The fusion protein was concentrated using a 30 kDa cut-off spin filter (Merck Millipore, USA), then diluted to 10 mL with EB containing 3 mM reduced glutathione (GSH) and 0.3 mM oxidised glutathione (GSSG). Approximately 200 µg of tobacco etch virus (TEV) protease was added for each litre of bacterial culture purified. The cleavage reaction was allowed to proceed overnight at room temperature with gentle rocking.

The cleavage mixture was acidified with 1% trifluoroacetic acid (TFA) then centrifuged at 16000 *g* for 20 min at 4°C and filtered through a 0.22 µm syringe-driven polyvinylidene fluoride (PVDF) membrane filter. The liberated recombinant peptide was purified using RP-HPLC on a Phenomenex C₄ column (250 mm x 4.6 mm x 10 µm, 300 Å) at a flow rate of 5 mL/min using a gradient of 15–45% Solvent B (0.043% TFA in 90% acetonitrile) in solvent A (0.05% TFA in water) over 30 min (gradient of 1% Solvent B/min). A secondary purification was performed using a XB-C18 column (Phenomenex Kinetex, 250 x 4.6 mm x 5 µm, 100 Å). The purity and mass of the final product was verified using analytical RP-HPLC and mass spectrometry.

2.2.2 Structure determination

Isotopically-labeled OAIP3 was reconstituted to a final concentration of 300 µM in 30 mM MES buffer, pH 6, constituted in 5% D₂O. The sample was filtered using a Costar® Spin-X® Centrifuge Tube Filters (0.22 µm pore size; Corning, USA), then 300 µL was added to a susceptibility-matched 5 mm outer diameter microtube (Shigemi Inc., PA, USA). NMR spectra were collected at 25°C on a 900 MHz NMR spectrometer (Bruker BioSpin, Germany) equipped with a cryogenically-cooled triple resonance probe. Spectra collection, editing and data processing were performed by Dr Mehdi Mobli (CAI, The University of Queensland).

3D and 4D spectra used for resonance assignments were acquired using non-uniform sampling. Sampling schedules that approximated the signal decay in each indirect

dimension were generated using sched3d²⁰³. Non-uniform sampling data were processed using the Rowland NMR toolkit (www.rowland.org/rnmrtk/toolkit.html) and maximum entropy parameters were automatically selected as previously described.¹³C- and ¹⁵N-edited HSQC-NOESY spectra (mixing time of 200 ms) were acquired using uniform sampling. Separate ¹³C-edited HSQC-NOESY spectra were acquired for the aliphatic and aromatic regions of the carbon spectrum.

Dihedral angles were derived from TALOS+ chemical shift analysis²⁰⁴ and the restraint range for structure calculations was set to twice the estimated standard deviation. NOESY spectra were manually peak picked and integrated, peak lists were then automatically assigned, distance restraints extracted, and an ensemble of structures calculated using the torsion angle dynamics package with CYANA 3.0²⁰⁵. The tolerances used for CYANA were 0.02 ppm in the direct ¹H dimension, 0.04 ppm in the indirect ¹H dimension, and 0.4 ppm for the heteronucleus (¹³C/¹⁵N). During the automated NOESY assignment/structure calculation process, CYANA assigned 92% of all NOESY peaks (1447 of 1566). The disulfide bonds were assigned on the basis of preliminary structure calculations; subsequent calculations included distance restraints for these disulfide bonds as described previously²⁰⁶.

2.2.3 Insecticidal assay

Mealworms were purchased from Pisces Enterprises (Kenmore, QLD, Australia). Insects between 3rd and 4th instar (mass 162–168 mg) were used. For each mealworm, 2.6 μ L of toxin diluted in ultrapure water was injected into the metathoracic pleurite. Injections were performed using a 29.5 gauge insulin syringe (B–D Ultra-Fine, Terumo Medical Corporation, Elkton, MD) needle fitted to an Arnold hand micro-applicator (Burkard Manufacturing Co. Ltd., England). Three replicates of five insects were used for each toxin concentration. After injection, the mealworms were housed in petri dishes and maintained with wet chicken feed. Effects were monitored over 48 h. Mealworms that did not respond to gentle provocation were considered moribund (dead or paralysed); this assay was performed by Dr Volker Herzig (IMB, The University of Queensland). Means and standard deviations were calculated using Graphpad Prism 6.0 (La Jolla, USA).

2.2.4 Mass spectrometry

Peptide masses were determined using matrix-assisted laser desorption/ionisation time-of-flight (MALDI-TOF) mass spectrometry (MS) on a 4700 Proteomics Bioanalyser (Applied Biosystems, Carlsbad, CA, USA). Fractions were spotted 1:1 (v/v) with α -cyano-4 hydroxycinnamic acid (CHCA) matrix (7 mg/mL in 50% acetonitrile/water, 0.1% formic acid). All masses reported are for monoisotopic $[M+H]^+$ ions, using positive reflector mode, or average mass using linear mode.

2.3 Results

2.3.1 Recombinant expression of OAIP3

Recombinant OAIP3 was produced using an *E. coli* periplasmic expression system optimised for production and purification of disulfide-rich venom peptides²⁰². The IPTG-inducible plasmid encodes a MalE signal sequence for translocation of the fusion protein from the cytoplasm to the periplasm, an N-terminal His₆ tag for purification using nickel affinity chromatography, followed by a maltose-binding protein (MBP) fusion tag to enhance solubility of the expressed protein, a TEV protease recognition site for liberation of fusion tags, and finally the OAIP3 peptide sequence (**Fig. 2.1A**). The recombinant OAIP3 sequence contains a non-native N-terminal glycine residue as the N-terminal residue of native OAIP3 is glutamic acid, a non-favoured residue for the P' position of the TEV protease recognition site²⁰⁷. The cystine pairings in OAIP3 determined using NMR (see below) matched the ICK framework commonly seen in SVPs (**Fig. 2.1B**).

The expression and purification of OAIP3 is illustrated in **Fig. 2.1C**; comparison of lanes 2 and 3 in **Fig. 2.1C** reveals overexpression of the His₆-MBP-OAIP3 fusion protein after IPTG induction. The fusion protein is highly soluble as most of the His₆-MBP-OAIP3 fusion protein was found in the soluble fraction following cell lysis (compare lanes 4 and 5 in **Fig. 2.1C**). None of the His₆-MBP-OAIP3 fusion was lost during application of the soluble cell fraction to a Ni-NTA column (**Fig. 2.1C**, lane 6) or during a subsequent wash step with 5 mM imidazole (**Fig. 2.1C**, lane 7). A large amount of His₆-MBP-OAIP3 fusion protein was eluted from the column with 300 mM imidazole (**Fig. 2.1C**, lane 8). Most of the fusion protein could be successfully cleaved with TEV protease to liberate free OAIP3 (compare lanes 9 and 10 in **Fig. 2.1C**). The OAIP3 liberated by TEV protease cleavage of the fusion protein was purified via RP-HPLC to obtain a single major peak (**Fig. 2.1D**). The purity

(>95%) of the peak collected was verified on analytical RP-HPLC (**Fig. 2.1D**, inset showing chromatogram). The asterisk in **Fig. 2.1D** denotes the peak with mass corresponding to the theoretical mass of OAIP3 (**Fig. 2.1D** inset showing MS spectrum).

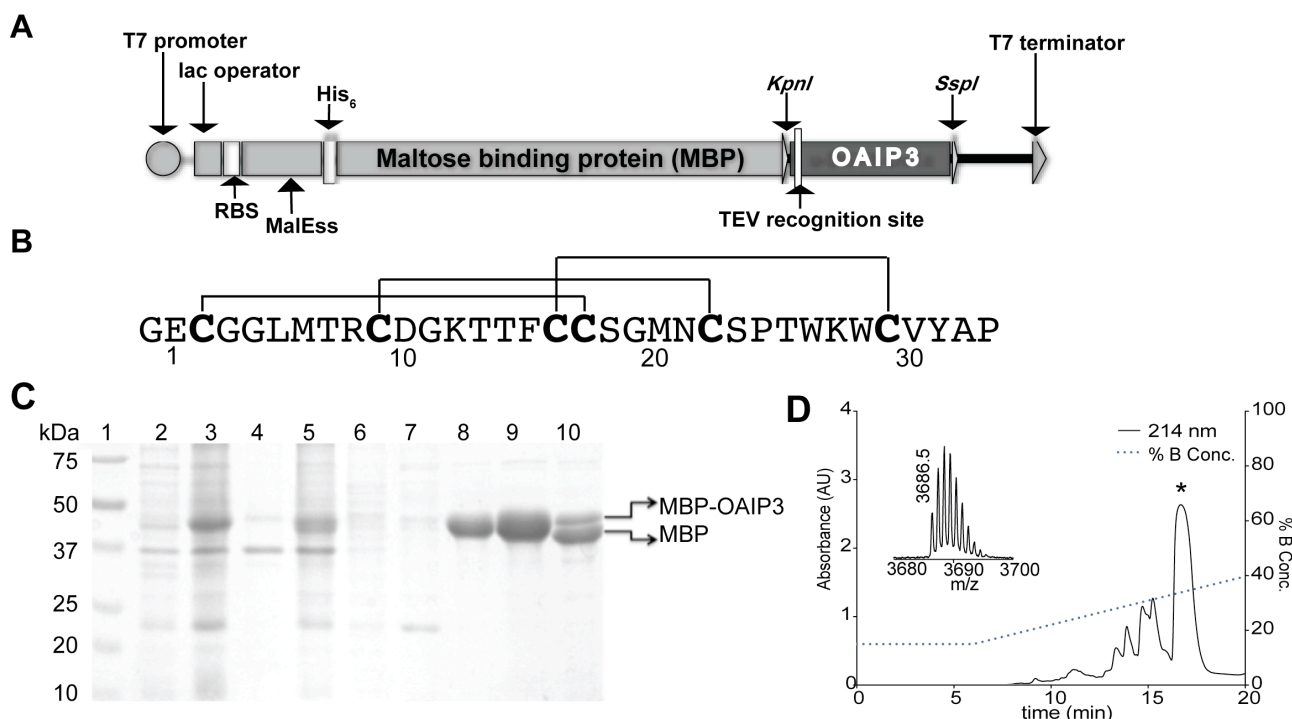


Figure 2.1. Expression and purification of recombinant OAIP3. **(A)** Schematic of the plasmid vector used for OAIP3 expression in *E. coli*. Important elements of the vector are shown (not to scale), including the ribosome binding site (RBS) and promoter and operator regions. **(B)** Amino acid sequence of recombinant OAIP3; lines above the sequence indicate disulfide bonds as determined from NMR analysis. **(C)** SDS-PAGE gel showing various stages in the expression and purification of recombinant OAIP3. The lanes (from left to right) are as follows: (1) molecular weight markers; (2) whole-cell extract before IPTG induction; (3) whole-cell extract after IPTG induction; (4) insoluble fraction after lysis of induced cells; (5) soluble fraction after lysis of induced cells; (6) flow-through from loading of soluble cell fraction onto Ni-NTA column; (7) eluate from wash of Ni-NTA column with 15 mM imidazole; (8) eluate from wash of Ni-NTA column with 250 mM imidazole; (9) eluted MBP-OAIP3 fusion protein prior to TEV protease cleavage; (10) MBP-OAIP3 fusion protein sample after TEV protease cleavage. **(D)** Chromatograms showing RP-HPLC purification of recombinant OAIP3. Asterisk denotes peak with mass corresponding to OAIP3 (3686.5 Da), as indicated by the mass spectrum shown in the inset.

Using the periplasmic expression system, a substantial quantity of recombinant OAIP3 was successfully produced which enabled characterisation of the peptide. The fusion protein was the major cellular product formed following IPTG induction, indicated by the single major protein band observed at ~43 kDa (**Fig. 2.1C**, compare lanes 2 and 3). The

majority of the fusion protein was found in the soluble fraction of the crude cell lysate (**Fig. 2.1C**, compare lanes 4 and 5). The His₆ tag allowed efficient purification of the fusion protein using nickel affinity chromatography, with minimal loss (**Fig. 2.1C**, lanes 6 and 7). Elution with 250 mM imidazole resulted in release of fusion protein from the Ni-NTA resin (**Fig. 2.1C**, lane 8) which was further concentrated with a 30 kDa molecular weight filter (**Fig. 2.1C**, lane 9). Liberation of OAIP3 from the fusion protein with TEV protease was ~90% efficient (**Fig. 2.1C**, lane 10). Both RP-HPLC and mass spectrometry confirmed the production of recombinant OAIP3 which eluted as a major peak in the RP-HPLC chromatogram with a mass that matched the theoretical oxidised mass of OAIP3 (**Fig. 2.1D**). The same approach was successfully employed to produce uniformly ¹³C/¹⁵N-labelled OAIP3 for NMR structure determination. Using this system, approximately 0.5 mg of pure recombinant peptide was obtained per litre of culture.

2.3.2 NMR structure determination

The structural integrity of recombinant ¹⁵N-labelled OAIP3 was examined by acquiring a 2D ¹H-¹⁵N heteronuclear single quantum coherence (HSQC) spectrum (**Fig. 2.2**). Spectra were acquired at 25°C on a Bruker 900 MHz spectrometer. The NMR spectrum revealed the expected number of backbone ¹H-¹⁵N connectivities as well as peaks for the sidechain amide groups of the two Trp residues (boxed and labelled “W-SC” in **Fig. 2.2**), sidechain ¹H-¹⁵N connectivities for the single Asn residue (connected by a dashed line and labelled “N-SC” in **Fig. 2.2**) and a single (folded) peak for the sidechain amide group of the Arg residue (labelled “R-SC” in **Fig. 2.2**). The excellent chemical shift dispersion in both the ¹H and ¹⁵N frequency dimensions is characteristic of a protein with a stable tertiary fold.

The structure of OAIP3 was determined using heteronuclear NMR spectroscopy with ¹³C/¹⁵N-labelled peptide. ¹H_N, ¹⁵N, ¹³C_α, ¹³C_β, and ¹³C' resonance assignments were obtained from analysis of amide-proton strips in 3D HNCACB, CBCA(CO)NH, and HNCO spectra. Sidechains assignments were based on 4D HCC(CO)NH-TOCSY, 3D ¹⁵N-HSQC NOESY and 3D ¹³C-HSQC NOESY spectra, with sidechain ¹H and ¹³C chemical shifts obtained primarily from 3D H(CC)(CO)NH-TOCSY and (H)CC(CO)NH-TOCSY spectra, respectively. ¹H-¹H distances were determined from signal intensities in 3D NOESY spectra. A long-range HNCO experiment was acquired to identify hydrogen bonds. All spectra were analysed using XEasy²⁰⁸. Backbone φ and Ψ dihedral angle restraints were

generated from analysis of chemical shifts using TALOS+²⁰⁴. These dihedral-angle restraints were used in conjunction with interproton distance restraints derived from NOESY spectra, hydrogen-bond restraints from the HNC0 experiment, and disulfide-bond restraints for structural calculations using CYANA 3.0²⁰⁵.

Three hundred structures were calculated from random starting conformations, then the 20 conformers with highest stereochemical quality as judged by MolProbity²⁰⁹ were selected to represent the solution structure of OAIP3 (**Fig 2.3A**). The structural ensemble has very high stereochemical quality as indicated with MolProbity²⁰⁹, with very few steric clashes (as indicated by the low clashscore: $8.7 \pm 2.1\%$), low percentage of Ramachandran outliers ($5.0 \pm 1.4\%$), and a low percentage of unfavorable sidechain rotamers ($16.4 \pm 4.2\%$) (**Table 2.1**). The final ensemble of 20 structures is precisely defined with RMSDs for the backbone and heavy atoms of 0.56 Å and 1.05 Å, respectively, over residues 2–33. The average MolProbity score of 3.09 places the ensemble in the 89th percentile (100th being the best) of structures in the MolProbity database (**Table 2.1**).

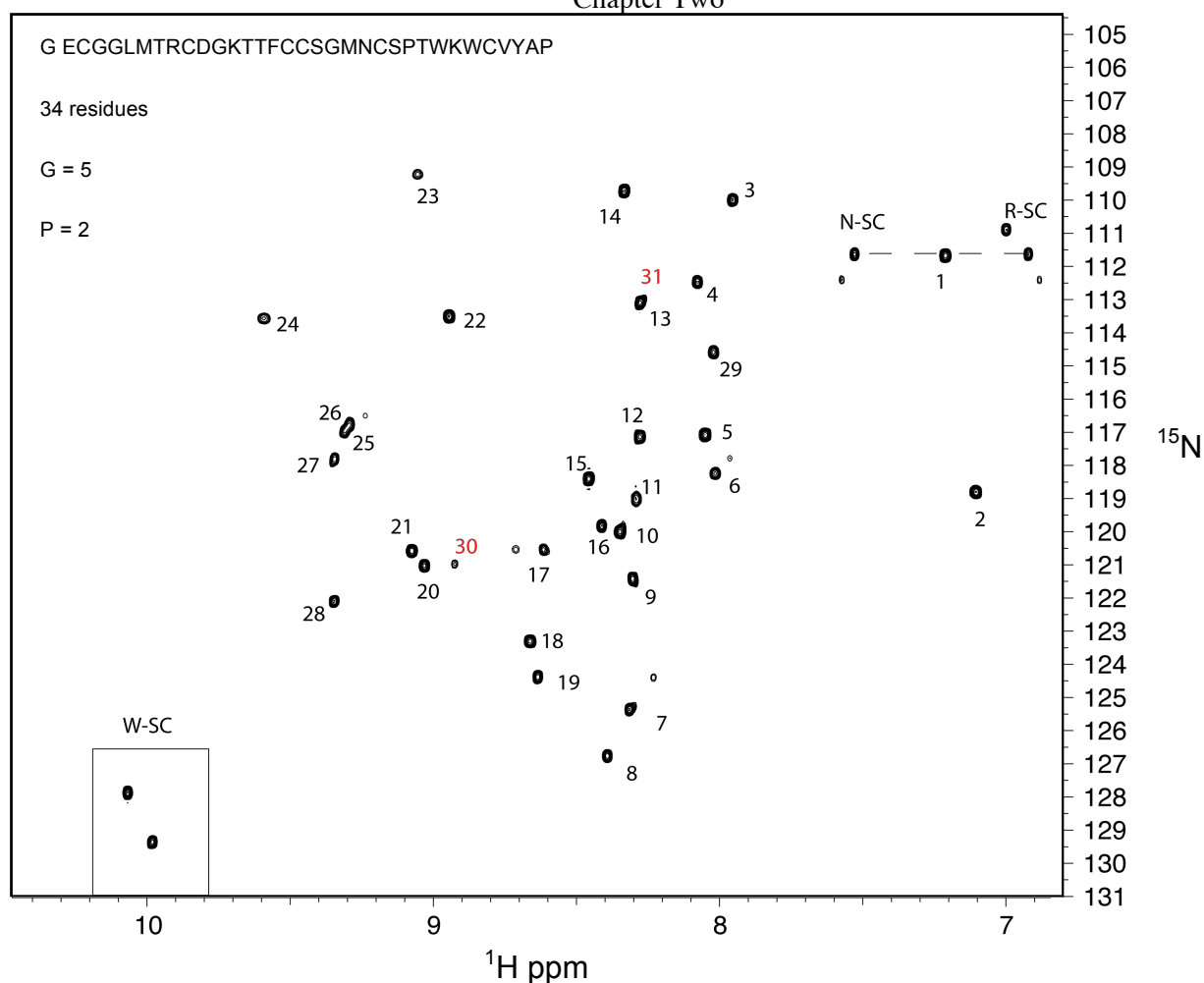


Figure 2.2. 2D ^1H - ^{15}N HSQC spectrum of OAIP3 acquired at 900 MHz. Peaks are labelled according to the residue number of OAIP3.

The structure comprises three disulfide bonds that form a classical inhibitor cystine knot (ICK) motif in which the Cys2–Cys17 and Cys10–Cys22 disulfide bonds and the intervening sections of polypeptide backbone forms a ring that is bisected by the Cys17–Cys30 disulfide bond (**Fig. 2.3B**, left). The structure comprises two antiparallel β -strands formed by residues 23–26 and 29–32. Eight hydrophobic residues are clustered on one face of the molecule to form a hydrophobic patch while four cationic residues are arranged in stack forming a positively-charged region (**Fig. 2.3B**, right).

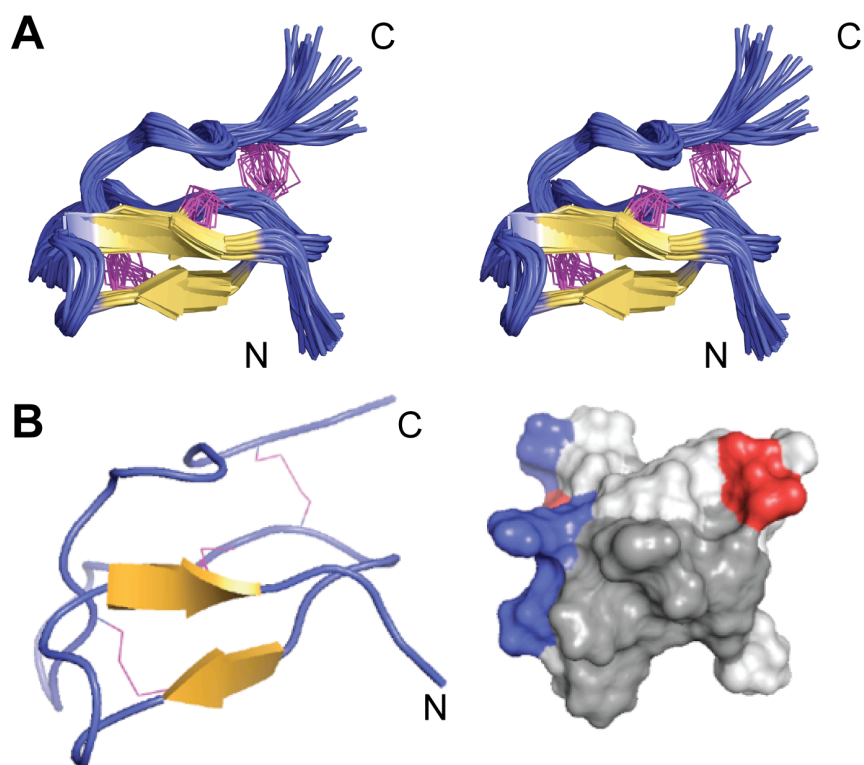


Figure 2.3. NMR solution structure of OAIP3. **(A)** Stereoview of the ensemble of 20 OAIP3 structures. The N- and C-termini are labelled, β -strands are shown in yellow, and disulfide bonds are magenta. **(B)**. Left: Ribbon representation of OAIP3 structure. β -Strands are shown in yellow and disulfide bonds are magenta. Right: Molecular surface of rOAIP3. Hydrophobic, anionic, and cationic residues are shown in grey, red, and blue respectively.

2.3.3 Sequence and structural homologs of OAIP3

A BLAST search of the OAIP3 sequence against the ArachnoServer database identified several SVPs with high sequence similarity (**Fig. 2.4**). OAIP3 is 72% identical to U₁-TRTX-Cg1d, a spider toxin identified through analysis of a venom-gland transcriptome from the Chinese fawn tarantula *Chilobrachys guangxiensis*²¹⁰. However, there is no activity information available for U₁-TRTX-Cg1d. Given the high level of sequence identity it can be predicted that U₁-TRTX-Cg1d is likely to be insecticidal. The next closest match with known activity is ω -TRTX-Asp2a, an inhibitor of Ca_v channels in rat cerebellar granule cells, isolated from the tarantula *Aphonopelma sp.*²¹¹. OAIP3 is 41% identical to U₂-TRTX-Hs1a and U₂-TRTX-Hs1b, two homologous SVPs from the Chinese bird spider *Haplopelma schmidti*²¹².

Table 2.1. Statistics for the OAIP3 structure.

statistical analysis of OAIP3 structure ¹	
Experimental restrains ²	
Interproton distance restrains	
Intraresidue	106
Sequential	137
Medium range (i - j < 5)	53
Long range (i - j ≥ 5)	99
Disulfide bond restrains	9
Dihedral – angle restrains	53
Total number of restrains per residue	11.6
R.m.s deviation from mean coordinate structure	
Backbone atoms (2 – 33)	0.56 ± 0.12 Å
All heavy atoms (2 – 33)	1.05 ± 0.11 Å
Stereochemical properties ³	
Residue in most favoured Ramachandran region (%)	83.18 ± 4.31
Ramachandran outlier (%)	5.00 ± 1.4
Poor rotamers (%)	16.43 ± 4.19
Clashscores ⁴	8.72 ± 2.11
Overall MolProbity score	3.05 ± 0.09
¹ All statistics are give as mean ± S.D	
² Only structurally relevant restrains, as defined by CYANA, are included.	
³ According to MolProbity (http://molprobity.biochem.duke.edu)	
⁴ Defined as the number of steric overlaps > 0.4 Å per thousand atoms	

A search for structural homologs of OAIP3 using the online DALI server (<http://ekhidna.biocenter.helsinki.fi/dali/>)²¹³ revealed a remarkable 47 structural matches with a statistically significant z score > 2. The best six matches are as shown in **Fig. 2.5**; five of these are Na_v channel modulators isolated from spider venoms. The closest matches were μ-TRTX-Hs2a, a potent inhibitor of neuronal tetrodotoxin (TTX)-sensitive Na_v channels, and Na_v channel targeting peptides isolated from *Agelenopsis aperta* (Western grass spider) and *Haplopelma hainanum* (Chinese Black Earth Tiger tarantula). Interestingly, there is a good overlay between the OAIP3 structure and the pharmacophore region of μ-TRTX-Hs2a²¹⁴. The structural similarities between OAIP3 and several Na_v toxins suggest that the molecular target of OAIP3 is likely to be insect Na_v channels. Interestingly, it is also structurally similar to M-TRTX-Gr1a, isolated from *Grammostola rosea* (Chilean rose tarantula). M-TRTX-Gr1a was initially identified as a blocker of mechanosensitive ion channels²¹⁵, but more recently it has been shown to also inhibit Na_v channels²¹⁶.

Peptide	Sequence	% identity
OAIP3 (native)	ECGGLMTRCDGKTTFC ^C SGMNC ^S SPTWKWC ^V YAP-NH ₂	
rOAIP3	GE ^C GGLMTRCDGKTTFC ^C SGMNC ^S SPTWKWC ^V YAP	
U ₁ -TRTX-Cg1d	G ^C DDLMDGCDGKSTFC ^C SGFNCSPTWKWC ^V YARPGRR	72
TRTX-Asp2a	^C AEFQSKCKKDSE- ^C CGTLECSPTWKWC ^V YPSPF	42
U ₁ -Hs1b	D ^C AGYMRECKEKL-- ^C CSGYV ^C SSRWKWC ^V LPPAP	41
U ₂ -Hs1b	D ^C AGYMRECKEKL-- ^C CSGYV ^C SSRWKWC ^V LPPAPW-NH ₂	41

Figure 2.4. Sequence alignment of OAIP3 with orthologs from other spider venoms

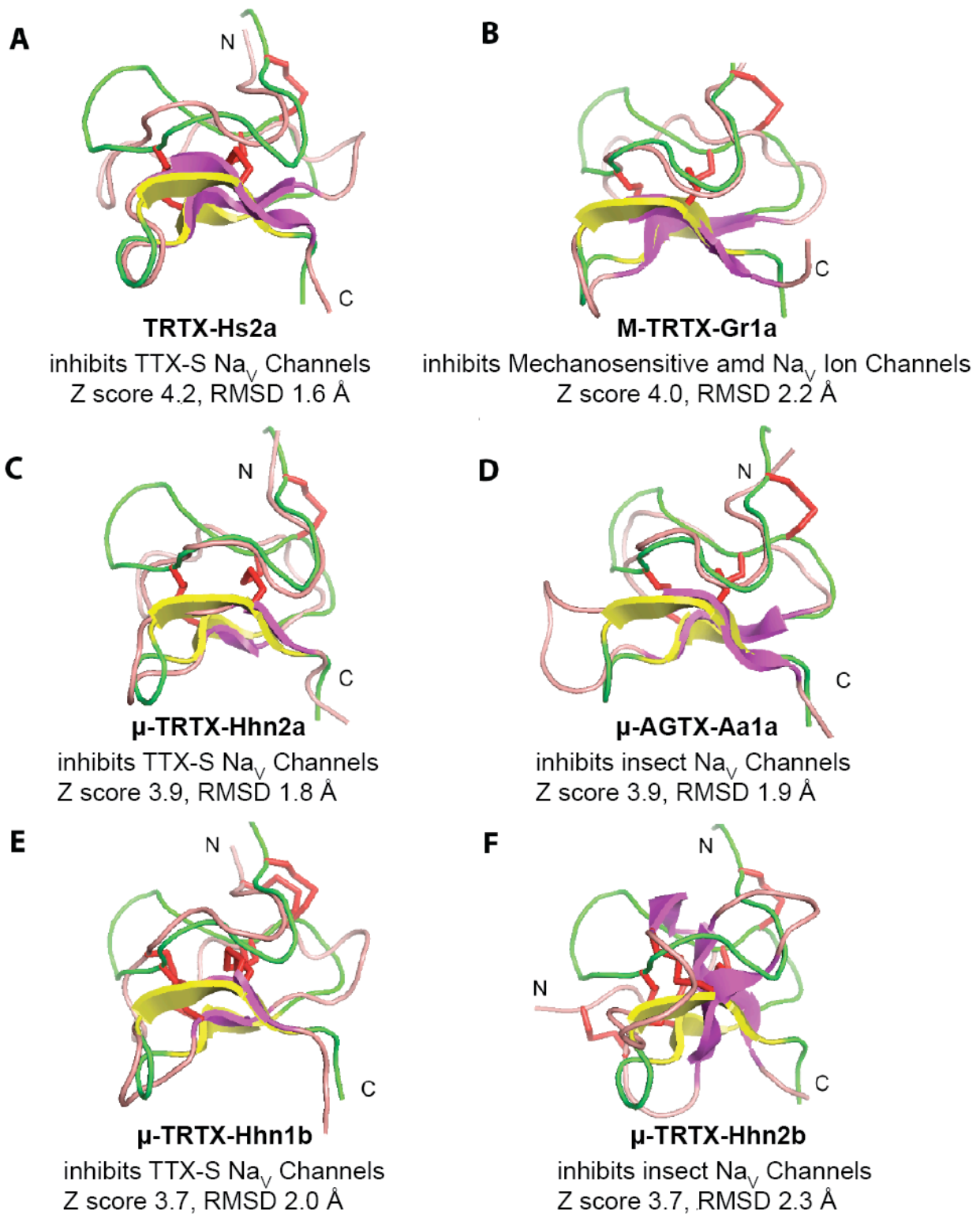


Figure 2.5. Structural homologs of OAIP3. Alignment of the structure of OAIP3 (green) with the top six structural homologs (pink) as ranked by the Dali server²¹³. The molecular target of each structural homolog is indicated, as is the Z score and RMSD of the alignment. Disulfide bonds are shown as solid tubes (red) and the N- and C-termini are labelled.

2.3.4 Insecticidal activity of recombinant OAIP3

The insecticidal activity of **native** OAIPs was previously assessed using mealworms and termites¹⁹⁹. 100% mortality was observed for OAIP1 and OAIP3 while OAIP2 caused ~25% mortality and OAIP4 ~50% mortality when injected into mealworms¹⁹⁹. All OAIPs, except OAIP2, were less potent when fed to termites. Initial testing of native OAIP3 yielded potent insecticidal activity when it was injected in mealworms, with 100% mortality at a dose of ~3 pmol/g, and when fed to termites with >70% mortality at a dose of ~350 pmol/g (**Fig. 2.6A**).

When injected at a dose of 0.4 nmol/g, **recombinant** OAIP3 caused ~26% of mealworms to become moribund after 48 h, but this was not a significantly higher level than seen in controls (**Fig. 2.6B**). The number of affected insects increased to ~53% at a dose of 7.6 nmol/g (**Fig. 2.6B**), but this is still significantly lower activity than observed for the native peptide. The reduced potency observed for recombinant OAIP3 suggests that the C-terminal amidation present in the native peptide is crucial for activity and/or addition of a non-native glycine residue at the N-terminus of the recombinant peptide deleteriously affects peptide activity. Future structure-activity relationship studies will be required to ascertain the reasons for the reduced potency of the recombinant OAIP3.

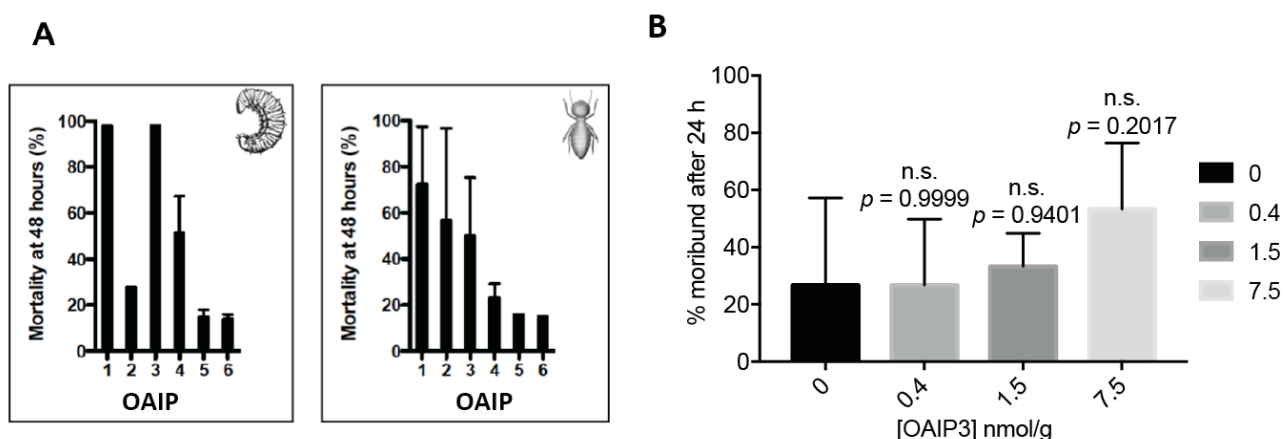


Figure 2.6. Insecticidal activity of OAIPs in mealworms and termites. **(A)** Activity of native OAIP 1-5 when injected into mealworms (3 pmol/g) and when fed to termites (350 pmol/g). Data from Ref. ¹⁹⁹. **(B)** Percentage of moribund mealworms (dead or paralysed) 48 h after injection of recombinant OAIP3 ($n = 5$, in triplicates, mean \pm SD) (one-way ANOVA, $p = 0.2187$, n.s.). Assays were performed by Dr Volker Herzig (IMB, University of Queensland).

2.4 Discussion

2.4.1 Production of recombinant OAIP3

Detailed structure-function characterisation of peptides requires a substantial quantity of material, especially for structure determination using NMR. Thus, I used an efficient *E. coli* periplasmic expression system for production of recombinant OAIP3, and used this system to produce isotopically-labelled peptide for determination of its solution structure using NMR spectroscopy. Functional characterisation was also carried out to determine the potency of the recombinant peptide.

The presence of multiple disulfide bonds in SVPs is often challenging for SPPS and recombinant peptide production. Peptide synthesis requires technical expertise and specialised equipment as it involves potentially dangerous chemicals such as TFA or hydrofluoric acid (HF). Moreover, syntheses involving long-chain amino acid are often challenging due to steric hindrance and unwanted side-reactions such as premature termination. Lastly, extensive optimisation of folding conditions is often required to obtain correctly folded synthetic peptide²¹⁷.

An alternative to SPPS is recombinant production of SVPs in bacteria. *E. coli* is often the bacterium of choice for recombinant protein expression due to its fast doubling time (~20 min), ability to grow in high density, and scalability to large-scale fermenters for increasing production yields; this translates into higher yields at lower cost of production and therefore better economic returns. Recombinant expression also allows low-cost production of isotopically-labelled peptides for high-resolution structure determination using NMR²⁰².

However, production of cysteine-rich peptides is difficult as the reducing cytoplasmic environment is prohibitive for the formation of disulfide bonds. In contrast, the *E. coli* periplasm contains the endogenous cellular machinery for disulfide-bond formation²¹⁸. Hence we used an expression vector containing a signal peptide sequence that allowed export of the OAIP3 fusion protein into the *E. coli* periplasm. This led to the production of a single, oxidised isoform of recombinant OAIP3, highlighting the success of this expression strategy.

The successful production of OAIP3 in bacteria indicates that it might be possible to engineer genetically-modified (GM) crops that express OAIP3 for improved resistance against insect pests. This strategy has been used for ω -hexatoxin-Hv1a (Hv1a), an SVP isolated from the funnel-web spider *Hadronyche versuta* that is potentially insecticidal⁴⁹, but which lacks oral efficacy²¹⁹. To overcome this problem, Hv1a was fused to snowdrop lectin (GNA) which enabled movement of the fusion protein across the insect gut into the hemolymph, allowing it to reach its targeted site in the insect nervous system and thereby enhancing its oral potency²²⁰. Transgenic *Arabidopsis* expressing the GNA/Hv1a fusion protein displayed markedly improved resistance against the green peach aphid (*Myzus persicae*)²²¹. In contrast with Hv1a, the intrinsic oral efficacy of OAIP3 makes it a potential candidate for generation of GM-crops without the need for fusion to a carrier protein.

2.4.2 Determination of the 3D structure of OAIP3

Isotopically-labelled OAIP3 was produced for structure determination using NMR. The NMR experiments enabled assignment of the chemical shifts of all NMR-observable proton (¹H), nitrogen (¹⁵N) and carbon (¹³C) atoms, which typically allows a higher-resolution structure to be obtained than is possible with 2D homonuclear NMR techniques²²². The NMR studies revealed that OAIP3 has a canonical ICK fold with the C1–C4 and C2–C5 disulfide bonds and the intervening sections of polypeptide backbone forming a loop that is pierced by the C3–C6 disulfide bond. ICK peptides are known to be highly resistant to thermal, chemical and proteolytic degradation^{12, 52}. Intrinsic resistance to proteases, which remains to be proven experimentally, may contribute to the oral efficacy of native OAIP3. However, the alkaline environment of some insect guts (mostly lepidopterans) is unfavourable for the stability of ICK peptides due to the possibility of disulfide-bond shuffling¹², and this will need to be investigated in future experiments with OAIP3.

The search for structural homologs of OAIP3 using the DALI server identified many homologs. Remarkably, the top six hits are all spider-venom peptides that are known to modulate the activity of insect or vertebrate Na_v channels. However, recombinant OAIP3, at concentrations up to 1 μ M, had no effect on currents mediated by the BgNa_v1 from the German cockroach *Blattella germanica* heterologously expressed in *Xenopus* oocytes (electrophysiology experiments performed by Dr Frank Bosmans, Johns Hopkins University, USA; results not shown). This does not necessarily imply that insect Na_v

channels are not the target of OAIP3; as discussed in Section 2.3.4 above, the lack of C-terminal amidation and the additional non-native N-terminal glycine residue may have contributed to the reduced *in vivo* potency of OAIP3 and the lack of activity on the BgNa_v1 channel. It has been shown in many cases that C-terminal amidation is required for maintaining the biological activity of neuropeptides and ion channel modulators^{214, 223}. The C-terminal amide was shown to be critical for μ -TRTX-Hh2a activity against the human Na_v1.7 channel. Recombinant μ -TRTX-Hh2a (with C-terminal acid, IC₅₀ ~727 nM) was 66-fold less potent against hNa_v1.7 compared to synthetic peptide with a C-terminal amide (IC₅₀ ~11 nM). Interestingly, the activity of the recombinant peptide was partly recovered (IC₅₀ ~190 nM) by a one-residue (glycine) extension at the C-terminus to mimic the native C-terminal amide²²⁴.

A marked difference in insecticidal activity between close homologs was also observed in U₂-TRTX-Hs1b and U₂-TRTX-Hs1a²²⁵, isolated from *Haplopelma schmidtii* with 42% sequence identity to OAIP3 (**Fig. 2.4**). U₂-TRTX-Hs1a weakly inhibits insect Na_v channels in cockroach dorsal unpaired median (DUM) neurons with an IC₅₀ of ~1.1 μ M and causes reversible paralysis in cockroaches with a PD₅₀ of ~50 nmol/g²²⁵. In comparison, U₂-TRTX-Hs1b, which differs by a single C-terminal residue truncation and amidation, had no effect on cockroaches (up to 109 nmol/g)²²⁵.

The addition of an N-terminal glycine to OAIP3 sequence (to aid TEV protease cleavage) may result in deleterious effects on activity. However, we have routinely produced recombinant peptides with a non-native serine or glycine without observing loss of activity. Hence, the stark differences in potency observed in native and recombinant OAIP3 may indicate that C-terminal amidation is crucial for OAIP3 activity.

2.5 Conclusions

In summary, this chapter described the production and characterisation of an insecticidal peptide, OAIP3, isolated from the venom of *S. plumipes*. Recombinant OAIP3 was produced in high yield as a single isoform using a bacterial periplasmic expression system. Structure determination using NMR indicated that OAIP3 has a canonical ICK fold commonly observed in spider-venom peptides. The search for structural homologs of OAIP3 identified several structurally related Na_v channel modulators from other spider

venoms. Both sequence and structural alignments suggest that OAIP3 is likely to target insect Na_v sodium channels. The insecticidal activity of recombinant OAIP3 was significantly less than native OAIP3, which we attribute to the loss of C-terminal amidation in the recombinant peptide. Overall, the structure-function characterisation of OAIP3 has provided informative insights for the development of bioinsecticides from spider venoms.

Chapter Three

NB. This chapter is presented as a finalised manuscript and formatted as per required for submission to ACS Chemical Biology

Discovery, molecular interaction and stability studies of a second acid-sensing ion channel 1 modulator from tarantula venom

Sing Yan Er^{1,#}, Ben Cristofori-Armstrong^{1,#}, Pierre Escoubas², and Lachlan D Rash^{1,3,*}

¹Institute for Molecular Bioscience, The University of Queensland, St. Lucia, QLD 4072, Australia, ²VenomeTech, 473 Route des Dolines — Villa 3, 06560 Valbonne, France, ³School of Biomedical Science, The University of Queensland, St. Lucia, QLD 4072, Australia

#These authors contributed equally to this work

*Address for correspondence:

Dr Lachlan D Rash: Phone: +61 7 3346-2985; Email: l.rash@uq.edu.au.

ABSTRACT

Acute pharmacological inhibition of acid-sensing ion channel 1a (ASIC1a) is efficacious in rodent models of neurological diseases such as stroke and multiple sclerosis. Thus, ASIC1a is a promising therapeutic target and selective ligands that modulate it are invaluable research tools and potential therapeutic leads. Spider venoms have provided an abundance of voltage-gated ion channel modulators, however, only one ASIC modulator (PcTx1) has so far been isolated from this source. Here we report the discovery, characterization, and chemical stability of a second spider venom peptide that potently modulates ASIC1a and 1b and investigate the molecular basis for its subtype selectivity. p-TRTX-Hm3a is a 37-amino acid peptide isolated from Togo starburst spider (*Heteroscodra maculate*) venom with substantial sequence similarity to PcTx1, albeit three residues shorter at the C-terminus. Hm3a pH-dependently inhibited ASIC1a with an IC_{50} of 1–2 nM and potentiated ASIC1b with an EC_{50} of 50 nM similar to PcTx1. Using ASIC1a to ASIC1b point mutants in rat ASIC1a revealed that E177 and R175 in the palm region opposite α -helix 5 play an important role in the Hm3a-ASIC1 interaction and contribute to the subtype-dependent effects of the peptide. Despite the high sequence similarity with PcTx1, Hm3a showed higher levels of thermal, serum, and cerebrospinal fluid stability over 48 hours. Overall, Hm3a represents a potent, highly stable tool for the study of ASICs and use in structure-activity studies to define the interaction of peptides with this novel channel family.

Growing knowledge on the molecular basis of various channelopathies and neurological disorders had sparked intense interest in the discovery and development of ion channel modulators as therapeutics and pharmacological tools¹⁻². Spiders, in particular, have proved to be a rich source of such modulators. Their venoms contain numerous biologically active peptides that potently target a variety of ion channels³⁻⁴. As such, peptides isolated from spider venoms have been widely used to dissect the molecular mechanisms of channel function and their role in biological processes and have been instrumental for improving our understanding of ion channels⁵⁻⁷. In this respect, the acid-sensing ion channels (ASICs) are no different with a spider venom peptide being the first, and still the most potent, selective modulator known for ASICs.

ASICs are chordate-specific members of the degenerin/epithelial sodium channel family that are widely distributed in the nervous system and many non-neuronal cells⁸. They are primary mammalian acid sensors and as such are activated by protonation⁹. Six ASIC subtypes are known (ASIC1a/b, ASIC2a/b, ASIC3 and ASIC4), which can assemble as functional homotrimeric (ASIC1a/b, ASIC2a and ASIC3 only) or heterotrimeric channels¹⁰. Each subunit consists of a large extracellular domain, two transmembrane helices, and short intracellular N- and C-termini. The combination of subunits in each channel affects the pH sensitivity, pharmacology, and kinetics of activation and desensitization¹⁰. ASIC1a is the most abundant ASIC subunit in the mammalian central nervous system. Unlike other ASICs, ASIC1a is also permeable to Ca^{2+} , a property that has been associated with ASIC1a's role in acidosis-induced neuronal injury¹¹⁻¹². ASICs have been implicated with a variety of pathophysiological conditions such as inflammatory and neuropathic pain¹³⁻¹⁵, psychiatric illness¹⁶, multiple sclerosis¹⁷, epileptic seizure termination¹⁸ and ischemic stroke¹⁹, hence are considered promising therapeutic targets^{11, 20}.

Although several small molecules have been demonstrated to modulate ASIC activity, they lack subtype specificity and potency, and thus are limited in their usefulness as pharmacological tools. In contrast, venom peptides are often extremely potent and can have very high selectivity for neuronal targets³. To date, six ligands targeting various ASIC subtypes have been isolated from animal venoms²¹. The prototypical and therefore most studied ASIC ligand is the spider venom peptide, PcTx1 from the spider *Psalmopoeus cambridgei*²². PcTx1 inhibits homomeric ASIC1a with an IC_{50} of ~0.9 nM, and stabilises the open state of ASIC1b. More recently it has been shown to also inhibit heteromeric ASIC1a/2b and ASIC1a/2a channels²³⁻²⁴. The only other inhibitory peptide ligands of

ASIC1 include the mamblagins, from the Mamba snakes (*Dendroaspis* spp.), which have been shown to inhibit ASIC1a and ASIC1b containing channels with IC₅₀ values between 11 and 300 nM^{21, 25}.

From a panel of spider venoms, we observed ASIC1a inhibitory activity from the venom of the Toga starburst spider (*Heteroscodra maculata*). Here, we describe the isolation, recombinant expression and characterisation of a second potent inhibitor of ASIC1a from venom of *Heteroscodra maculata*. This venom-peptide, named π -theraphotoxin-Hm3a (hereafter Hm3a), was pharmacologically characterized to determine its ASIC subtype-selectivity, binding site, mechanism of action and stability in biological fluids.

RESULTS AND DISCUSSION

ASIC1 has been associated with many pathophysiological conditions as a result of acidosis and has been shown to be a promising drug target²⁰. However, the current array of ASIC1 modulatory ligands available as selective pharmacological tools and therapeutic leads is extremely limited. The difficulty in developing more selective small molecule ASIC inhibitors as therapeutic leads is illustrated by a series of classical medicinal chemistry studies by Merck. Three studies using different starting scaffolds all resulted in more potent molecules, however, all had significant off-target effects resulting in substantial sedation in animal studies²⁶⁻²⁸. Based on the discovery of PcTx1 in a spider venom²² we hypothesized that spider venoms should be a valuable source of additional novel ASIC modulators. Discovery of novel ligands, and understanding the molecular basis for differences in their biological properties (such as structural and chemical stability) and functions provides valuable insight to develop improved ligands.

Identification and Purification of Hm3a

A panel of spider venoms were screened for activity on rat ASIC1a channels expressed in *Xenopus laevis* oocytes using two-electrode voltage-clamp (TEVC) electrophysiology. Venom from *Heteroscodra maculata* (1/1000-fold dilution) resulted in robust (>90%) inhibition of ASIC1a. Fractionation of the crude venom using reversed-phase (RP) HPLC yielded 44 fractions, indicating the high complexity of *H. maculata* venom. Assay-guided fractionation led to the identification of a minor, early-eluting peak, Fraction 12, that

inhibited rASIC1a currents (**Fig. 3.1A**). Subsequent purification of Fraction 12 led to isolation of a single peptide, with an observed monoisotopic $M+H^+$ of 4285.05 (**Fig. 3.1B**). The peptide was named p-TRTX-Hm3a, hereafter Hm3a, according to a rational nomenclature system for naming peptide toxins from venomous animals²⁹.

The full-length amino acid sequence of Hm3a was determined by a combination of N-terminal Edman degradation and tandem mass spectrometry. The theoretical oxidized monoisotopic m/z ($M+H^+ = 4285.03$) of the Hm3a sequence matched the observed monoisotopic mass suggesting the presence of a free carboxylic acid at the C-terminus and three disulfide bonds. A BLAST search on the ArachnoServer database³⁰ revealed that Hm3a shares 82% identity with PcTx1, the prototypical ASIC1a inhibitor from *Psalmopoeus cambridgei* venom (**Fig. 3.1C**). Hm3a differs from PcTx1 by five point mutations and a three residue C-terminal truncation. Native Hm3a is highly potent on rASIC1a, inhibiting acid-evoked currents with an IC_{50} of 2.6 ± 1.3 nM when applied at pH 7.45 (**Fig. 3.1D**). Due to the high sequence identity, conserved cysteine framework, and similar pharmacology between Hm3a and the inhibitor cysteine knot (ICK) fold peptide PcTx1 (PDB: 2KNI), it is highly likely that Hm3a also conforms to the ICK fold (**Fig. 3.1E**). Despite being identified 15 years ago, PcTx1 remained the only known peptide isolated from spider venom that targets ASICs. Moreover, the relatively small molecular weight of PcTx1 or Hm3a allows for more efficient production by recombinant expression or chemical synthesis.

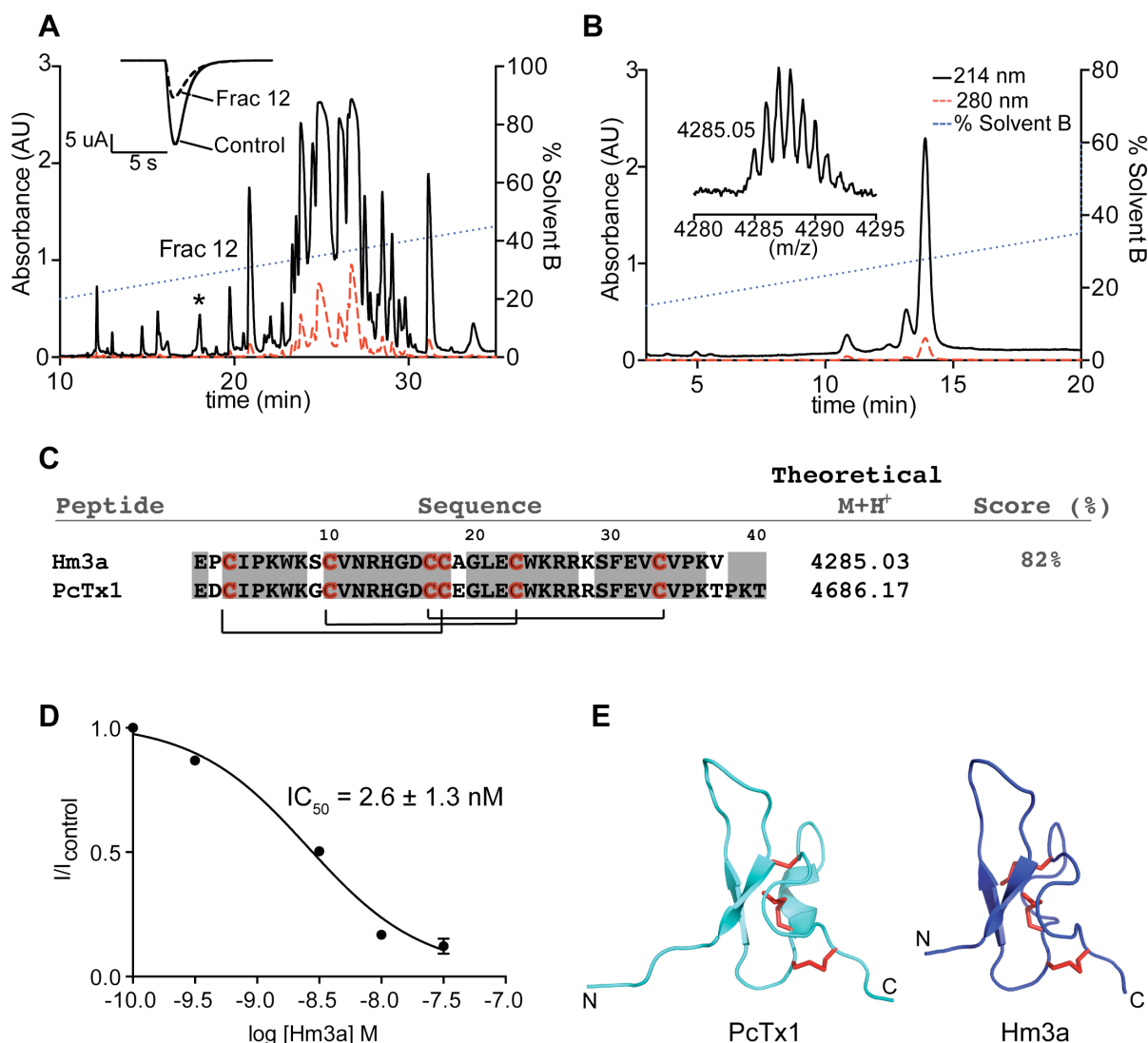


Figure 3.1. Isolation of Hm3a from *H. maculata* venom. **(A)** RP-HPLC chromatogram of crude *H. maculata* venom. The asterisk denotes the Hm3a containing fraction. Inset shows the effect of Fraction 12 on rASIC1a expressed in *Xenopus* oocytes. **(B)** Chromatogram showing the final purification step of native Hm3a and MALDI-TOF MS spectrum showing a monoisotopic mass, $M+H^+$ of 4285.05. **(C)** Full amino acid sequence of Hm3a aligned with PcTx1 (non-conserved residues are in bold, cysteine residues are shown in red). **(D)** Concentration-effect curve for inhibition of rASIC1a by native Hm3a ($n = 6$; error bars denote SEM). Fitting the Hill equation to the data yielded an IC_{50} of 2.6 ± 1.3 nM. **(E)** Three-dimensional homology model of Hm3a based on PcTx1 (PDB: 2KNI). Disulfide bridges shown in red, N- and C- termini are as indicated.

Recombinant Production of Hm3a

In order to obtain sufficient material to carry out further pharmacological characterization of Hm3a, we used an *Escherichia coli* recombinant expression system that we have previously employed to produce many disulfide rich venom peptides including PcTx1³¹⁻³². Following IPTG induction, the Hm3a-fusion protein was the dominant cellular protein

present (**Fig. 3.2A**). Cleavage from the fusion protein and purification using RP-HPLC resulted in a single peptide isoform, with a final yield of ~1 mg of correctly folded peptide per liter of bacterial culture at >98% purity (determined using RP-HPLC and MS) (**Fig. 3.2B**). The observed $M+H^+$ (4372.58) was in accordance with the calculated value (4372.06) for Hm3a with an additional N-terminal serine left from the TEV recognition site (**Fig. 3.2B insert**).

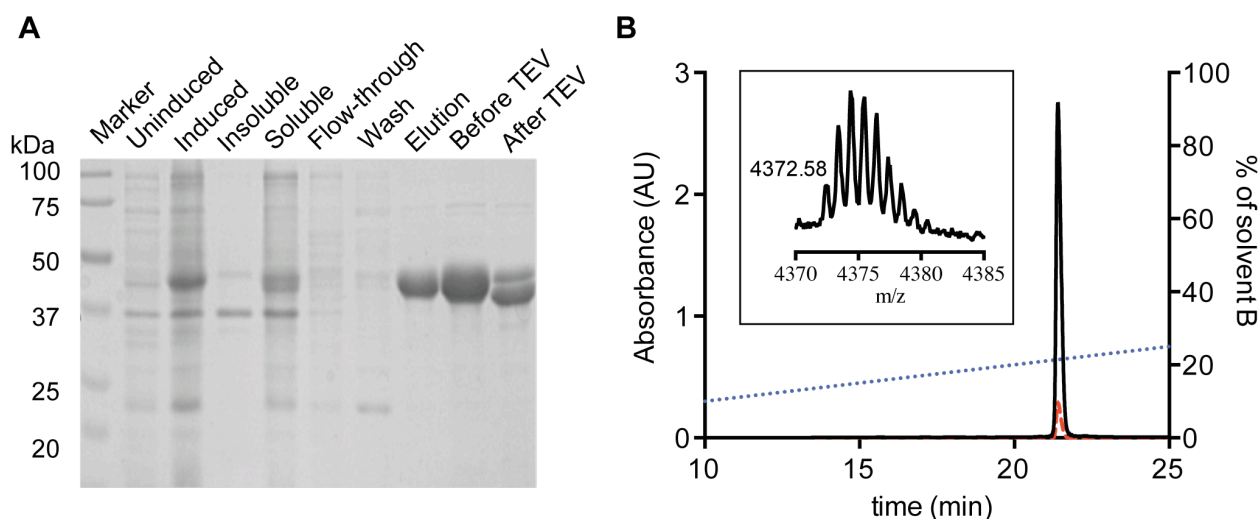


Figure 3.2. Production and purification of recombinant Hm3a were performed by Mr Ben Cristofori-Armstrong. **(A)** SDS-PAGE gel showing the expression, purification and TEV cleavage of the Hm3a-MBP fusion protein. The lanes are labeled as follows: Marker = 1 kDa protein molecular weight marker; Uninduced = whole-cell extraction before induction; Induced = whole-cell extract after induction; Insoluble = the insoluble fraction after cell lysis; Soluble = soluble fraction after cell lysis; flow-through = the flow-through after loading to Ni-NTA; Wash = the Ni-NTA flow-through after 15 mM imidazole wash; Elution = the Ni-NTA after 250 mM imidazole wash; Before TEV = concentrated sample before addition of TEV protease; After TEV = concentrated sample after addition of TEV protease. **(B)** RP-HPLC chromatogram of purified recombinant Hm3a. Inset is a MALDI-TOF mass spectrum showing the monoisotopic $M+H^+$ (observed, 4372.58; calculated 4372.06).

Effects of Hm3a on ASICs

The potency and selectivity of Hm3a was assessed using TEVC electrophysiology on oocytes expressing homomeric rASIC1a, rASIC1b, rASIC2a, rASIC3, human ASIC1a, hASIC1b, and heteromeric rASIC1a/ASIC1b (**Fig. 3.3A, 3.3B and 3.3C**). Recombinant Hm3a was similarly potent to the native peptide, causing rapid and reversible inhibition of rASIC1a with an IC_{50} of 1.3 ± 0.2 nM (**Fig. 3.3A**) confirming that the identified sequence is indeed the active peptide and is folded correctly. Furthermore, it shows that the addition of an extra residue on the N-terminus (the serine from the TEV cleavage) has little effect on

the inhibitory activity of the peptide, consistent with the well tolerated addition of a Tyr to the N-terminus of PcTx1³³. Having ascertained the identity and structural conformation, the remaining characterization studies of Hm3a were performed using recombinant peptide. Hm3a is highly selective for ASIC1, with no observable effect on rASIC2a or rASIC3 when tested at concentrations up to 10 μ M (**Fig. 3.3A**). In stark contrast, Hm3a strongly potentiated rASIC1b (~4-fold increase in amplitude) with an EC₅₀ of 46.5 \pm 6.2 nM (**Fig. 3.3B**) as has previously been reported for PcTx1³⁴. The potentiating effect was also observed on heteromeric rASIC1a/ASIC1b channels with higher potency (EC₅₀ of 17.4 \pm 0.5 nM), but lower efficacy (less than 2-fold increase in current amplitude) as compared to homomeric rASIC1b (**Fig. 3.3B**).

We next assessed species-dependent effects of Hm3a on ASIC1. Similar to the rat isoforms, Hm3a also inhibited human ASIC1a and potentiated hASIC1b; however, was ~30-fold, and ~3.8-fold less potent, respectively, than on the rat isoforms (**Fig. 3.3C**). The Hill coefficients from the concentration-effect curves of Hm3a on both rat and human ASIC1a and ASIC1b are 1.3–1.6, suggesting positively cooperative binding of more than one Hm3a peptide per ASIC1 trimer. This is consistent with the co-crystal structures of cASIC1 and PcTx1 that showed three PcTx1 peptides bound per channel³⁵⁻³⁶.

In the study by Chen *et al.*³⁴, that first demonstrated the potentiation of ASIC1b by PcTx1, they were unable to determine an accurate EC₅₀ as a plateau in the PcTx1 induced potentiation effect was not reached (likely due to the high concentrations required and the high cost of commercially available peptides). Here, we were able to show a maximal response in Hm3a potentiation of both rat and human ASIC1b and determine a more robust EC₅₀ value. PcTx1 has been shown to inhibit both ASIC1a homomers²² as well as rASIC1a/ASIC2b and rASIC1a/ASIC2a heteromers²³⁻²⁴, however no activity has been reported on rASIC1a/ASIC1b heteromers. Our results indicate that rASIC1a/ASIC1b heteromers are sensitive to Hm3a in the mid-nanomolar range. A better understanding of the interaction of these peptides with both ASIC1b and ASIC1a/1b heteromers is crucial when they are used as ASIC1a inhibitors in animal studies because both ASIC1a and ASIC1b are highly expressed in the peripheral nervous system in rodents³⁷. Thus, the use of high concentrations of Hm3a or PcTx1 may lead to confounding results, and possible undesirable side-effects because inhibition of ASIC1b has caused analgesic effects on inflammatory and nociceptive pain models of ASIC1a-knockout mice, indicating the involvement of ASIC1b in pain²⁵.

Despite the high sequence identity of Hm3a to PcTx1, Hm3a is slightly less potent on rASIC1a (~3-fold compared to PcTx1 in our previous studies) (**Fig. 3.1D, 3.3A, 3.5C**)^{32, 38}. From our previous structure-activity studies on PcTx1, we have shown that truncation of the three C-terminal residues (Pro38Lys39Thr40) resulted in a ~4-fold decrease in activity³⁸. Furthermore, a P38A mutation of PcTx1 was also ~4-fold less potent than wild-type PcTx1, leading us to the conclusion that the interaction made by Pro38 in PcTx1 could account for the slight loss in activity observed in these variants³⁸. Being equivalent in length to the Δ 3C variant of PcTx1, Hm3a also lacks a proline at position 38. Hence, we hypothesized that the potency of Hm3a on rASIC1a could be enhanced by the addition of a proline at the C-terminus (Hm3a_P38). A plasmid encoding the Hm3a_P38 variant was produced by site-directed mutagenesis and the peptide was recombinantly produced. Hm3a_P38 had an IC₅₀ of 0.4 ± 0.11 nM (**Fig. 3.3D**) or a 3.25-fold increase in potency as compared to wild-type Hm3a, in complete agreement with our prediction.

Extensive mutagenesis of PcTx1^{32, 38}, along with two co-crystal structures in complex with chicken ASIC1³⁵⁻³⁶ have been instrumental in defining the PcTx1 pharmacophore. Three of the residue differences between PcTx1 and Hm3a (D2P, G9S, and E19A) were not identified as potential contacts in structural studies. As a result, the effect of these mutations in PcTx1 have not been studied, and here we show that these mutations do not appear to be crucial for activity at rASIC1a. Thr37 of PcTx1 was identified as a crystal contact, however a PcTx1_T37A mutant was shown to be equipotent with wild-type PcTx1³⁸, in good agreement with the Hm3a potency (Thr37 is a Val in Hm3a, see Figure 1C). The only residue difference between Hm3a and PcTx1 that falls within the key pharmacophore residues was R28K. Arg28 makes multiple channel contacts and the PcTx1_R28A mutant had 14.5-fold lower activity on rASIC1a³⁸. In the case of Hm3a, the conservative mutation of Arg to Lys at position 28 appears to have little to no deleterious effect on peptide activity, thus the substitution is both functionally and structurally neutral. Although Lys has one less amino group, full retention of activity suggests that not all the interactions proposed in crystal studies are making energetically important contributions.

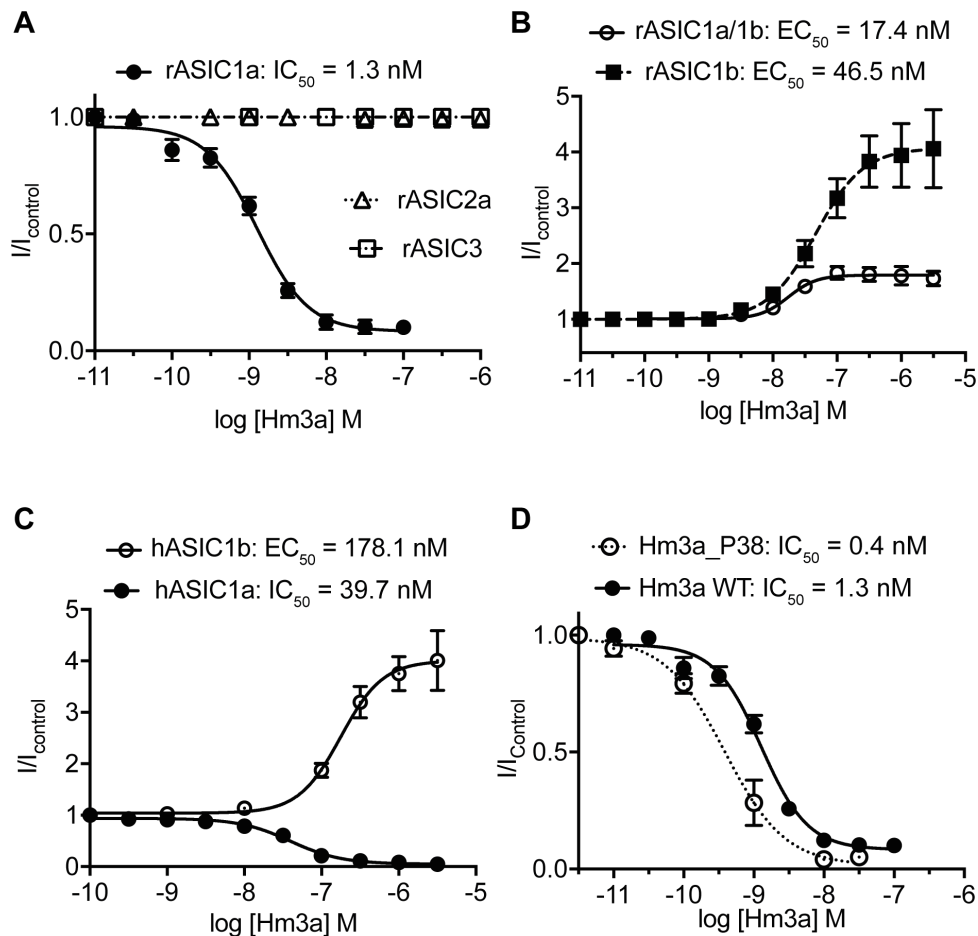


Figure 3.3. Concentration-effect curves of Hm3a for (A) homomeric rASIC1a, 2a, and 3 ($n = 6-10$), and (B) homomeric rASIC1b and heteromeric rASIC1a/ASIC1b channels ($n = 6$) ($p = 0.052$, $F = 8.069$). (C) Concentration-effect curves of Hm3a for homomeric hASIC1a and hASIC1b ($n = 7$) ($p = 0.0029$, $F = 13.34$). (D) Concentration-effect curves of wild-type Hm3a and Hm3a_P38 mutant on homomeric rASIC1a ($p = 0.029$, $F = 9.388$). Data are mean \pm SEM.

The mechanism of action of Hm3a on ASIC1

Given the sequence similarity of Hm3a and PcTx1, we hypothesized that Hm3a modulates ASIC1a in similar manner as PcTx1. Upon protonation, ASIC1 transitions from a resting state to an open state, then promptly enters a desensitized state in which the channel does not conduct current despite continued proton stimulus³⁹. The mechanism of action of PcTx1 on ASIC1a inhibition is well established. PcTx1 mimics the binding of protons in the acidic pocket of ASIC1a. In this context, PcTx1 acts as an agonist to stabilize the desensitization state of ASIC1a at physiological pH, resulting in channel inhibition^{32, 34}.

We assessed the effects of Hm3a on the SSD of rASIC1a by conditioning the channel with increasing proton concentrations in the presence and absence of 30 nM peptide (**Fig. 3.4A and 3.4B**). The current amplitude at different proton concentrations was fitted to the Hill function to obtain the pH of half-maximal desensitisation ($\text{pH}_{50 \text{ SSD}}$) (**Fig. 3.4C**). The $\text{pH}_{50 \text{ SSD}}$ of rASIC1a alone was 7.243 ± 0.003 (In good agreement with previous reports³⁴). The presence of 30 nM Hm3a during conditioning induced a parallel alkaline shift in the $\text{pH}_{50 \text{ SSD}}$ of rASIC1a by 0.362 pH units to 7.605 ± 0.024 (**Fig. 3.4C**). This parallel shift in SSD shows that when applied at conditioning pH 7.9, 30 nM Hm3a is insufficient to induce SSD of the channel (i.e. inhibition) thus channels are in the resting state but in the presence of peptide. This allows us to study the effect of the peptide on the pH-dependence of channel activation.

We next assessed the effects of Hm3a on pH-dependent activation of ASIC1a. A conditioning pH of 7.9 was used throughout these experiments to ensure that Hm3a did not inhibit channels as previously shown in the SSD experiment. In good agreement with a previous study on PcTx1³⁴, the pH_{50} of activation ($\text{pH}_{50 \text{ ACT}}$) of rASIC1a was 6.078 ± 0.039 as compared to 6.284 ± 0.064 when 30 nM Hm3a was used. Thus Hm3a lowered the proton concentrations required for activation by 0.206 pH units. This also highlights that Hm3a can interact with the channel and the channel can still be activated with peptide bound at pH 7.9.

The on- and off-rate of Hm3a on rASIC1a was examined by application of 30 nM peptide at pH 7.45 for increasing periods of time followed by activation at pH 6 (**Fig. 3.4D**). Fitting a single exponential function to the time course of inhibition data revealed a time to 50% inhibition ($t_{1/2}$) of ~16 s, with maximal inhibition reached after ~90 s (**Fig. 3.4D**). The slow onset of Hm3a inhibition may not be reflective of the actual binding on-rate for the peptide-channel interaction. Hm3a causes inhibition via inducing SSD of ASIC1a; however, the slow transition time required for conformational changes between the open state and desensitised may take longer than the actual on rate of the Hm3a. In agreement with this, we observed that application of 30 nM Hm3a for less than 10 s, led to potentiation of currents indicating the quick interaction between ASIC1a and Hm3a, similar to previously reported observations with PcTx1 on ASIC1a⁴⁰. The on-rate of Hm3a was similar to PcTx1 as previously reported using oocyte electrophysiology. Full inhibition of ASIC1a induced by 30 nM PcTx1 was achieved ~150 s after peptide application, with a time constant (τ) of 52 s ³⁴. Comparatively, on rate is slower with lower concentration of

PcTx1. With 1 nM PcTx1, maximum inhibition of ASIC1a expressed in COS-7 cells was achieved only after ~ 3 min³³, indicating that the on rate of Hm3a is concentration-dependent. Recovery of ASIC1a current after inhibition induced by a 180 s exposure to 30 nM Hm3a for was slow, reaching maximum current amplitude after ~ 360 s of washout of peptide. Fitting a single exponential function to the data revealed a $t_{1/2}$ of ~ 132 s (**Fig. 3.4E**). ASIC1a recovers from the desensitised state over a time course of several seconds (time constant ~ 10 s)⁴¹, hence the slower recovery from Hm3a inhibition can be largely attributed to dissociation of the peptide from the channel rather than simply recovery from SSD.

PcTx1 (and by similarity, Hm3a) was shown to preferentially bind and stabilize the open state of ASIC1b, resulting in channel potentiation³⁴. In order to determine the mechanism of ASIC1b potentiation by Hm3a, we analyzed the decay time constants of inactivation from the ASIC1b data shown in **Fig. 3.4F**. Control ASIC1b currents elicited by a pH drop to 5.0 decayed with a time constant, τ of 1.17 ± 0.10 ms. In good agreement with the EC_{50} of Hm3a for rASIC1b potentiation (**Fig. 3.2B**), Hm3a caused a concentration-dependent increase in the time constant of inactivation with an EC_{50} of 53 ± 2.54 nM and plateaued at ~ 300 nM with a time constant of 2.18 ± 0.11 ms (**Fig. 3.4E**).

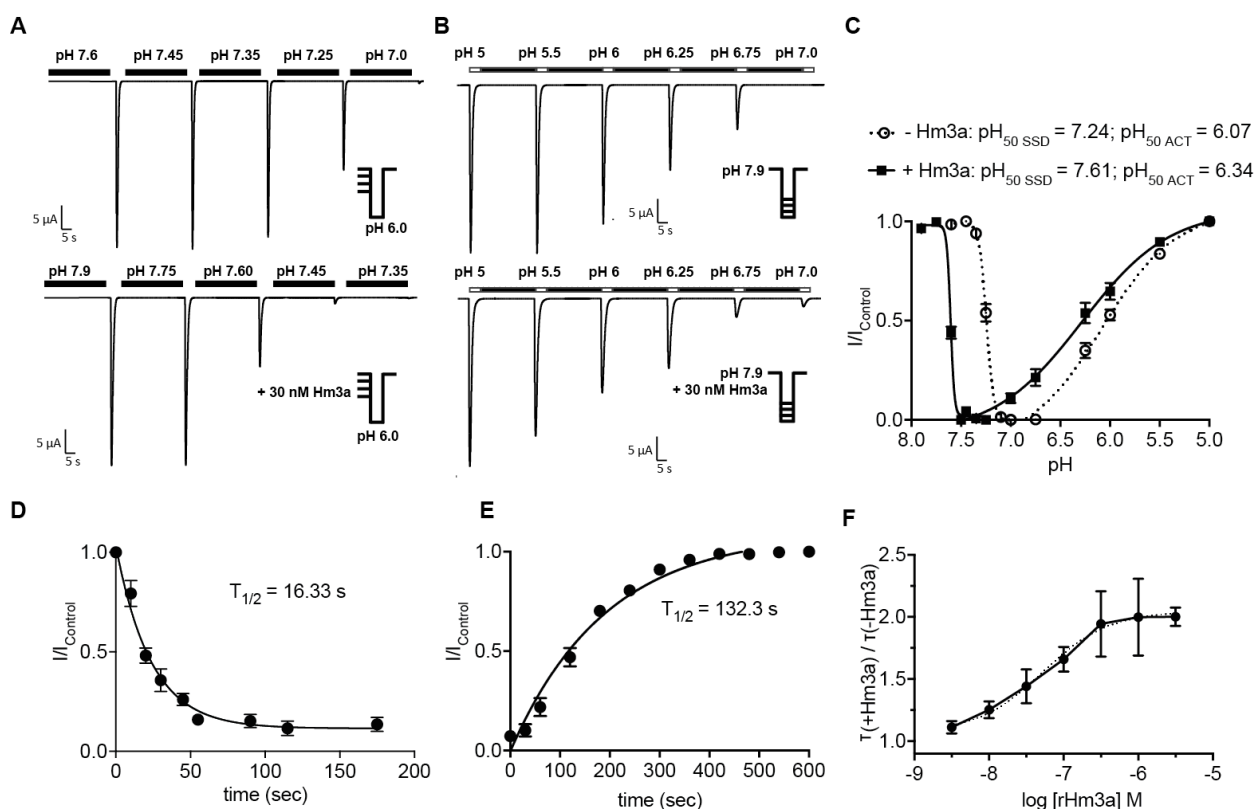


Figure 3.4. The mechanism of action of Hm3a on rASIC1. The effects of Hm3a on the pH-dependent steady-state desensitization, activation of ASIC1a and ASIC1b as well as the on-rates of Hm3a on ASIC1a were characterized by Mr Ben Cristofori-Armstrong. **(A)** Representative current traces in the absence (top) or presence (bottom) of 30 nM Hm3a, elicited by pH 6.0, following conditioning from pH 7.9 to 7.1. **(B)** Representative current traces in absence (top) or presence (bottom) of 30 nM Hm3a, elicited by pH 5.0 to 6.0, following conditioning at pH 7.9. **(C)** The alkaline shift in steady-state desensitisation ($p < 0.0001$, $F = 379.1$) and activation ($p = 0.029$, $F = 5.526$) of rASIC1a in the presence of 30 nM Hm3a (solid line, closed circle) as compared without Hm3a (dash line, open circles) ($n = 6$). **(D)** Time course of rASIC1a inhibition by 30 nM Hm3a. The time constant ($t_{1/2}$) for inhibition was calculated by fitting the data to a single-exponential decay function ($n = 6$). **(E)** Recovery from inhibition was assessed by applying 30 nM Hm3a for 180 s, then stimulating the channel after 0 s, 30 s, 60 s, and every 60 s thereafter until maximal recovery was reached. The time constant ($t_{1/2}$) for recovery from inhibition was calculated by fitting the data to a single-exponential function ($n = 6$). Data are mean \pm SEM. **(F)** The ratio of rASIC1b time constants of desensitization with varying concentrations of Hm3a against control conditions. Dashed line represents a fit of the Hill equation to the data and yielded an IC_{50} of 53 ± 0.4 nM ($n = 5$).

Characterizing the molecular interactions involved in subtype and species selectivity of Hm3a on ASIC1

The binding site of PcTx1 on ASIC1a has been extensively studied^{32, 35-36, 38} and comprises primarily α -helix5 at the bottom of the acidic pocket and palm of the adjacent

subunit. (**Fig. 3.5A**). The rASIC1a residue F350 (F352 in hASIC1a) on α -helix5 in the thumb domain is particularly important for interaction with the peptide⁴² making it diagnostic for this binding pocket. Given the similarity of Hm3a with PcTx1 in sequence and pharmacology we assume it will share the same binding site. However, in order to confirm this, the peptide was tested on the channel mutant rASIC1a_F350A. Hm3a did not inhibit rASIC1a_F350A, rather, at concentrations over 300 nM, Hm3a strongly potentiated currents (**Fig. 3.5B**). Previous studies using diluted *Psalmopoeus cambridgei* venom (containing PcTx1) on the rASIC1a_F350A or hASIC1a_F352L mutants showed a total lack of inhibition however, Sherwood 2009b⁴³ did show evidence that PcTx1 could still bind to the mutant channel (i.e. pre-incubation with 200 nM PcTx1 prevented the action of bigdynorphin). Our studies with higher concentrations of Hm3a (up to 3 mM) show that not only can it still bind but can have functional effects. This suggests that in the absence of the large number of contacts (~6) made between F350 and PcTx1 (and by similarity, Hm3a)³⁸ there are still sufficient residual contacts to mediate functional interaction.

ASIC1b is highly expressed in peripheral sensory nerves and has been shown to play a key role in mediating acid-induced nociception, at least in rodents^{25, 44}. Thus determining the molecular basis for Hm3a's potentiation of ASIC1b is an important step to understand potential complications when interpreting *in vivo* data, and enable the design of more selective ASIC1 modulators. Thus, we further characterized the potential interactions sites of Hm3a on ASIC1. ASIC1a and ASIC1b are splice isoforms that only differ in the first third of the protein (identical from residue 186 of rASIC1a onwards). A series of chimeras of rASIC1a and rASIC1b identified the small region of residues 167–185 of rASIC1a (19 residues N-terminal to the splice-site) to be sufficient to confer the inhibitory effect on rASIC1a in to rASIC1b³⁴. Interestingly, the only residue difference between human and rat ASIC1a within the known PcTx1 binding site, Ala178 in the rat channel (Val in human ASIC1a, and a proline in rASIC1b) also resides in this small region. We examined this region in further detail to determine specific residues involved by testing the effects of Hm3a on the rASIC1a mutants A178V, R175C, and E177G (**Fig. 3.5A**), as it was predicted these residues could be responsible for the different subtype and species pharmacology of Hm3a and PcTx1 at ASIC1.

The IC₅₀ of Hm3a was only slightly increased on rASIC1a_A178V (~ 4 nM) (**Fig. 3.5B**), which does not account for the 30-fold difference in IC₅₀ on rat and human ASIC1a, or the vastly different effects on rASIC1b, We concluded that Ala178 is not strongly involved in

channel–peptide interaction, consistent with MD predictions whereby the equivalent residue on cASIC1a, Gln179, does not form persistent interaction with Lys25 of PcTx1³⁸. In contrast, there was a profound decrease in Hm3a activity on both rASIC1a_R175C and rASIC1a_E177G, with IC₅₀s of 72.5 nM and 117 nM, respectively (**Fig. 3.5B**). These mutations were made to make the rASIC1a-binding interface resemble that of rASIC1b. None of these mutations affected the channels sensitivity to protons (in the form of SSD and activation) (**Supp. Fig. 3.1**), thus, any loss in potency is likely due to a loss of important interactions between the peptide and channel, rather than changes in channel function. Consistent with this evidence, PcTx1:ASIC1a crystal structures and molecular dynamic studies^{35-36, 38} showed that Glu177 and Arg175 of rASIC1a (Glu178 and Arg176 in cASIC1a) make contact with Trp24 and Arg27 of PcTx1, respectively, both major pharmacophore residues^{32, 38}. Although the interaction between PcTx1 and ASIC1a is well characterized, no study has so far demonstrated individual residues that determine subtype specificity between rASIC1a and rASIC1b. Here we show that Hm3a interacts with both ASIC1a and 1b with ~35-fold difference in potency (but different functional outcomes) and identified Arg175 and Glu177 of rASIC1a as two of the causative residues which can account for the subtype specificity of Hm3a, and most likely PcTx1. This improved understanding of the binding interaction between peptide and channel should the design of more specific analogues of these peptides.

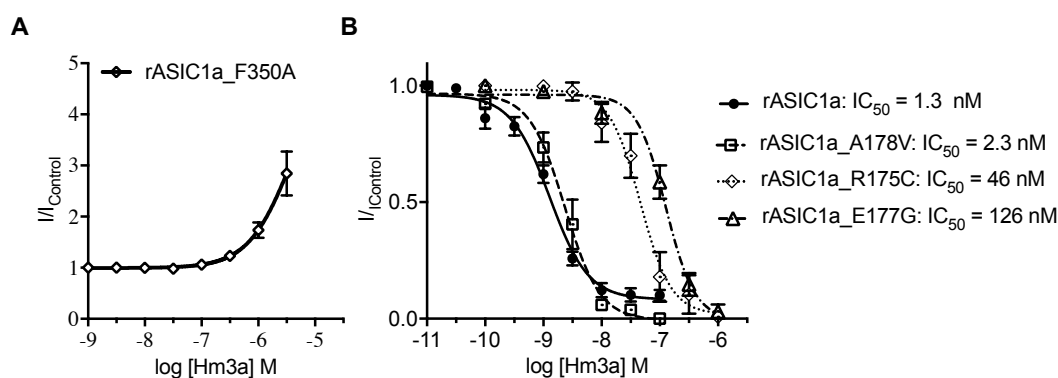
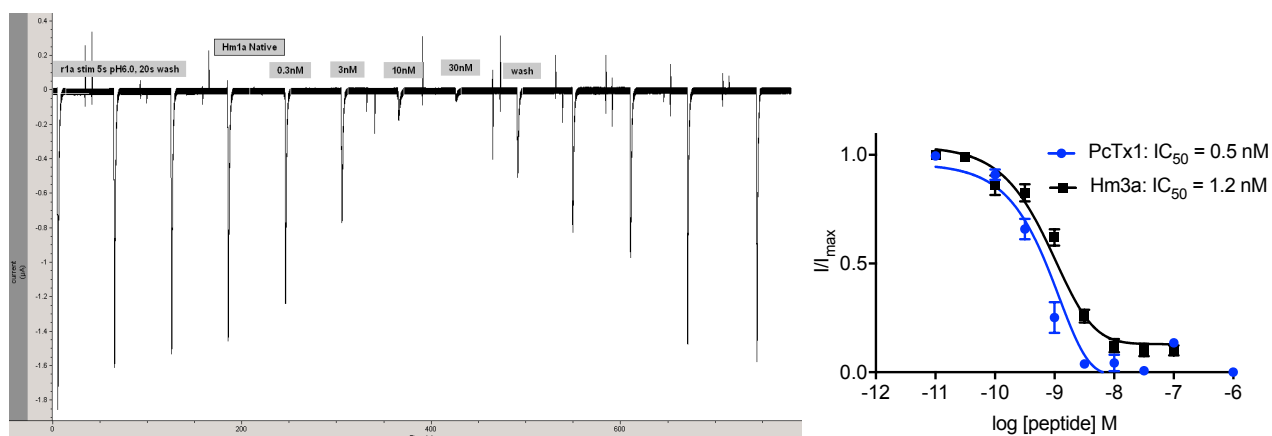
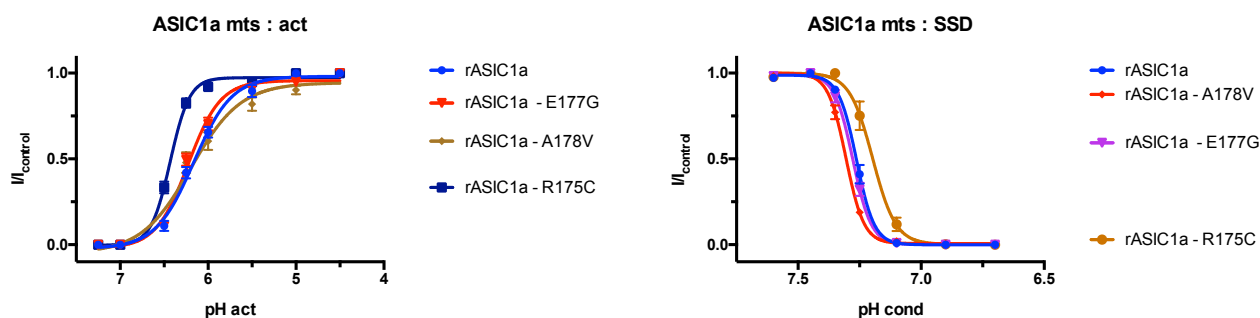


Figure 3.5. Molecular interactions involved in species and subtype selectivity. Concentration-response curves of Hm3a on (A) rASIC1a_F350; (B) rASIC1a_E177G, rASIC1a_R175C, rASIC1a_A178V and wild-type rASIC1a. Data are mean + SEM, n = 4–6, **** $p < 0.0001$.



Supplementary figure 3.1. (Left) Current trace of rat ASIC1a stimulated with pH 6.0. Several control pH exposures were included due to the tachyphylaxis effect of protons on ASIC1a. Data were normalised to the peak current (I_{\max}) after several exposures. (Right) Dose-response curves of PcTx1 (in blue) and Hm3a (in black) on rat ASIC1a tested at pH 7.45.



Supplementary figure 3.2. The Act (Left) and SSD (Right) curves for channel mutants. ($n = 6-7$). Experiments were carried out by Mr Ben Cristofori-Armstrong.

Stability of Hm3a and PcTx1

Given the likely role of ASIC1a in a range of pathological conditions, and the need to use selective pharmacological tools for target validation *in vivo*, it is important to understand the thermal and biological stability of peptides such as Hm3a and PcTx1. Despite its extensive use a research tool *in vivo*, the stability of PcTx1 has never been reported. Therefore, we evaluated the stability of Hm3a and PcTx1 in comparison to the clinically used peptide oxytocin at 55°C (in aqueous buffer at pH 7.4), in human serum and in human cerebrospinal fluid (CSF) (**Fig. 3.6A, 3.6B, and 3.6C**). Hm3a proved to have high thermal stability with <10% loss after 48 h at 55°C. In contrast, both PcTx1 and oxytocin showed a near-linear breakdown over time, with ~44% of PcTx1 and ~50% of oxytocin remaining at 48 h. Similarly, Hm3a was largely unaffected in human serum with >90% intact peptide after 48 h. In comparison, there was an initial sharp decline in PcTx1

during the first few hours which then plateaued at ~76% over 48 h. An initial sharp decline was also observed for oxytocin, however, unlike PcTx1, degradation of oxytocin continued over time, with ~50% peptide remaining after 48 h. Hm3a and PcTx1 appear to be highly stable in human CSF with >90% intact after 48 h. Oxytocin was also relatively stable in hCSF (~81% intact at 48 h) while human atrial natriuretic peptide was completely degraded by 12 h under these conditions.

It is often claimed that peptides containing the ICK motif are highly stable and resistant to thermal, chemical and enzymatic degradation and this has been as demonstrated for several spider venom ICK peptides such as ω -Hv1a, ProTx-I, ProTx-II, GsMTx-4, and GTx1-15⁴⁵⁻⁴⁶. Interestingly, despite the high degree of sequence similarity, Hm3a was more stable than PcTx1 when challenged with high temperature or human serum. The improved stability of Hm3a over PcTx1 may be due to Hm3a's fewer charged residues (particularly lysines at the C-terminus), which are involved in the cleavage sites of many enzymes such as trypsin⁴⁷. We conclude that the substantially higher biological stability of Hm3a as compared to PcTx1 makes it a more attractive tool for studying the role of ASICs in biological fluids and in *in vivo* studies.

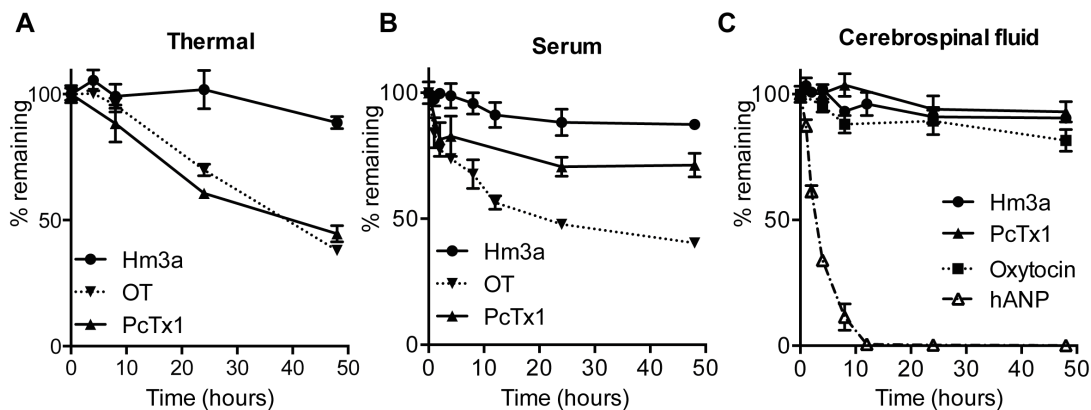
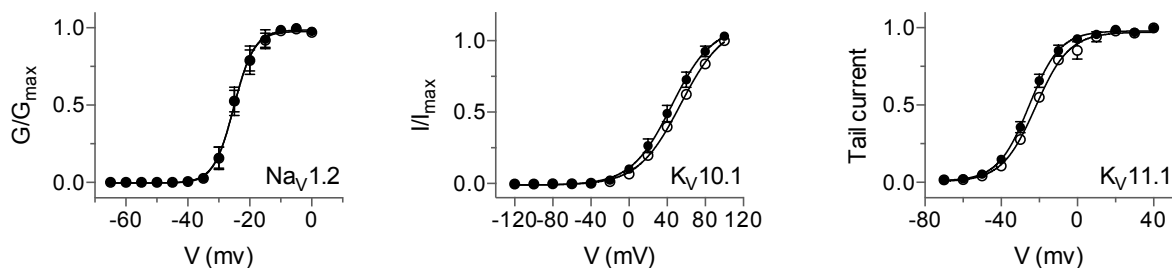


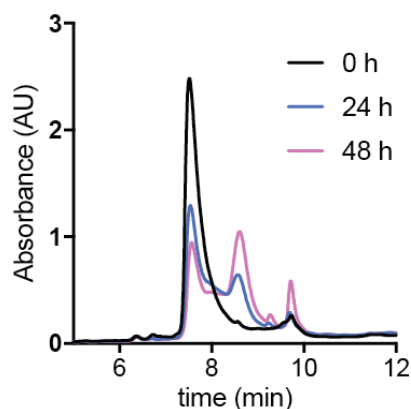
Figure 3.6. Comparative stability studies of Hm3a and PcTx1. **(A)** Thermal stability of Hm3a, PcTx1 and oxytocin at 55 °C (pH 7.4). **(B)** Serum stability of Hm3a, PcTx1 and oxytocin at 37 °C. **(C)** Cerebrospinal fluid stability of Hm3a, PcTx1, oxytocin and human atrial natriuretic peptide (hANP) at 37 °C (CSF stability of Hm3a and hANP were carried out by Mr Ben Cristofori-Armstrong). The percentage of peptide remaining for all conditions was quantified using RP-HPLC. Data are mean \pm SEM.

Spider venom peptides are known to be gating modifiers of voltage-gated ion channels, hence Hm3a was also tested on therapeutically-relevant off-targets including the voltage-gated sodium channel subtype 1.2 ($Na_v1.2$) and the voltage-gated potassium channel subtypes 10.1 ($K_v10.1$) and 11.1 ($K_v11.1$). $Na_v1.2$ is predominantly expressed in the

central nervous system; prolonged opening of the channel were implicated with onset of epileptic disorders⁴⁸. $K_V10.1$ is implicated in a variety of cellular processes including cell proliferation and tumour progression⁴⁹ whereas $K_V11.1$ is vital for proper cardiac functioning⁴⁹. At 10 μ M, Hm3a had no effect on the voltage-dependence activation of these channels (**Supp. Fig. 3.2**), further iterating the high selectivity of Hm3a towards ASIC1.



Supplementary figure 3.3: The effect of 10 mM Hm3a on the voltage dependence of activation of several human voltage gated ion channels off-targets, (from left to right) $Na_V1.2$, $K_V10.1$ and $K_V11.1$. Experiments were performed by Mr Ben Cristofori-Armstrong.



Supplementary figure 3.4: HPLC profile of PcTx1 following incubation in human serum at 0 h (black), 24 h (blue) and 48 h (pink).

Conclusion. We have identified and characterized a new potent peptide modulator of ASIC1 from the venom of *H. maculata*, and suspect that spider venoms harbour more, potent and selective peptide inhibitors of ASICs. Despite the high sequence and pharmacological similarity of Hm3a and PcTx1, Hm3a appears to be superior in terms of stability. Furthermore, through rational engineering of Hm3a, we produced a more potent variant of the peptide making its ASIC1a inhibitory potency on par with PcTx1. We also identified several determinant residues in rASIC1a for ASIC1a/1b selectivity studies. The

distinct differences between the subtypes and species selectivity will contribute to the rational engineering and development of ASIC modulators with improved subtype selectivity. Overall, the discovery of new ASIC1 modulators will improve our knowledge of ASIC function and facilitate the development of novel ASIC-targeting therapeutic leads and research tools.

METHODS

Venom Peptide Purification and Characterization

Heteroscodra maculata venom was purchased from Spider Pharm (Yarnell, AZ, USA). The lyophilized venom was dissolved in water (1:10 dilution from original venom volume) and stored at -20°C until required. A total of 50 μL of the diluted venom was fractionated using RP-HPLC on a C18 column (Phenomenex Kinetex, 250 x 4.6 mm, 100 Å) using a gradient of solvent A (0.05% trifluoroacetic acid (TFA) in H_2O) and solvent B (90% acetonitrile, 0.043% TFA in H_2O) as follows: 5% solvent B for 5 min, 5–20% solvent B for 10 min, 20–50% solvent B for 30 min, 50–80% solvent for 5 min, at a flow rate of 1 mL/min. Fractions were collected by monitoring eluent absorption at 214 and 280 nm and lyophilized. The dried fractions were dissolved in water and aliquots of each fraction were assayed for activity against rASIC1a expressed in *Xenopus* oocytes. A second RP-HPLC purification was carried out on the active fraction using a C18 column (Thermo Aquasil, 50 x 2.1 mm, 190 Å) and a gradient of 10–30% solvent B over 20 min at a flow rate of 0.3 ml/min. All solvents used were HPLC grade.

RP-HPLC and MALDI-TOF Mass Spectrometry.

Both analytical and semi-preparative RP-HPLC was performed using a Shimadzu Prominence HPLC system with the column at room temperature ($\sim 21\text{--}22^{\circ}\text{C}$). Peptide mass was determined using matrix-assisted laser desorption/ionisation time-of-flight (MALDI-TOF) MS using a Model 4700 Proteomics Analyzer (Applied Biosystems, Foster City, CA, USA) collected in both positive reflector and linear mode. All masses reported are $\text{M}+\text{H}^+$. Fractions were mixed (1:1, v/v) with α -cyano-4-hydroxycinnamic acid matrix (7 mg/mL in 50% acetonitrile in H_2O). To obtain a sequence tag of the peptide the reductive

matrix 1,5-diaminonaphthalene (1,5-DAN) was used⁵⁰. The active fractions were mixed (1:1, v/v) with 1,5-DAN (10 mg/ml in 50% acetonitrile, 0.1% formic acid in H₂O).

Peptide Sequencing

The pure peptide was reduced with 2-mercaptoethanol and alkylated by 4-vinyl-pyridine then sequenced via N-terminal Edman degradation (477A, Applied Biosystems, Foster City, CA, USA). Sequence homologies were determined using sequences obtained from a search of non-redundant protein databases via the BLAST server and Arachnoserver (www.arachnoserver.org/)³⁰. Sequence alignments and percentages of similarity were calculated using BLASTP⁵¹.

Production of Recombinant Hm3a

Recombinant Hm3a was produced using the bacterial periplasmic expression system as described for PcTx1³¹⁻³². The synthetic gene encoding PcTx1 was cloned into the pLicC-MBP expression vector, then mutated using standard PCR protocols⁵² to produce a vector encoding Hm3a. The fusion protein was expressed in *E. coli* BL21 (λ DE3) and grown in Luria-Bertani broth medium to an OD₆₀₀ of 0.8–1.0. The culture was then cooled to 16°C and induced with 0.5 mM IPTG for 16 hours. Cells were pelleted by centrifugation at 5000 *g* then lysed via mechanical lysis at 28 kPa. The fusion protein was purified from the cell lysate via affinity chromatography using Ni-NTA Superflow resin (QIAGEN, Valencia, CA, USA). The peptide was cleaved from the fusion protein using TEV protease and purified by RP-HPLC on a C4 semi-preparative column (Phenomenex Jupiter, 250 x 10 mm, 300 Å). Peptide purity was verified using analytical RP-HPLC on a C18 column (Thermo Aquasil, 50 x 2.1 mm, 190 Å) and gradient of 10–50 % solvent B over 40 min, at a flow rate of 0.25 ml/min. Masses of the eluted peptides were obtained using MALDI-TOF MS.

Electrophysiology

Peptide activity was assessed using TEVC electrophysiology on *Xenopus laevis* oocytes. Oocytes preparation, cDNA/cRNA preparation and injections were performed as described^{4, 32}. Stage V–VI oocyte were injected with 20–40 ng of ion channel cDNA/cRNA (Nanoject 2000; WPI, Sarasota, FL, USA). Currents were recorded 1–6 days after injection

under voltage-clamp using two standard glass microelectrodes of 0.5–2 M Ω resistance when filled with 3 M KCl solution. Oocytes were clamped at –60 mV (OC-725C oocyte clamp; Warner Instruments, Hamden, CT, USA). Currents were elicited by a drop in pH from 7.45 to 6.0 or 5.0 using a gravity–driven microperfusion system (consisting of 60 mL syringe connected to an IV flow regulator) to allow controlled to allow rapid solution exchange (~1.5 ml/min) at room temperature. HEPES was replaced by MES in buffers with pH below 6.8. A series of control currents were taken to account for the tachyphylaxis effect of ASICs in response to repeated pH stimulation prior to peptide application. Data was acquired (2000 Hz and filtered at 0.01 Hz) and analysis was performed using pCLAMP software Version 10 (Axon Instruments, Sunnyvale, CA, USA). Peptides were prepared by serial dilutions in ND96 (96 mM NaCl, 1.8 mM CaCl₂, 2 mM KCl, 2 mM MgCl₂, 5 mM HEPES) solution supplemented with 0.1 % bovine serum albumin (BSA, fatty acid free) to minimize adsorption to plastic surfaces.

Stability Assays

Thermal stability was assessed by dissolving Hm3a, PcTx1 or oxytocin in 10 mM phosphate buffer pH 7.4 to a final concentration of 25 mM. Samples were incubated at 55 °C and triplicate samples were taken at $t = 0, 2, 4, 8, 24, 48,$ and 72 h, quenched with 5% TFA solution, centrifuged at 17 000 g for 25 minutes and analyzed using RP-HPLC. The peak corresponding to intact peptide was identified by comparison to an untreated sample and mass determination via MALDI-TOF MS. Levels of peptide were quantified by integration of the peak area recorded at 214 nm, and plotted as a percentage of the peak area at $t = 0$ for each respective sample.

Serum stability was performed using male AB human serum (Sigman-Aldrich) and cerebrospinal fluid (CSF) stability using pooled human CSF collected from healthy volunteers (acquired from The Macquaire Motor Neurone Disease Research Centre, Macquarie University, NSW, 2109, Australia). Both serum and CSF were pre-warmed to 37 °C for 15 minutes and added to lyophilized Hm3a, PcTx1, human atrial natriuretic peptide, or oxytocin to a final concentration of 50 mM. Triplicate samples were taken at $t = 0, 1, 2, 4, 8, 12, 24,$ and 48 h, quenched with 20% TFA solution, and stored at 4 °C for 15 minutes to precipitate serum or CSF proteins. Samples were centrifuged at 17 000 g for 25 minutes and analyzed using RP-HPLC. The peak corresponding to intact peptide was

identified by comparison to an untreated sample and mass determination via MALDI-TOF MS. Levels of peptide were quantified as described above.

Deposition of Protein and cDNA Sequence Information.

Peptide sequence information derived for Hm3a has been submitted to the publicly accessible ArachnoServer spider-toxin database³⁰. The ArachnoServer accession numbers for Hm3a is AS002366. Toxin records can be accessed directly using the final four digits of the accession number.

Materials

Chemicals were purchased from Sigma Aldrich (St. Louis, MO, USA, via Sigma Australia, Castle Hill, NSW, Australia), with the exceptions of IPTG (Bioline, Alexandria, NSW, Australia) and TFA (Auspep Tullamarine, VIC, Australia). Recombinant TEV protease was produced in-house using a previously described protocol⁵³.

Animal Welfare and Ethics Statement.

Oocyte studies complied with the Australian code of practice for care and use of animals for scientific purposes, 8th Ed. 2013. The protocol was approved by The University of Queensland Animal Ethics Committee (Approval No. QBI/059/13/ARC/NHMRC). *Xenopus laevis* oocytes were obtained via recovery surgery performed under tricaine methanesulfonate anaesthesia (animals bathed in 1.3 mg/ml). The minimum time between surgeries on the same animal was 3 months. All studies involving animals are reported in accordance with the ARRIVE guidelines for reporting experiments involving animals⁵⁴⁻⁵⁵.

Data Analysis and Statistical Procedures

Data were normalized to a series of control current (I/I_{control}) elicited by a drop in pH (6.0–5.0) with only sample buffer and analyzed with the software Graphpad Prism 7 (La Jolla, CA, USA). The half-maximal response (IC_{50} , EC_{50} or pH_{50}) and Hill coefficient (nH) was obtained through a non-linear fit to the data of a four parameter logistic equation

("sigmoidal dose-response"). Half-life ($t_{1/2}$) was obtained through a non-linear fit to the data of a "dissociation – one phase exponential decay" equation. Results are reported, in the text or on the figures, as means \pm SEM. They represent the mean of n individual measurements on different oocytes. Statistical analysis and comparison between three or more groups were performed with one-way ANOVA and Tukey's Test whilst comparison between two groups was performed using Student's t-test.

ASSOCIATED CONTENT

Supporting Information

Steady-state desensitization curves of rASIC1a chimeras

Dose-response curves of Hm3a on off targets, human Nav1.2, Kv10.1 and Kv11.1

AUTHOR INFORMATION

Corresponding Author

*Email: l.rash@uq.edu.au

Author Contributions

#These authors contributed equally to this work.

Notes

The authors declare no competing financial interest.

ACKNOWLEDGMENTS

We thank Dr. Jennifer Smith for helping with stability assays and Prof. Gilles Guillemin for providing pooled human cerebrospinal fluid. We thank Prof. John Wood for the rat ASIC1a, ASIC2a, and ASIC3 clones; Prof. Stefan Gründer for the rat ASIC1b clone; A/Prof Candice Askwith for the human ASIC1b clone; Prof. Richard Lewis for the rat Nav1.2 clone; Dr Cas Simons for the Kv10.1 clone; and Prof. Jamie Vandenberg for the Kv11.1 clone. We acknowledge financial support from the Australian National Health and Medical Research Council (NHMRC Grant 15507; L.D.R.); S.Y.E. is supported by a UQ International Scholarship.

REFERENCES

1. Ackerman, M. J.; Clapham, D. E., Ion channels--basic science and clinical disease. *N Engl J Med* 1997, *336* (22), 1575–1586.
2. Lewis, R. J.; Garcia, M. L., Therapeutic potential of venom peptides. *Nat Rev Drug Discov* 2003, *2* (10), 790–802.
3. Klint, J. K.; Senff, S.; Rupasinghe, D. B.; Er, S. Y.; Herzig, V.; Nicholson, G. M.; King, G. F., Spider-venom peptides that target voltage-gated sodium channels: pharmacological tools and potential therapeutic leads. *Toxicon* 2012, *60* (4), 478–491.
4. Saez, N. J.; Senff, S.; Jensen, J. E.; Er, S. Y.; Herzig, V.; Rash, L. D.; King, G. F., Spider-venom peptides as therapeutics. *Toxins* 2010, *2* (12), 2851–2871.
5. Nebe, J.; Ebersberger, A.; Vanegas, H.; Schaible, H. G., Effects of omega-agatoxin IVA, a P-type calcium channel antagonist, on the development of spinal neuronal hyperexcitability caused by knee inflammation in rats. *J Neurophysiol* 1999, *81* (6), 2620–2626.
6. Osteen, J. D.; Herzig, V.; Gilchrist, J.; Emrick, J. J.; Zhang, C.; Wang, X.; Castro, J.; Garcia-Caraballo, S.; Grundy, L.; Rychkov, G. Y.; Weyer, A. D.; Dekan, Z.; Undheim, E. A.; Alewood, P.; Stucky, C. L.; Brierley, S. M.; Basbaum, A. I.; Bosmans, F.; King, G. F.; Julius, D., Selective spider toxins reveal a role for the Nav1.1 channel in mechanical pain. *Nature* 2016, *534* (7608), 494–499.
7. Siemens, J.; Zhou, S.; Piskorowski, R.; Nikai, T.; Lumpkin, E. A.; Basbaum, A. I.; King, D.; Julius, D., Spider toxins activate the capsaicin receptor to produce inflammatory pain. *Nature* 2006, *444* (7116), 208–212.
8. Kellenberger, S.; Schild, L., Epithelial sodium channel/degenerin family of ion channels: a variety of functions for a shared structure. *Physiol Rev* 2002, *82* (3), 735–767.
9. Waldmann, R.; Champigny, G.; Bassilana, F.; Heurteaux, C.; Lazdunski, M., A proton-gated cation channel involved in acid-sensing. *Nature* 1997, *386* (6621), 173–177.
10. Hesselager, M.; Timmermann, D. B.; Ahring, P. K., pH Dependency and desensitization kinetics of heterologously expressed combinations of acid-sensing ion channel subunits. *J Biol Chem* 2004, *279* (12), 11006–11015.
11. Chu, X. P.; Xiong, Z. G., Acid-sensing ion channels in pathological conditions. *Adv Exp Med Biol* 2013, *961*, 419–431.
12. Yermolaieva, O.; Leonard, A. S.; Schnizler, M. K.; Abboud, F. M.; Welsh, M. J., Extracellular acidosis increases neuronal cell calcium by activating acid-sensing ion channel 1a. *Proc Natl Acad Sci U S A* 2004, *101* (17), 6752–6757.
13. Bohlen, C. J.; Chesler, A. T.; Sharif-Naeini, R.; Medzihradzsky, K. F.; Zhou, S.; King, D.; Sanchez, E. E.; Burlingame, A. L.; Basbaum, A. I.; Julius, D., A heteromeric Texas coral snake toxin targets acid-sensing ion channels to produce pain. *Nature* 2011, *479* (7373), 410–414.
14. Deval, E.; Noel, J.; Lay, N.; Alloui, A.; Diochot, S.; Friend, V.; Jodar, M.; Lazdunski, M.; Lingueglia, E., ASIC3, a sensor of acidic and primary inflammatory pain. *EMBO J* 2008, *27* (22), 3047–3055.

15. Duan, B.; Wu, L. J.; Yu, Y. Q.; Ding, Y.; Jing, L.; Xu, L.; Chen, J.; Xu, T. L., Upregulation of acid-sensing ion channel ASIC1a in spinal dorsal horn neurons contributes to inflammatory pain hypersensitivity. *J Neurosci* 2007, 27 (41), 11139–11148.
16. Coryell, M. W.; Wunsch, A. M.; Haenfler, J. M.; Allen, J. E.; Schnizler, M.; Ziemann, A. E.; Cook, M. N.; Dunning, J. P.; Price, M. P.; Rainier, J. D.; Liu, Z.; Light, A. R.; Langbehn, D. R.; Wemmie, J. A., Acid-sensing ion channel-1a in the amygdala, a novel therapeutic target in depression-related behavior. *J Neurosci* 2009, 29 (17), 5381–5388.
17. Vergo, S.; Craner, M. J.; Etzensperger, R.; Attfeld, K.; Friese, M. A.; Newcombe, J.; Esiri, M.; Fugger, L., Acid-sensing ion channel 1 is involved in both axonal injury and demyelination in multiple sclerosis and its animal model. *Brain* 2011, 134 (Pt 2), 571–584.
18. Ziemann, A. E.; Schnizler, M. K.; Albert, G. W.; Severson, M. A.; Howard, M. A., 3rd; Welsh, M. J.; Wemmie, J. A., Seizure termination by acidosis depends on ASIC1a. *Nat Neurosci* 2008, 11 (7), 816–822.
19. Xiong, Z. G.; Zhu, X. M.; Chu, X. P.; Minami, M.; Hey, J.; Wei, W. L.; MacDonald, J. F.; Wemmie, J. A.; Price, M. P.; Welsh, M. J.; Simon, R. P., Neuroprotection in ischemia: blocking calcium-permeable acid-sensing ion channels. *Cell* 2004, 118 (6), 687–698.
20. Wemmie, J. A.; Taugher, R. J.; Kreple, C. J., Acid-sensing ion channels in pain and disease. *Nat Rev Neurosci* 2013, 14 (7), 461–471.
21. Baron, A.; Lingueglia, E., Pharmacology of acid-sensing ion channels - Physiological and therapeutical perspectives. *Neuropharmacology* 2015, 94, 19–35.
22. Escoubas, P.; De Weille, J. R.; Lecoq, A.; Diochot, S.; Waldmann, R.; Champigny, G.; Moinier, D.; Menez, A.; Lazdunski, M., Isolation of a tarantula toxin specific for a class of proton-gated Na⁺ channels. *J Biol Chem* 2000, 275 (33), 25116–25121.
23. Joeres, N.; Augustinowski, K.; Neuhof, A.; Assmann, M.; Grunder, S., Functional and pharmacological characterization of two different ASIC1a/2a heteromers reveals their sensitivity to the spider toxin PcTx1. *Sci Rep* 2016, 6, 27647.
24. Sherwood, T. W.; Lee, K. G.; Gormley, M. G.; Askwith, C. C., Heteromeric acid-sensing ion channels (ASICs) composed of ASIC2b and ASIC1a display novel channel properties and contribute to acidosis-induced neuronal death. *J Neurosci* 2011, 31 (26), 9723–9734.
25. Diochot, S.; Baron, A.; Salinas, M.; Douguet, D.; Scarzello, S.; Dabert-Gay, A. S.; Debayle, D.; Friend, V.; Alloui, A.; Lazdunski, M.; Lingueglia, E., Black mamba venom peptides target acid-sensing ion channels to abolish pain. *Nature* 2012, 490 (7421), 552–555.
26. Kuduk, S. D.; Chang, R. K.; Wai, J. M.; Di Marco, C. N.; Cofre, V.; DiPardo, R. M.; Cook, S. P.; Cato, M. J.; Jovanovska, A.; Urban, M. O.; Leitl, M.; Spencer, R. H.; Kane, S. A.; Hartman, G. D.; Bilodeau, M. T., Amidine derived inhibitors of acid-sensing ion channel-3 (ASIC3). *Bioorg Med Chem Lett* 2009, 19 (15), 4059–4063.
27. Kuduk, S. D.; Di Marco, C. N.; Bodmer-Narkevitch, V.; Cook, S. P.; Cato, M. J.; Jovanovska, A.; Urban, M. O.; Leitl, M.; Sain, N.; Liang, A.; Spencer, R. H.; Kane, S. A.; Hartman, G. D.; Bilodeau, M. T., Synthesis,

- structure-activity relationship, and pharmacological profile of analogs of the ASIC-3 inhibitor A-317567. *ACS Chem Neurosci* 2010, 1 (1), 19–24.
28. Kuduk, S. D.; Di Marco, C. N.; Chang, R. K.; Dipardo, R. M.; Cook, S. P.; Cato, M. J.; Jovanovska, A.; Urban, M. O.; Leidl, M.; Spencer, R. H.; Kane, S. A.; Bilodeau, M. T.; Hartman, G. D.; Bock, M. G., Amiloride derived inhibitors of acid-sensing ion channel-3 (ASIC3). *Bioorg Med Chem Lett* 2009, 19 (9), 2514–2518.
29. King, G. F.; Gentz, M. C.; Escoubas, P.; Nicholson, G. M., A rational nomenclature for naming peptide toxins from spiders and other venomous animals. *Toxicon* 2008, 52 (2), 264–276.
30. Herzig, V.; Wood, D. L.; Newell, F.; Chaumeil, P. A.; Kaas, Q.; Binford, G. J.; Nicholson, G. M.; Gorse, D.; King, G. F., ArachnoServer 2.0, an updated online resource for spider toxin sequences and structures. *Nucleic Acids Res* 2011, 39 (Database issue), D653–D657.
31. Klint, J. K.; Senff, S.; Saez, N. J.; Seshadri, R.; Lau, H. Y.; Bende, N. S.; Undheim, E. A.; Rash, L. D.; Mobli, M.; King, G. F., Production of recombinant disulfide-rich venom peptides for structural and functional analysis via expression in the periplasm of *E. coli*. *PLoS One* 2013, 8 (5), e63865.
32. Saez, N. J.; Mobli, M.; Bieri, M.; Chassagnon, I. R.; Malde, A. K.; Gamsjaeger, R.; Mark, A. E.; Gooley, P. R.; Rash, L. D.; King, G. F., A dynamic pharmacophore drives the interaction between Psalmotoxin-1 and the putative drug target acid-sensing ion channel 1a. *Mol Pharmacol* 2011, 80 (5), 796–808.
33. Salinas, M.; Rash, L. D.; Baron, A.; Lambeau, G.; Escoubas, P.; Lazdunski, M., The receptor site of the spider toxin PcTx1 on the proton-gated cation channel ASIC1a. *J Physiol* 2006, 570 (Pt 2), 339–354.
34. Chen, X.; Kalbacher, H.; Grunder, S., Interaction of acid-sensing ion channel (ASIC) 1 with the tarantula toxin psalmotoxin 1 is state dependent. *J Gen Physiol* 2006, 127 (3), 267–276.
35. Bacongus, I.; Gouaux, E., Structural plasticity and dynamic selectivity of acid-sensing ion channel-spider toxin complexes. *Nature* 2012, 489 (7416), 400–405.
36. Dawson, R. J.; Benz, J.; Stohler, P.; Tetaz, T.; Joseph, C.; Huber, S.; Schmid, G.; Hugin, D.; Pflimlin, P.; Trube, G.; Rudolph, M. G.; Hennig, M.; Ruf, A., Structure of the acid-sensing ion channel 1 in complex with the gating modifier Psalmotoxin 1. *Nat Commun* 2012, 3, 936.
37. Wu, L. J.; Duan, B.; Mei, Y. D.; Gao, J.; Chen, J. G.; Zhuo, M.; Xu, L.; Wu, M.; Xu, T. L., Characterization of acid-sensing ion channels in dorsal horn neurons of rat spinal cord. *J Biol Chem* 2004, 279 (42), 43716–43724.
38. Saez, N. J.; Deplazes, E.; Cristofori-Armstrong, B.; Chassagnon, I. R.; Lin, X.; Mobli, M.; Mark, A. E.; Rash, L. D.; King, G. F., Molecular dynamics and functional studies define a hot spot of crystal contacts essential for PcTx1 inhibition of acid-sensing ion channel 1a. *Br J Pharmacol* 2015, 172 (20), 4985–4995.
39. Gründer, S.; Pusch, M., Biophysical properties of acid-sensing ion channels (ASICs). *Neuropharmacology* 2015, 94, 9–18.
40. Chen, X.; Kalbacher, H.; Grunder, S., The tarantula toxin psalmotoxin 1 inhibits acid-sensing ion channel (ASIC) 1a by increasing its apparent H⁺ affinity. *J Gen Physiol* 2005, 126 (1), 71–79.

41. Babini, E.; Paukert, M.; Geisler, H. S.; Grunder, S., Alternative splicing and interaction with di- and polyvalent cations control the dynamic range of acid-sensing ion channel 1 (ASIC1). *J Biol Chem* 2002, 277 (44), 41597–41603.
42. Sherwood, T.; Franke, R.; Conneely, S.; Joyner, J.; Arumugan, P.; Askwith, C., Identification of protein domains that control proton and calcium sensitivity of ASIC1a. *J Biol Chem* 2009, 284 (41), 27899–27907.
43. Sherwood, T. W.; Askwith, C. C., Dynorphin opioid peptides enhance acid-sensing ion channel 1a activity and acidosis-induced neuronal death. *J Neurosci* 2009, 29 (45), 14371–14380.
44. Hoagland, E. N.; Sherwood, T. W.; Lee, K. G.; Walker, C. J.; Askwith, C. C., Identification of a calcium permeable human acid-sensing ion channel 1 transcript variant. *J Biol Chem* 2010, 285 (53), 41852–41862.
45. Herzig, V.; King, G. F., The Cystine Knot Is Responsible for the Exceptional Stability of the Insecticidal Spider Toxin omega-Hexatoxin-Hv1a. *Toxins (Basel)* 2015, 7 (10), 4366–4380.
46. Kikuchi, K.; Sugiura, M.; Kimura, T., High Proteolytic Resistance of Spider-Derived Inhibitor Cystine Knots. *Int J Pept* 2015, 2015, 537508.
47. Olsen, J. V.; Ong, S. E.; Mann, M., Trypsin cleaves exclusively C-terminal to arginine and lysine residues. *Mol Cell Proteomics* 2004, 3 (6), 608–614.
48. Sugawara, T.; Tsurubuchi, Y.; Agarwala, K. L.; Ito, M.; Fukuma, G.; Mazaki-Miyazaki, E.; Nagafuji, H.; Noda, M.; Imoto, K.; Wada, K.; Mitsudome, A.; Kaneko, S.; Montal, M.; Nagata, K.; Hirose, S.; Yamakawa, K., A missense mutation of the Na⁺ channel alpha II subunit gene Na(v)1.2 in a patient with febrile and afebrile seizures causes channel dysfunction. *Proc Natl Acad Sci U S A* 2001, 98 (11), 6384–6389.
49. Ouadid-Ahidouch, H.; Ahidouch, A.; Pardo, L. A., K_v10.1 K(+) channel: from physiology to cancer. *Pflugers Arch* 2016, 468 (5), 751–762.
50. Fukuyama, Y.; Iwamoto, S.; Tanaka, K., Rapid sequencing and disulfide mapping of peptides containing disulfide bonds by using 1,5-diaminonaphthalene as a reductive matrix. *J Mass Spectrom* 2006, 41 (2), 191–201.
51. Altschul, S. F.; Madden, T. L.; Schaffer, A. A.; Zhang, J.; Zhang, Z.; Miller, W.; Lipman, D. J., Gapped BLAST and PSI-BLAST: a new generation of protein database search programs. *Nucleic Acids Res* 1997, 25 (17), 3389–3402.
52. Qi, D.; Scholthof, K. B., A one-step PCR-based method for rapid and efficient site-directed fragment deletion, insertion, and substitution mutagenesis. *J Virol Methods* 2008, 149 (1), 85–90.
53. Fang, L.; Jia, K. Z.; Tang, Y. L.; Ma, D. Y.; Yu, M.; Hua, Z. C., An improved strategy for high-level production of TEV protease in *Escherichia coli* and its purification and characterization. *Protein Expr Purif* 2007, 51 (1), 102–109.
54. Kilkenny, C.; Browne, W.; Cuthill, I. C.; Emerson, M.; Altman, D. G.; National Centre for the Replacement, R.; Reduction of Animals in, R., Animal research: reporting in vivo experiments—the ARRIVE guidelines. *J Cereb Blood Flow Metab* 2011, 31 (4), 991–993.
55. McGrath, J. C.; Drummond, G. B.; McLachlan, E. M.; Kilkenny, C.; Wainwright, C. L., Guidelines for reporting experiments involving animals: the ARRIVE guidelines. *Br J Pharmacol* 2010, 160 (7), 1573–1576.

Chapter Four

Elucidating the pharmacokinetics and biodistribution of PcTx1 following intravenous and intranasal administration

4.1 Introduction

Until recently, toxinology research was mainly focused on negating the adverse effects of venoms (e.g., via the development of anti-venoms). However, deepened understanding of the molecular basis of channelopathies and neurological disorders had sparked an interest in the development of venom-derived ion channel ligands as therapeutics and diagnostics tools²²⁶⁻²²⁸. Spiders, in particular, are a rich source of ion channel modulators. Peptides from spider venom, fine-tuned over million of years of evolution, are able to target various ion channels with incredible potency and specificity. To our advantage, these highly potent venom peptides have proven to be useful pharmacological tools as well as leads for agrochemical¹⁰ and pharmaceutical²²⁹ applications. In particular, PcTx1, an ASIC1a modulator, is a valuable research tool and possible therapeutic lead molecule for several neurological diseases where gaining access to the CNS is crucial for its use in *in vivo* studies (as detailed in **Chapters 1 and 3**). However, achieving an effective dose of PcTx1 in the brain is challenging as the brain is enveloped by the blood-brain barrier.

The BBB is responsible for maintaining delicate homeostasis in the brain and it prevents the influx of unwanted molecules, which unfortunately includes most drugs and drug leads^{172, 230}. In general, only compounds with a molecular weight less than 400–600 Da, a polar surface <70 Å² and an octanol-to-water partition coefficient close to 3.4 have the potential to cross the BBB by passive diffusion²³¹. As such, PcTx1 (~4.8 kDa) is unlikely to reach the brain via conventional parenteral routes such as IV administration. Indeed, intracerebroventricular administration, but not IV, administration of “PcTx1 venom” and PcTx1 provided neuroprotection in rat model for stroke¹⁴¹⁻¹⁴². Interestingly, IN administration of “PcTx1 venom” did result in substantial neuroprotective effects in a rodent model of stroke¹⁴¹, indicating that IN administration of PcTx1 may be able viable route to bypass the BBB and reach the brain. However, as PcTx1 constitutes only ~0.4% of *P. cambridgei* venom¹⁴², it remains unclear if the neuroprotection following IN administration of “PcTX1 venom” was due to PcTx1 inhibition of ASIC1a or from other bioactive molecules present in the venom. Thus, we are interested in understanding the

therapeutic efficacy of pure PcTx1 and differences in its pharmacokinetics following IN and IV administration.

An understanding of a molecule's pharmacokinetic properties is critical to the development and assessment of new therapeutic agents. Detailed analysis of absorption, distribution, metabolism, and excretion (ADME) is required by regulatory agencies that govern the approval process²³⁰. Traditional pharmacokinetic and biodistribution studies for pharmaceutical agents involve blood and tissue sampling at various time-points to determine local concentrations and serum half-life²³². Non-invasive *in vivo* imaging techniques such as positron emission tomography (PET), optical imaging, X-ray computed tomography (CT) and magnetic resonance imaging (MRI) are increasingly being used to investigate the biodistribution and pharmacokinetics of drugs as opposed to conventional tissue biodistribution (*ex vivo*) studies²³³. A distinct advantage of *in vivo* imaging is the ability to perform repeated, serial imaging on the same animal, thereby reducing the number of animals required and providing finer time resolution.

Amongst the *in vivo* imaging techniques, PET and optical imaging are regarded as quantitative or semi-quantitative imaging modes²³⁴ due to their superior detection sensitivity, whereas CT and MRI are normally used for anatomical imaging purposes as they provide better spatial resolution²³⁵⁻²³⁶. As summarised in **Table 4.1**, each imaging technique has advantages and limitations. Hence, combinations of complementary imaging modes (*i.e.* PET/CT or PET/MRI) are used to provide high sensitivity and enhanced anatomical localisation of the molecule in question²³⁷⁻²³⁸.

PET imaging allows quantitative *in vivo* biodistribution studies of molecules labelled with PET tracers (positron-emitting radionuclides) with unparalleled sensitivity. PET tracers undergo radioactive decay resulting in emission of positrons (an anti-electron)²³⁹. The positron travels for 1–2 mm before colliding with an electron, resulting in annihilation and emission of two 511 keV photons that move in opposite (180°) directions. These photons are sensed by the gamma detector and their source location computationally calculated. Thus, the detection of two 511 keV photons can be directly translated to the frequency of annihilation events and distribution of the PET-labelled molecule²³⁹. PET tracers such as carbon-11, oxygen-15, fluorine-18, gallium-68, copper-64, and bromine-

76 have half-lives ranging from 20 min to 16 h²³⁴. Long-lived PET tracers such as zirconium-89 and iodine-124 with half-lives of 3.2 days and 4.2 days are also available²³⁴. The use of PET imaging in the drug development process can be directly translated from animals to humans as it is a clinically relevant imaging technique²⁴⁰. However, PET imaging has several drawbacks, including the exposure to ionising radiation, and thus requires a high level of technical expertise. It is also limited by the half-lives of radionuclides, high cost of radionuclide production, and the generation of radioactive waste.

Compared to PET imaging, optical imaging using near-infrared (NIR) probes provides a simpler, non-ionising and relatively sensitive method for *in vivo* imaging. The use of probes at NIR wavelengths (750–900 nm) enables clearer discrimination between the signal from the probe and background autofluorescence (*i.e.*, better signal-to-noise ratio). Biological materials such as hemoglobin have $\lambda_{\max} < 600$ nm while water has $\lambda_{\max} > 1150$ nm; thus, in the NIR spectral range, absorbance by biological materials is minimised, allowing deeper penetration of NIR wavelengths (several centimeters) through biological tissues²⁴¹. However, NIR probes are often large, organic molecules, which may also confound the pharmacokinetics and biodistribution of the molecule being studied²⁴².

A major caveat of PET and NIR optical imaging is their relatively lower spatial resolution as compared to CT or MRI²³⁷⁻²³⁸. To circumvent this issue, multimodal imaging approaches, such as PET/CT²³⁷ and, more recently, PET/MRI²⁴³ enables imaging with both high sensitivity and high anatomical resolution. In CT imaging, X-rays are used to generate image contrast based on differences in absorptivity of X-ray in different tissues. Multiple X-ray slices are taken then computationally assembled and reconstructed into 3D images.

In comparison, MRI provides better contrast in soft tissues such as the brain, using the intrinsic properties of protons in different tissues (such as water or fat) to generate contrast²⁴⁴. The magnetic dipole moment of protons are aligned with the external magnetic field of an MRI machine. Radiofrequency (rf) pulses are then used to disrupt the alignment. When protons return to their initial alignment (*i.e.* aligned with the external magnetic field) via a process known as relaxation, they lose energy by emitting

rf radiation that is detected by a receiver coil. Thus, image contrast is based on the differences in relaxation properties and density of protons, which influence the signal intensity obtained. Tissues with higher water content (slow relaxation) have different signal intensity as compared to tissue with higher fat content (fast relaxation)²⁴⁵.

Table 4.1: Comparison of PET, MRI and NIR imaging^{235, 237-238, 241}.

	Basis	Spatial resolution	Depth	Detection (M)	Advantages	Disadvantages
PET	Detection of γ rays from radionuclide decay	0.2–2 mm	No limit	10^{-11} – 10^{-12}	Highest sensitivity, isotopes can substitute natural atoms	Requires cyclotron, short-lived isotopes, low spatial resolution, exposure to radiation, cost.
MRI	Detection of changes in electromagnetic properties of protons with radiofrequency pulses	25–200 μm	No limit	10^{-3} – 0^{-5}	High resolution, combines functional and morphological visualisation	Time consuming, low sensitivity hence requiring large amount of probes, cost
Optical	Optical imaging of fluorescent probes at 700–900 nm where tissue absorption and autofluorescence is minimal	1–3 mm	< 7 cm	10^{-6} – 10^{-9}	High sensitivity, Fast, low cost,	Low spatial resolution. Low tissue depth
CT	Generation and compilation of axial slices of X-ray images	50–120 μm	No limit	NA	High resolution	Exposure to ionising radiation which could led to cell damage. Poor soft tissue contrast.

In order to evaluate the efficiency of IN administration as a method for CNS delivery of venom peptides, we decided to use PcTx1 as a model peptide. PcTx1 is a highly potent ASIC1a inhibitor which had been used extensively in *in vivo* studies with no reports of toxicity¹⁴¹. Moreover, there have been extensive structure-activity relationship (SAR) studies undertaken on PcTx1, providing a clear understanding of the epitopes important for activity, and sites that can be manipulated without affecting its inherent function. Most importantly, neuroprotection of the brain was observed with IN administration of *P. cambridgei* venom in a mouse model of stroke, strongly that IN administration is a plausible method for delivering PcTx1 to the CNS. Hence, we decided to combine *in*

in vivo imaging techniques and traditional *ex vivo* tissue sampling to study the uptake of PcTx1 in the brain following IN administration.

Given that one single imaging mode is unlikely to be sufficient to completely understand the pharmacokinetics and biodistribution of PcTx1, we employed different labelling strategies to allow use of different methods of *in vivo* imaging of PcTx1. This chapter describes the production and characterisation of PcTx1 analogues and studies of their pharmacokinetics and biodistribution using PET, MRI and NIRF imaging.

4.2 Materials and Methods

4.2.1 Recombinant expression and purification of PcTx1 and Tyr_NPcTx1

Recombinant PcTx1 (wild-type) and the variant Tyr_NPcTx1 (i.e., PcTx1 with an additional N-terminal Tyr residue) were produced using the *E. coli* periplasmic system described in **Chapters 2** and **3**. The non-native tyrosine in Tyr_NPcTx1 was introduced via site-directed mutagenesis of the WT PcTx1 plasmid using standard PCR protocols²⁴⁶.

4.2.2 Solid-Phase Peptide Synthesis of AHA-PcTx1 (azPcTx1)

In order to achieve site-specific coupling through azide-alkyne Huisgen cycloaddition, a variant of PcTx1 (azPcTx1) containing L-azidohomoalanine (AHA) was synthesised by Mr Zoltan Dekan (IMB, University of Queensland, Australia). The peptide was produced using standard solid-phase peptide synthesis (SPPS) protocol with 9-fluorenylmethyloxycarbonyl (Fmoc) as the α -amino protecting group. The side-chain protecting groups were Arg(Pbf), Asn(Trt), Asp(OtBu), Cys(Trt), Glu(OtBu), His(Trt), Lys(Boc), Ser(tBu), Thr(tBu) and Trp(Boc) (Chem-Impex International, Illinois, USA)

The peptide was synthesised (0.1 nmol scale) using a Symphony Automated Peptide Synthesiser (Protein Technologies Inc. Arizona, USA) on Fmoc-Thr(tBu)-Wang polystyrene resin (loading 0.68 nmol/g) (Peptides International Inc., Kentucky, USA). Chain assembly was performed following an established *in situ* neutralisation method²⁴⁷. Briefly, Fmoc deprotections were achieved using 30% piperidine in dimethylformamide (DMF) (1 x 1.5 min, then 1 x 4 min). Amino acid couplings (2 x 20 min) were performed in DMF using five equivalents of Fmoc-amino acid/2-(1H-

Benzotriazole-1-yl)-1,1,3,3-tetramethyluronium hexafluorophosphate (HBTU)/diisopropylethylamine (DIEA), at 1:1:1 ratio, relative to resin loading capacity. After assembly of the peptide chain, the resin was rinsed with 50% methanol (MeOH) and dichloromethane (DCM) then dried under vacuum.

Cleavage from resin and removal of side-chain protecting groups was achieved by treatment with 50 mL of 95% TFA/2.5% triisopropylsilane (TIPS)/2.5% H₂O at room temperature for 2 h. After most of the cleavage solution was evaporated under a stream of N₂, the products were precipitated and washed twice with cold diethyl ether (Et₂O) and lyophilised from 50% MeCN/0.1% TFA/H₂O. Electrospray ionisation mass spectrometry (m/z): calculated (average) [calc. (avg.)] [M+4H]⁴⁺ = 1206.4, observed = 1206.3.

The purified linear peptide was oxidised as follows: peptide (50 mg), reduced glutathione (100 equiv.) and oxidised glutathione (10 equiv.) were dissolved in 50 mL of 8 M urea then added to a 450 mL of 5 M NH₄OAc (pH 8.0) and stirred for 3 days at 4°C with exposure to air. The refolding was monitored using analytical RP-HPLC.

4.2.3 Synthesis of alkyne DOTA (1,4,7,10-tetraazacyclododecanetetraacetic acid) tags

DOTA-propargylglycine (1xDOTA) and 4xDOTA-DBCO (4xDOTA) were manually assembled (0.1 mmol scale) on a Fmoc-propargylglycine (Boc)-Rink polystyrene resin (loading 0.62 mmol/g). Amino acid or DOTA side-chains were protected as follows; propargylglycine(Fmoc), Lys(Boc), Lys(Fmoc), DOTA(tBu).

The synthesis strategies for 1xDOTA and 4xDOTA are shown in **Fig. 4.3**. Fmoc deprotections were achieved using 50% piperidine/DMF (1 x 2 min, then 1 x 4 min). Couplings were performed in DMF using four equivalents of Fmoc-amino acid/HATU (1-[Bis(dimethylamino)methylene]-1H-1,2,3-triazolo[4,5-b]pyridinium 3-oxid hexafluorophosphate)/DIEA (1:1:1) relative to resin loading for 1 x 20 min. Overnight coupling of DOTA-tri-t-Bu-ester was performed in DMF using 1.5 equivalents of t-Bu-DOTA/HATU/DIEA (1:1:1). Cleavage from the resin and removal of side-chain protecting groups was achieved by treatment with 95% TFA/2.5% TIPS/2.5 % H₂O at room temperature for 4 h. The cleavage solution was evaporated under a stream of N₂,

the products were precipitated and washed with cold Et₂O then lyophilised from 50% MeCN/0.1% TFA/H₂O.

Derivatisation of the 4xDOTA with a dibenzocyclooctyne (DBCO) functional group was achieved by incubating 3 equiv. of 4xDOTA with 1 equiv. of dibenzocyclooctyne-*N*-hydroxysuccinimidyl ester (DBCO-NHS ester) in 0.1 M sodium phosphate, pH 7.6 for 4 h. The product was purified using RP-HPLC and quantified based on UV absorbance at 309 nm (ϵ_{309} DBCO = 12,000 M⁻¹.L.cm⁻¹). ESI MS (m/z): calculated (average) 499.5 [M+H]¹⁺, found 499.4 (1xDOTA); MALDI-TOF MS (m/z): calculated 2362 [M+H]¹⁺, found 2365.9 (4xDOTA).

4.2.4 Azide-alkyne Huisgen cycloaddition

Coupling between azPcTx1 and the alkyne imaging moiety was achieved using Cu(I)-catalysed azide/alkyne cycloaddition (CuAAC)²⁴⁸ using one equiv. of azPcTx1 with two equiv. of alkyne. The reaction was carried out in 50 mM MES, pH 6 buffer containing 0.5 mM copper(II) sulphate, 2.5 mM Tris(3-hydroxypropyltriazolylmethyl)amine (THPTA), and 6.3 mM aminoguanidine hydrochloride. The reaction was initiated by addition of 6.3 mM sodium ascorbate then the mixture was incubated overnight at room temperature with gentle mixing. Due to the possibility of copper chelation by DOTA, the 1xDOTA tag was preloaded with gadolinium by incubating it with 10 equiv. of gadolinium chloride (GdCl₃) in 50 mM MES buffer at pH 6 for > 12 h.

A copper-free click chemistry was used for coupling of azPcTx1 and the 4xDOTA tag using Strain-Promoted [3 + 2] Azide-Alkyne Cycloaddition (SPAAC)²⁴⁹. The reaction mixture contained 1 equiv. of azPcTx1 and 1.5 equiv. of 4xDOTA tag in 50 mM MES, pH 6 buffer. The 4xDOTA tag was also chelated with 40 equiv. of GdCl₃ concurrently in the same reaction vessel. The mixture was incubated for > 12 h and purified using RP-HPLC.

4.2.5 Relaxation studies of DOTA-labelled peptides

Data and image acquisition for MR relaxation studies of aqueous azPcTx1, Gd-DOTA-PcTx1 and 4x-Gd-DOTA-azPcTx1 solutions (20, 50 and 150 μM) were acquired on a Bruker Biospec 9.4 T small animal imaging spectrometer (Ettlingen, Germany) by Dr Yas Tesiram (CAI, University of Queensland). Longitudinal relaxation times (T₁) for

these samples were measured using a saturation recovery with a spin echo data acquisition scheme. In this experiment the echo time (T_E) was kept constant at 7 ms, and the repetition time (T_R) was varied ($T_R = 988\text{--}10000$ ms). For the images, the field of view (FOV) was 12×12 mm, matrix = 96×96 , slice thickness = 0.5 mm, and number of averages = 2. Transverse relaxation times (T_2) were measured using a multi-slice multi-echo (MSME) sequence with 128 echoes. The experimental parameters were $T_R = 10000$ ms, $T_E = 0.06\text{--}0.768$ s, FOV = 12×12 mm, matrix = 96×96 , slice thickness = 0.5 mm.

MR images were analysed using ImageJ²⁵⁰ and mean signal intensity calculated from circular regions of interest (ROI) of the samples (**Fig. 4.6A,B**) to obtain plots of signal intensity against T_R or T_E (**Fig. 4.6C,E**). The recovery curves for T_1 and T_2 time estimation, were fitted to a non-linear, least square fit, based on a “one-phase decay” equation, using the software Prism 6.0 (La Jolla, USA). The longitudinal relaxivity (r_1) and transverse relaxivity (r_2) of the compounds were calculated from the slopes of the plots of $1/T_1$ and $1/T_2$ versus the sample concentrations. All curve fitting and statistical analysis were performed using Prism 6.0 (La Jolla, USA).

4.2.6 Iodination of Tyr_N_PcTx1

Tyr_N_PcTx1 was iodinated using chloramine-T²⁵¹. Briefly, 7.5 μ l of 0.1 M sodium iodide (7.5 nmol) was added to Tyr_N_PcTx1 (7.5 nmol) in 135 μ l of 0.1 M phosphate buffer, pH 7.5. The reaction was initiated by adding 15 μ l of 3 mM chloramine T (15 nmol) with gentle mixing. The mixture was incubated for 1 min at room temperature, then diluted to 0.5 mL with Solvent A. Separation of unlabelled, mono-iodinated, and di-iodinated PcTx1 was performed using analytical C₁₈ RP-HPLC and isolated products confirmed using mass spectrometry.

4.2.7 Two-electrode voltage clamp electrophysiology (TEVC)

The ASIC1a inhibitory activity of PcTx1 variants (modified with different imaging moieties) was assessed using TEVC electrophysiology on *X. laevis* oocytes. Oocyte digestion, cDNA/cRNA preparation, injections and data analysis were performed as described in **Chapter 3**.

4.2.8 Thermal, serum and cerebrospinal fluid stability assay

The thermal and metabolic stability of PcTx1 was assessed at 55°C using human serum or human CSF as described in **Chapter 3**.

4.2.9 Iodine-124 iodination and TLC purification

Iodination of Tyr_N-PcTx1 and TLC purification of iodinated products was performed by Dr Rajiv Bhalla (CAI, University of Queensland). Lyophilised Tyr_N-PcTx1 (200 µg) was reconstituted in 300 µL of 0.1 M phosphate buffer pH 7.45, and added to an iodogen tube (Thermo Scientific, Australia). Then, iodine-124 (¹²⁴I, produced in-house as sodium iodide at CAI), dissolved in 100 µL of 0.05 M NaOH, was added to the same iodogen tube. The tube was capped and gently agitated then incubated at room temperature for ~35 min. The labelling efficiency and radiochemical purity were determined using instant thin-layer chromatography strips (iTLC) (Agilent Technologies, Australia) using saline as the mobile phase. The result from iTLC was verified with RP-HPLC on a C₁₈ column (Agilent ZORBAX Eclipse Plus, 150 x 4.6 mm x 5 µm, 95 Å) using a gradient of 15–35 % Solvent B over 20 min.

4.2.10 in vivo PET/CT imaging

PET/CT data were acquired using an Inveon multimodality PET/CT imaging scanner (Siemens, Australia). Animal preparation, peptides administration, PET/CT data acquisition, organs harvesting, gamma counting, data acquisition and image analyses were performed by Dr Karine Mardon (CAI) and/or Ms Xin Song (CAI). Briefly, mice were anaesthetised with isoflurane (IsoFlo, Abbott Laboratories) at a dose of 2% in a closed anaesthetic induction chamber. Mice were monitored using ocular and pedal reflexes to ensure deep anaesthesia. Once the mouse was deeply anaesthetised, it was placed on an appropriate animal bed, where the anaesthetic air mixture (1%) was delivered to its nose and mouth through a nose cone. Physiological monitoring (respiration using a sensor probe) was achieved throughout all experiments using an animal monitoring system (BioVetTM system, m2m Imaging, Australia). The radiolabelled ¹²⁴I-PcTx1 was administered intravenously (1.5–2.0 MBq) through the tail vein or via the intranasal route (0.5–0.3 MBq).

For IV administration, the injection syringe was filled with the radioisotope solution (approximately 150 μL in 0.1 M phosphate buffer, pH 7.45) and the activity in the syringe was measured using a dose calibrator (Capintec CRC-25, USA). The activity left in the syringe after the tail vein injection was measured using the same dose calibrator and the total volume injected into each mouse was calculated. For IN administration, mice were first placed in a supine position, then a 2.5–5 μL droplet of ^{124}I -PcTx1 was pipetted into the nostril. The process was repeated several times using alternating nostrils until the required dosage was achieved. The maximum volume administered was 20 μL per mouse.

Following injection of the radiotracer, PET Images were acquired for 90 min (dynamic acquisitions) or 30–60 min (static acquisitions) following IV or IN administration, respectively. PET Images were reconstructed using an ordered-subset expectation maximisation (OSEM2D) algorithm and analysed using the Inveon Research Workplace software (IRW 4.1) (Siemens). Immediately after PET acquisition, CT scans were acquired for anatomical co-registration. The CT images of the mice were acquired through an X-ray source with the voltage set to 80 kV and the current set to 500 μA . The scans were performed using 360° rotation via 120 rotation steps with a low magnification and a binning factor of four. The exposure time was 230 ms with an effective pixel size of 106 μm . The total CT scanning process took approximately 15 min. The CT images were reconstructed using Feldkamp reconstruction software (Siemens).

Following CT imaging, fusion of CT and PET images and definition of regions of interest (ROIs) were performed using IRW 4.1. CT and PET datasets of each individual animal were aligned using IRW software (Siemens) to ensure good overlap of the organs of interest. Three-dimensional ROIs were placed within the whole body, as well as all the organs of interest, using morphologic CT information to delineate organs. Activity per voxel was converted to nci/cc using a conversion factor obtained by scanning a cylindrical phantom filled with a known activity of ^{124}I to account for PET scanner efficiency. Activity concentrations were then expressed as percent of the decay-corrected injected activity per cm^3 of tissue that can be approximated as percentage injected dose/g (%ID/g). The dynamic tracer uptake was calculated post reconstruction of PET data sets into 35 frames.

4.2.11 Post mortem biodistribution study

At various time points after administration of the radiotracer, tissue samples were collected for gamma counting in a collaborative effort with Dr Karine Mardon and Ms Xin Song (CAI) in order to determine peptide biodistribution. Mice were injected in a group of four at $t = 0$ and sacrificed at different time points after injection of ^{124}I -PcTx1. For IN administration, mice were given a dose of approximately 0.30–1.00 MBq in a maximum volume of 20 μL . Anesthetised mice were sacrificed by cervical dislocation and organs including, heart, lung, liver, spleen, kidney, stomach, gut, muscle, nose and brain were surgically removed, weighed and placed in tubes. The brains were further dissected into different regions including medulla pons, cerebellum, midbrain, hypothalamus, hippocampus, striatum, frontal cortex, posterior cortex and olfactory bulb. Radioactivity was counted using a gamma counter (Wizard 2480, Perkin Elmer). Tissue uptake was obtained based on the specific activity of ^{124}I -labelled Tyr_N-PcTx1 (determined from standards sampled from the dose solution), counts per minute in the tissue following subtraction of background radioactivity, and tissue weight in grams. Radioactivity concentrations were then expressed as percent of the decay-corrected injected activity per g of tissue that can be approximated as percentage injected dose/g (%ID/g). Dose-normalised concentrations in brain from intranasal experiments were calculated and expressed in nmol/L (assuming a density of 1 g/mL).

4.2.12 Reversed-phase high performance liquid chromatography

Unless otherwise stated, RP-HPLC fractionations were performed as described. Preparative RP-HPLC was performed with a C₈ column (Grace Vydac, 250 x 22 mm) attached to a Ultimate 3000 LC system (Dionex, Sunnyvale, USA). Semi-preparative or analytical RP-HPLC was performed on a Prominence HPLC system (Shimadzu, Kyoto, Japan) with a C₄ semi-preparative column (Phenomenex Jupiter, 250 x 10 mm x 10 μm , 300 Å) at 5 mL/min; C₁₈ analytical column (Phenomenex Kinetex, 250 x 4.6 mm x 5 μm , 100 Å) at 1 mL/min; C₁₈ narrow-bore column (Thermo Hypersil, 100 x 2.1 mm x 5 μm , 180 Å) at 0.3 mL/min. Fractions were separated using a gradient of Solvent A (0.05% TFA in H₂O) and Solvent B (0.043% TFA, 90% MeCN in H₂O). Fractions were manually collected based on UV absorbance at 214 nm and 280 nm. All solvents used were HPLC-grade.

4.2.13 Mass determination

Peptide masses were obtained using electrospray ionisation mass spectrometry (ESI-MS; (LCMS-2020 Shimadzu, Kyoto, Japan) or matrix-assisted laser desorption/ionisation time-of-flight mass spectrometry (MALDI-TOF MS) using a Model 4700 Proteomics Bioanalyser (Applied Biosystems, Carlsbad, USA). For MALDI-TOF MS, samples were spotted 1:1 (v/v) with α -cyano-4 hydroxycinnamic acid matrix (CHCA) (7 mg/mL in 50% acetonitrile/1% formic acid in H₂O). Observed masses are reported as monoisotopic m/z or average mass.

4.2.14 Animals

Male wild-type (C57BL6) mice, ~12–15 weeks old, weighing 25–30g, were obtained from local breeding colonies (University of Queensland Biological Resources, Australia). Mice were maintained under standard conditions in clean holding facilities on a 12 h light–dark cycle with *ad libitum* access to food and water. All procedures for *X. laevis* oocytes electrophysiology studies and mice PET/CT biodistribution studies were in compliance with the Australian code of practice for care and use of animals for scientific purposes and approved by The University of Queensland Animal Ethics Committee (Approval number QBI/059/13/ARC/NHMRC and CAI/398/14/NHMRC). Oocytes were obtained by trained personnel via recovery surgery performed on mice under tricaine methanesulfonate anaesthesia. The minimum time between surgeries on the same animal was 3 months.

4.3 Results

4.3.1 Recombinant expression and purification of PcTx1 variants

Recombinant Tyr_N-PcTx1 was produced using the *E. coli* periplasmic expression system (**Fig. 4.1A**) described in Chapter 2. **Fig. 4.1B** shows an SDS-PAGE gel illustrating various stages in the expression and purification of Tyr_N-PcTx1. Following IPTG induction, the His₆-MBP-PcTx1 fusion protein (~43 kDa) was the major cellular protein produced (**Fig. 4.1B**, compare *lanes 2 and 3*). The majority of the fusion protein was soluble with a small amount in the insoluble fraction (**Fig. 4.1B**, compare *lanes 4 and 5*). Following Ni-NTA purification, the soluble fusion protein was obtained in high purity as indicated by a single protein band at 43 kDa (**Fig. 4.1B**, *lanes 6–8*). The

peptide was liberated from the fusion protein using TEV protease as indicated by a ~4.5 kDa shift of the protein band on SDS-PAGE (Fig. 4.1B, compare lanes 9 and 10). The cleavage mixture containing Tyr_N_PcTx1 was purified using semi-preparative C₄ RP-HPLC (Fig. 4.1C), then further purified to >95% purity as judged by the elution of a single peak on analytical C₁₈ RP-HPLC (Fig. 4.1D). The observed monoisotopic mass for recombinant Tyr_N_PcTx1 (4774.29) is in agreement with the theoretical monoisotopic mass of 4774.21 (Fig. 4.1D inset).

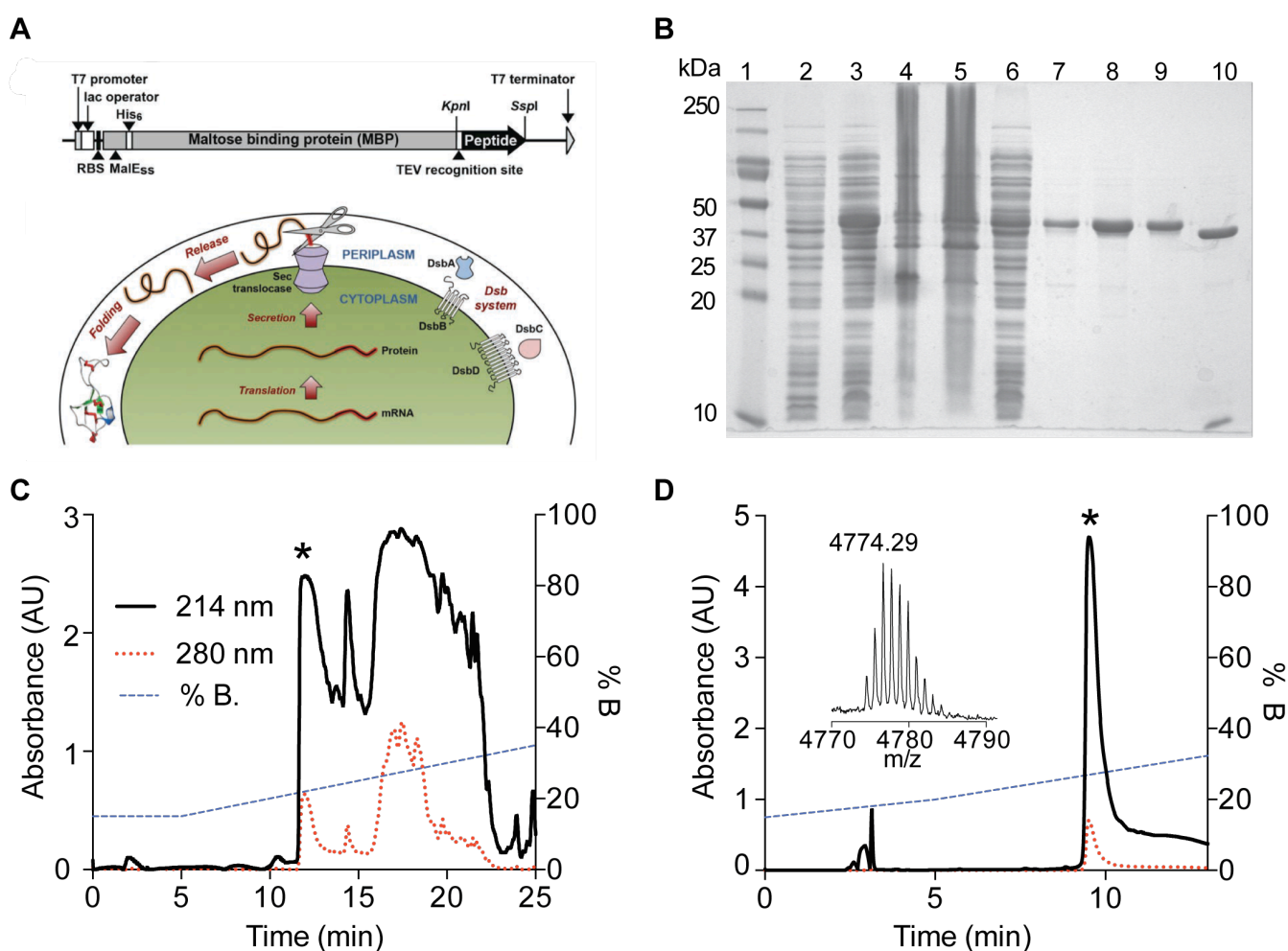


Figure 4.1. (A) Top panel: Schematic representation of the coding region of the pLic-MBP expression vector. This IPTG-inducible plasmid contains genetic components encoding the MalE_{SS}-His₆-MBP-peptide fusion protein with a TEV protease recognition site between the MBP and toxin coding regions and an IPTG-inducible Lac operon. Bottom panel: An illustration of the *E. coli* periplasmic expression system. The fusion protein is expressed within the cytoplasm. The MalE signal sequence directs the translocation of the fusion protein to the periplasm via the SecYEG translocase system. The Dsb machinery in the periplasm catalyzes the formation of disulfide bonds. (B) SDS-PAGE gel showing various steps in the expression and purification of Tyr_N_PcTx1. The lanes (from left to right) are as follows: (1) molecular weight markers; (2) whole-cell extract before IPTG induction; (3) whole-cell extract after IPTG induction; (4) insoluble fraction after lysis of induced cells; (5) soluble fraction after lysis of induced cells; (6) flow-

through from loading of soluble cell fraction onto Ni-NTA column; (7) eluate from wash of Ni-NTA column with 5 mM imidazole; (8) eluate from wash of Ni-NTA column with 250 mM imidazole; (9) eluted His₆-MBP- Tyr_NPcTx1 fusion protein prior to TEV protease cleavage; (10) His₆-MBP-Tyr_NPcTx1 fusion protein sample after TEV protease cleavage. **(C)** RP-HPLC chromatogram showing purification of Tyr_NPcTx1 from the TEV protease cleavage mixture. **(D)** RP-HPLC chromatograms showing final purification of Tyr_NPcTx1 using an analytical C₁₈ column. Inset shows a MALDI-TOF mass spectrum of the purified peptide. Asterisk denotes peaks with mass corresponding to the theoretical mass of Tyr_NPcTx1.

4.3.2 Chemical synthesis of azPcTx1

Synthesis of azPcTx1 at 0.1 mmole scale resulted in approximately 430 mg of crude material. The m/z (1206.3) of the crude material is in agreement with the theoretical value of 1206.4 ($[M+4H]^{4+}$). The crude product was purified using preparative RP-HPLC to give 110 mg of hexathiol azPcTx1. After refolding (50 mg of crude material), the single major product (**Fig. 4.2, left panel**), was obtained with a final yield of ~22% (11 mg of folded peptide). The observed m/z (1204.7), matched the calculated value of 1204.9 ($[M+4H]^{4+}$) (**Fig. 4.2, right panel**), of the folded peptide. The IC₅₀ of ~1.2 nM obtained for inhibition of rASIC1a by azPcTx1 (data not shown) is in agreement with published values for PcTx1 (IC₅₀ ~1 nM)¹⁰³⁻¹⁰⁴, indicating that peptide activity is unaffected by the azide modification.

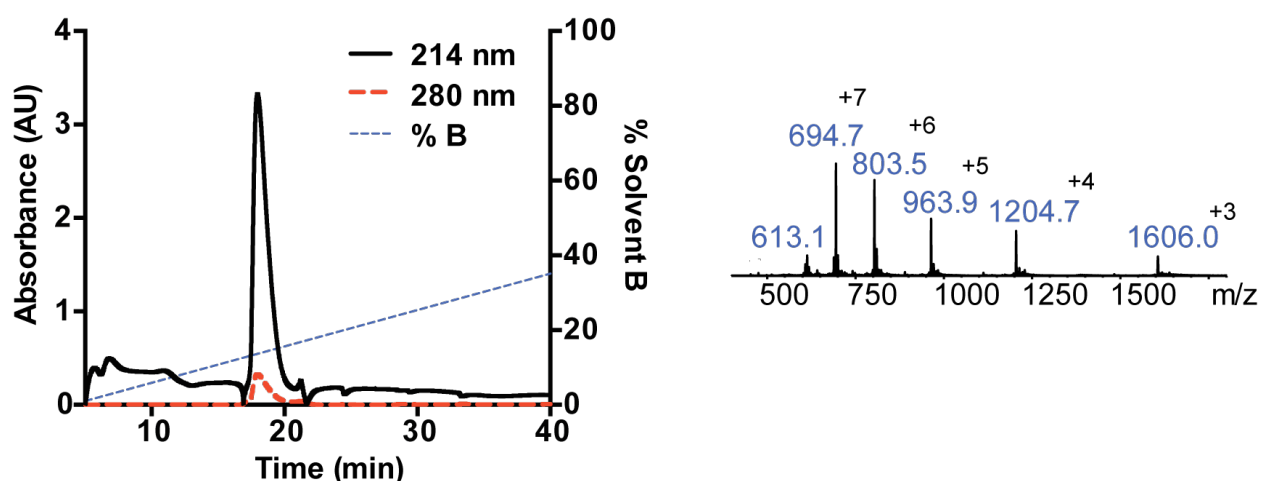


Figure 4.2 Purification of azPcTx1 (Experiment performed by Mr Zoltan Dekan). **Right:** RP-HPLC chromatogram showing purification of azPcTx1 from folding reaction mixture. **Left:** ESI mass spectrum of purified folded azPcTx1.

4.3.3 Synthesis, derivatisation and bioconjugation of imaging moieties

Alkyne DOTA tags were synthesised from DOTA-tri-tBu-ester (Macrocyclics™, TX, USA) as illustrated in **Figure 4.3**. Following removal of the protecting group (tBu), the observed m/z of the product (499.1 for the $[M+H^+]$ ion) is in agreement with the calculated molecular weight (MW) (498.5 Da) (**Fig. 4.3 inset**). The 4xDOTA tag was assembled with Fmoc-protected lysines for the incorporation of four DOTA groups and DBCO-NHS. The average m/z of the product (2365.99, in linear mode) is in agreement with the calculated MW (2362.67 Da) (**Fig. 4.3 inset**).

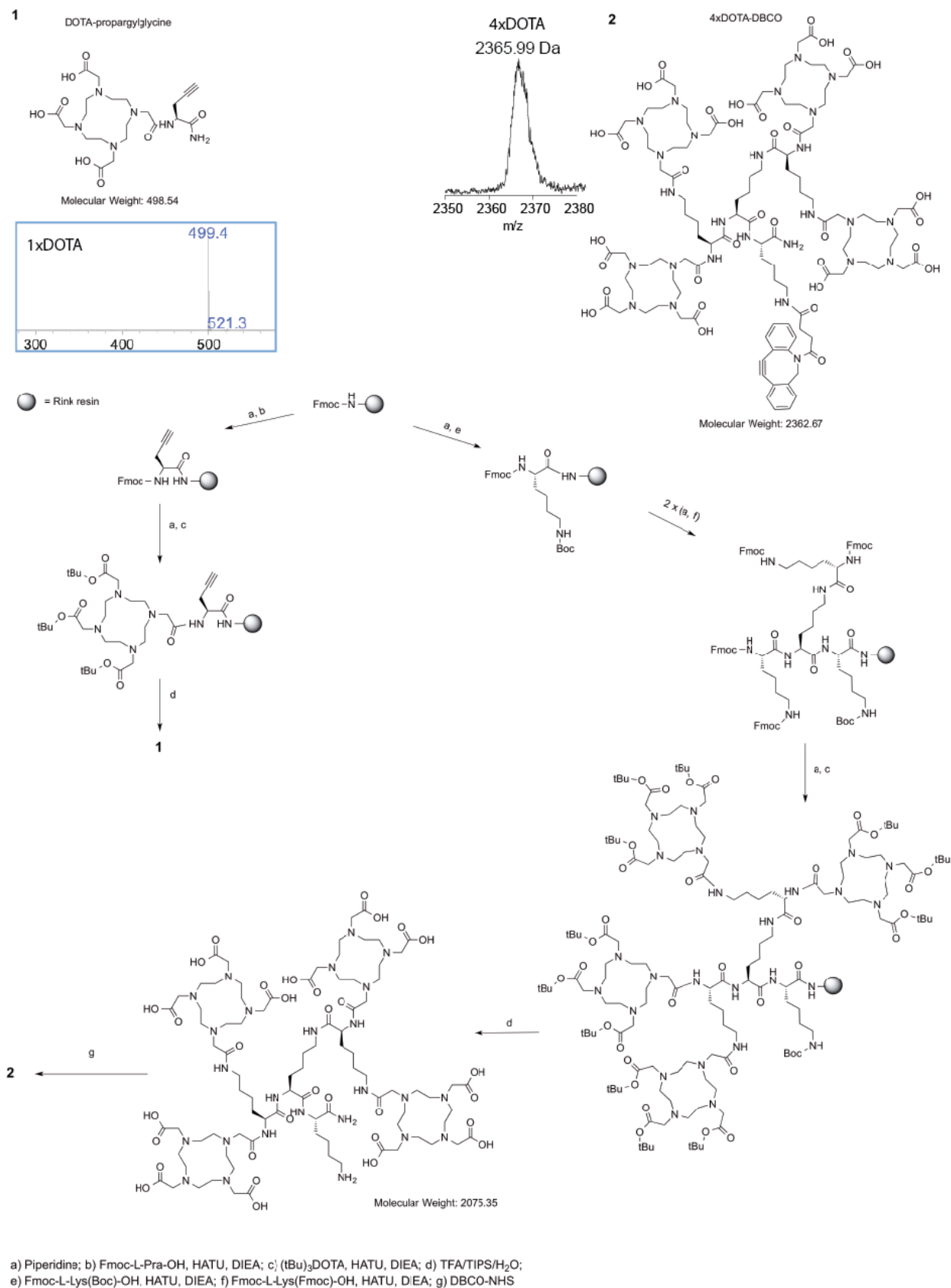


Figure 4.3. Schematic of 1xDOTA (synthesised by Mr Zoltan Dekan) and 4xDOTA synthesis using Fmoc SPPS. Inset shows mass spectra obtained using ESI and MALDI-TOF MS of the crude products after ether precipitation.

Prior to CuAAC, the 1xDOTA tag was chelated with Gd^{3+} to prevent chelation of Cu(I) by DOTA. Following CuAAC, a single product (Gd-DOTA-azPcTx1) was obtained as judged by RP-HPLC (**Fig. 4.4A**). The average m/z (5471.24) is in agreement with the calculated MW (5468.3 Da), which corresponds to the combined mass of azPcTx1 (MW: 4815.6 Da), 1xDOTA (MW: 498.5 Da) and Gd^{3+} ion (MW: 154.3 Da) (**Fig. 4.4A inset**).

The 4xDOTA tag was conjugated to azPcTx1 via SPAAC and chelated with Gd^{3+} concurrently. As shown using RP-HPLC, the reaction was highly specific and efficient with a single product obtained (4x-Gd-DOTA-azPcTx1) (**Fig. 4.4B**). The observed average isotopic mass (m/z 7796.3) from MALDI is in good agreement with the calculated MW (7795.7 Da), which corresponds to the combined mass of azPcTx1 (MW: 4815.6 Da) coupled with the 4xDOTA tag (2362.7 Da) coordinated with four Gd^{3+} ions (617.0 Da) (**Fig. 4.4B inset**).

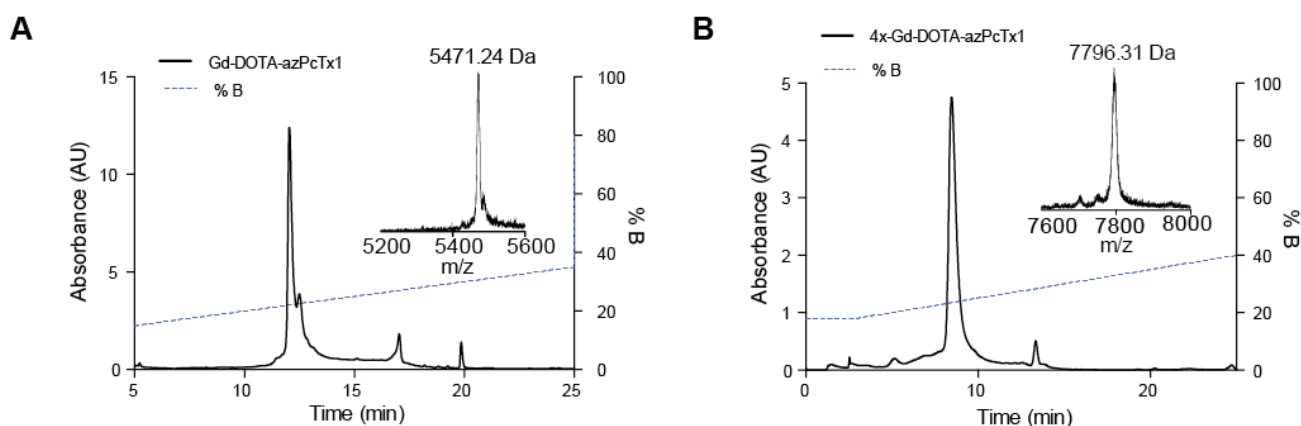


Figure 4.4. Labelling of azPcTx1 with various imaging moieties. **(A)** RP-HPLC of Gd-DOTA-azPcTx1. Inset shows MALDI mass spectrum of product with an average m/z of 5471.24 Da. **(B)** RP-HPLC of 4x-Gd-DOTA-azPcTx1. Inset shows the MALDI mass spectrum of product with average m/z of 7796.31 Da.

4.3.4 Iodination of PcTx1

Prior to radiolabelling of Tyr_N -PcTx1 with ^{124}I for PET imaging, a trial iodination trial was performed in order to test the effect of the modification on PcTx1 activity as well as to obtain a standard for subsequent radiolabelling. As indicated in **Fig. 4.5**, iodination of Tyr_N -PcTx1 using chloramine T and sodium iodide resulted in the production of non-, mono- and di-iodinated variants that were easily separated using RP-HPLC. The observed m/z of non-, mono- and di-iodinated variants are as indicated (**Fig 4.5 insets**).

The mass increment of 125.91 Da and 251.97 Da is indicative of iodination of the tyrosyl group. The activity of Tyr_NPcTx1 and its iodinated version was assessed using TEVC studies on *X. laevis* oocytes expressing rASIC1a. As compared to WT PcTx1 (IC₅₀ = 0.47 nM), the addition of an N-terminal Tyr resulted in a ~3-fold decrease in activity (IC₅₀ = 1.83 nM). The activity decreased further by 4- and 8-fold with the addition of one (IC₅₀ = 8.37 nM) and two iodines (IC₅₀ = 15.03 nM), respectively (**Table 4.2**). Nevertheless, all of the iodinated derivatives are potent inhibitors of rASIC1a.

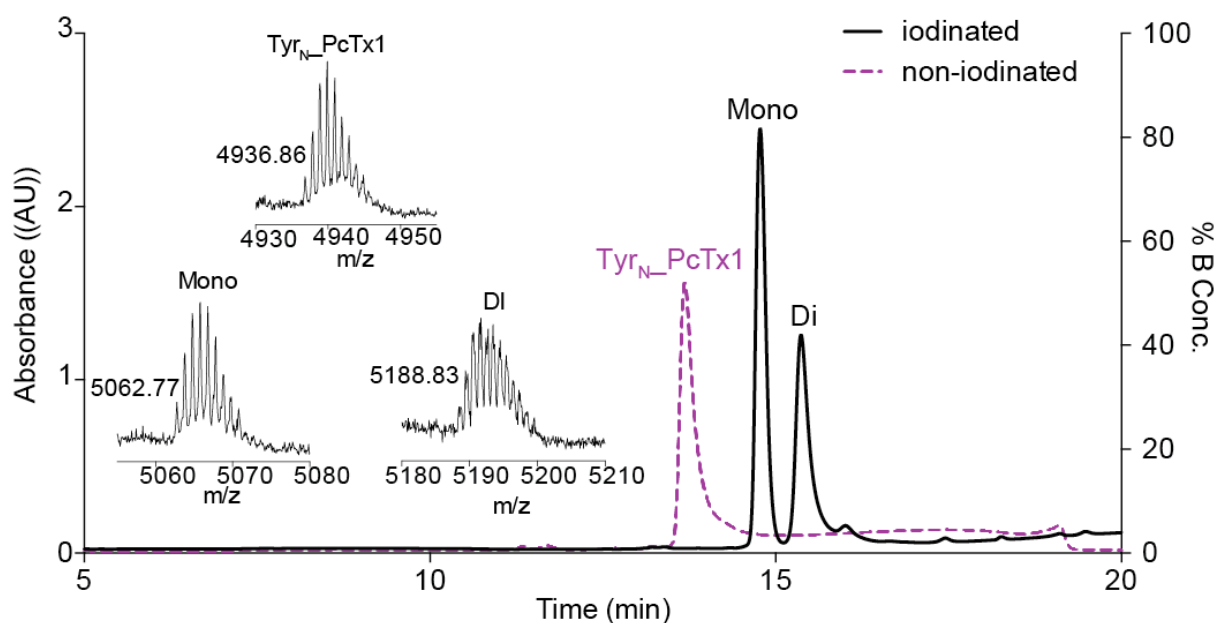


Figure 4.5. RP-HPLC chromatograms showing purification of PcTx1_{Tyr_N} before iodination (dashed, purple) and after iodination (black). Peaks corresponding to the mass of the mono-iodinated (Mono) and di-iodinated (Di) Tyr_NPcTx1 are as indicated. Inset shows MALDI-TOF mass spectra of corresponding peaks with monoisotopic M+H⁺ of 4936.86 (Tyr_NPcTx1), 5062.77 (mono-iodinated) and 5188.83 (di-iodinated).

Table 4.2. IC₅₀ values for inhibition of rASIC1a by PcTx1 and Tyr_NPcTx1 (mean ± SEM; n = 4). The modification in the Tyr_NPcTx1 sequence is highlighted in red.

PcTx1 variant	Sequence	IC ₅₀ (nM)
PcTx1	SEDCIPKWKGCVNRHGDCCGLECWKRRRSFEVCVPKTPKT	0.47 ± 0.05
Tyr _N PcTx1	SEDCIPKWKGCVNRHGDCCGLECWKRRRSFEVCVPKTPKT	1.83 ± 0.47
Tyr _N mono_PcTx1	S YEDCIPKWKGCVNRHGDCCGLECWRRRSFEVCVPKTPKT	8.37 ± 3.00
Tyr _N Di_PcTx1	S YEDCIPKWKGCVNRHGDCCGLECWRRRSFEVCVPKTPKT	15.03 ± 2.58

4.3.5 Longitudinal and transverse relaxation of Gd³⁺ loaded DOTA-azPcTx1

Longitudinal (T_1) and transverse (T_2) relaxation profiles (Fig. 4.6A,B,C,E) and relaxivity (Fig. 4.6D,F) for azPcTx1, Gd-DOTA-azPcTx1 and 4x-Gd-DOTA-azPcTx1 were determined at a magnetic field strength of 9.4 T. As summarised in Table 4.2, there were no significant differences in the longitudinal or transverse relaxation rates of azPcTx1 over the concentration range 20–150 μM . In comparison, both Gd-DOTA-azPcTx1 and 4x-Gd-DOTA-azPcTx1 displayed concentration-dependent enhancement in longitudinal (~2–3 fold) and transverse (~1.5–2.4 folds) relaxation rates. The calculated longitudinal relaxivities (r_1) for 1xDOTA-Gd-azPcTx1 and 4xDOTA-Gd-azPcTx1 were $4.60 \pm 0.24 \text{ mM}^{-1}\text{s}^{-1}$ and $9.40 \pm 0.86 \text{ mM}^{-1}\text{s}^{-1}$, respectively, a considerable enhancement compared to the relaxivity of azPcTx1 ($-0.13 \text{ mM}^{-1}\text{s}^{-1}$). Similarly, both compounds were shown to enhance transverse relaxivity (r_2) as compared to azPcTx1 ($0.67 \pm 0.49 \text{ mM}^{-1}\text{s}^{-1}$). The calculated transverse relaxivity for Gd-DOTA-azPcTx1 and 4x-Gd-DOTA-azPcTx1 is $11.63 \pm 0.36 \text{ mM}^{-1}\text{s}^{-1}$ and $40.72 \pm 0.18 \text{ mM}^{-1}\text{s}^{-1}$, respectively.

Table 4.3: Summary of the longitudinal and transverse relaxation times (T_1 and T_2), rates (R_1 and R_2) and relaxivity (r_1 and r_2) of PcTx1, 1xDOTA-Gd-PcTx1 and 4xDOTA-Gd-PcTx1

Concentration (μM)	azPcTx1			Gd-DOTA-azPcTx1			4x-Gd-DOTA-azPcTx1		
	20	50	150	20	50	150	20	50	150
T_1 (sec)	2.646	2.663	2.773	2.050	1.521	0.913	1.563	0.965	0.527
R_1 ($1/T_1$)	0.378	0.376	0.361	0.488	0.658	1.096	0.640	1.036	1.897
r_1 ($\text{mM}^{-1} \text{s}^{-1}$)	-0.137 ± 0.013			4.60 ± 0.24			9.40 ± 0.86		
T_2 (sec)	0.335	0.341	0.328	0.307	0.281	0.211	0.266	0.200	0.110
R_2 ($1/T_2$)	2.982	2.937	3.049	3.254	3.555	4.751	3.767	5.013	9.066
r_2 ($\text{mM}^{-1} \text{s}^{-1}$)	0.67 ± 0.49			11.63 ± 0.36			40.72 ± 0.18		

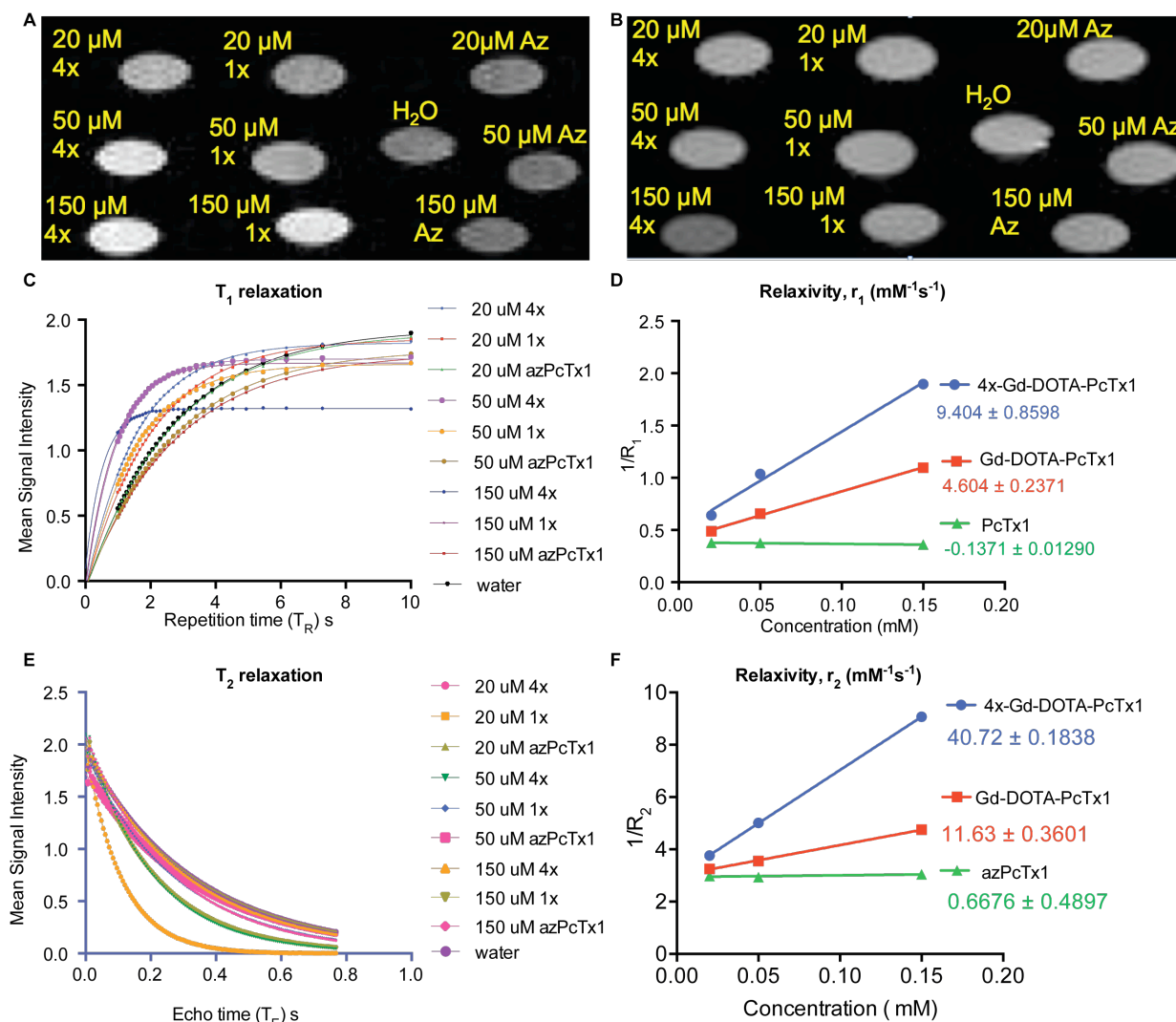


Figure 4.6: Nuclear relaxation of PcTx1 and variants at 9.4 T (MR images acquired by Dr Yas Tesiram). (A) Signal intensities of the various samples in a T_1 -weighted MRI (1x = Gd-DOTA-azPcTx1, 4x = 4x-Gd-DOTA-azPcTx1 and Az = azPcTx1) at a specific repetition time. (B) Signal intensities of the various samples in a T_2 -weighted MRI at a specific repetition time. (C) Plot of mean signal intensity versus repetition time (T_R). (E) Plot of mean signal intensity versus echo time (T_E) for T_2 relaxation. (D and F) Relaxivity of Gd^{3+} -loaded DOTA PcTx1 obtained by plotting the T_1 and T_2 relaxation rates against peptide concentrations.

4.3.6 Activity of labelled PcTx1 variants on rASIC1a and hASIC1a

The activity of labelled PcTx1 variants were assessed on both rASIC1a and hASIC1a using TEVC. Addition of an azide group or imaging moieties ranging from 31 Da (terminal azide group) to ~2.3 kDa (4xDOTA-Gd), resulted in a slight reduction in potency (< 7 fold) on both human and rat ASIC1a (Fig. 4.7). The largest effect was observed for the fluorescently-labelled PcTx1 (AF488_azPcTx1 and CF680R_azPcTx1)

and the 4x-Gd-DOTA-azPcTx1 where there was ~7-fold decrease in the inhibitory activity.

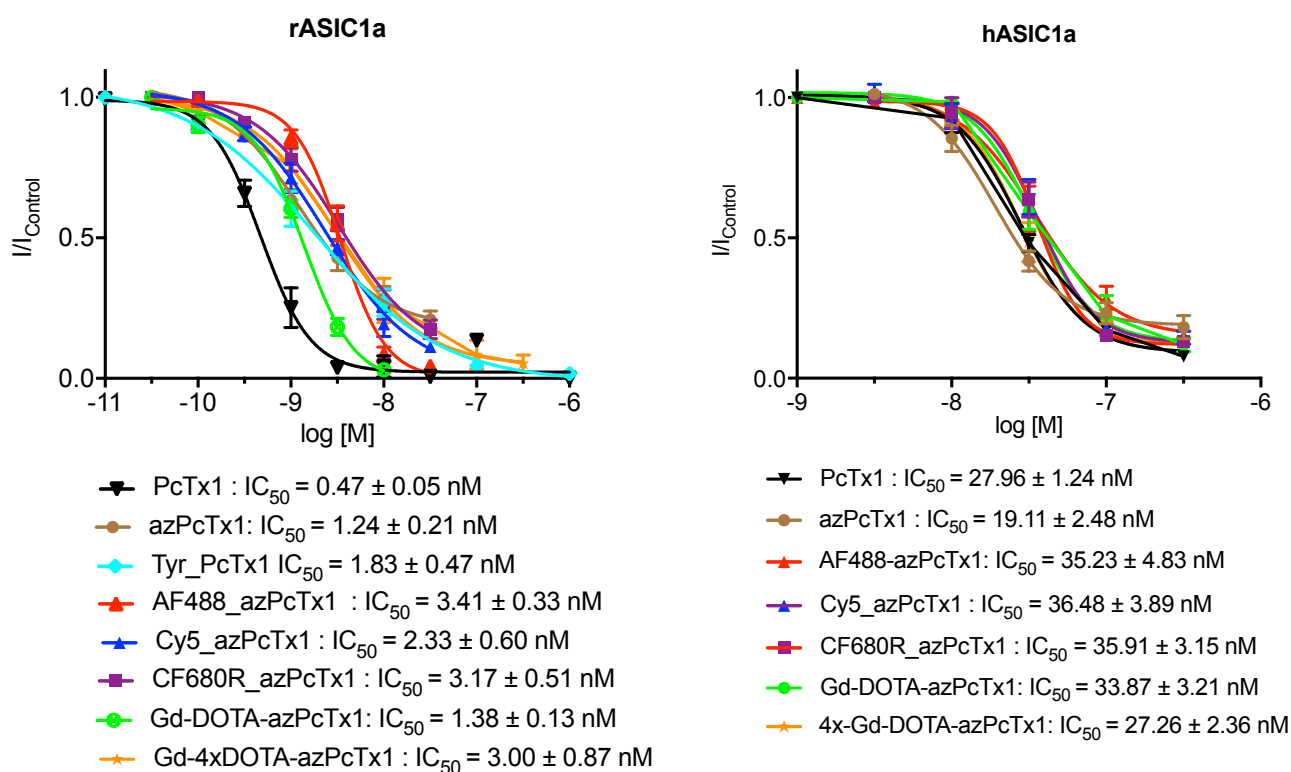


Figure 4.7. Concentration-effect curves for inhibition of rASIC1a (**top panel**) and hASIC1a (**bottom panel**) by various PcTx1 analogues. Data points are mean ± SEM; $n = 4-6$.

4.3.7 Stability profile of PcTx1

PcTx1 was assessed for thermal stability at 55°C (at pH 7.4), and biological stability in human serum and human CSF as shown in **Fig. 3.6 of Chapter 3**.

4.3.8 Interaction between PcTx1 and serum albumin

We used isothermal calorimetry (ITC) and NMR chemical shift mapping (NMR-CSM) to determine whether PcTx1 interacts with serum albumin. ITC revealed a clear interaction between PcTx1 and bovine serum albumin (BSA), with the negative deflections in the raw data (**Fig. 4.8, left panel**) indicating that the interaction is exothermic as less energy is required to heat the sample cell. Fitting of a sigmoidal model to the binding isotherm (**Fig. 4.8, right panel**) yielded a dissociation constant (K_d) of 9.96 μ M and a stoichiometry (n) of 0.29, indicating that up to three PcTx1 molecules may bind to a single BSA protein.

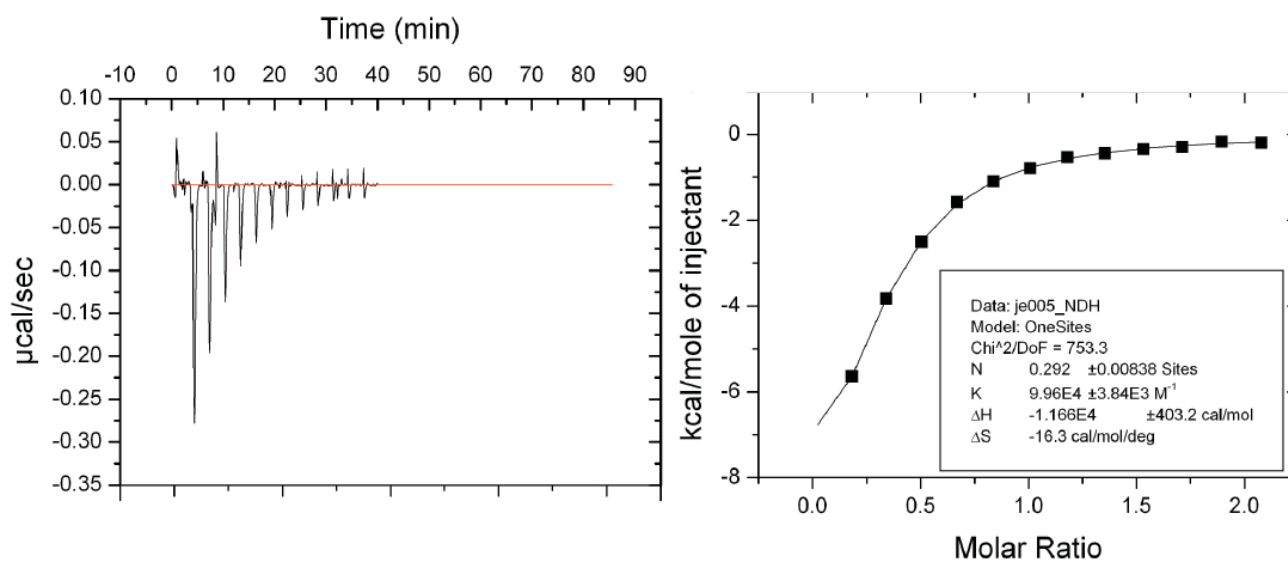


Figure 4.8. Left panel: Raw ITC data showing the exothermic response (negative deflections) obtained when PcTx1 was added to monomeric BSA. **Right panel:** Binding isotherm obtained by integrating the peaks in the left panel and plotting against the molar ratio of PcTx1:BSA. Fitting of sigmoidal curve to the data yielded a K_d of $\sim 9.96 \mu\text{M}$.

NMR-CSM is commonly used to map residues involved in protein-protein interactions. Typically, one protein is ^{15}N -labelled while the interacting partner is unlabelled. Titration of the unlabelled partner into a solution of the ^{15}N -labelled protein leads to an observable perturbation of the NMR chemical shift and/or intensity of residues at the protein-protein interface. Here we titrated BSA into a solution of ^{15}N -labelled PcTx1 and acquired 2D ^1H - ^{15}N HSQC spectra as a function of increasing BSA concentration (**Fig. 4.9**). These HSQC spectra revealed a decrease in intensity for peaks from Trp7, Lys25, Arg26, Arg27, Arg28, Ser29, Val32 upon addition of BSA. The signal decay constant (K) was obtained by fitting a one-phase decay curve to a plot of signal intensity versus BSA concentration, and this is shown as function of residue number in **Fig. 4.10, left panel**. The signals from residues R26, R27 and V32 experienced the highest decay rates. Interestingly, these residues are located in the β -hairpin loop that contains the majority of residues that mediate the interaction of PcTx1 with ASIC1a [add references here to support this statement] (**Fig. 4.10, right panel**).

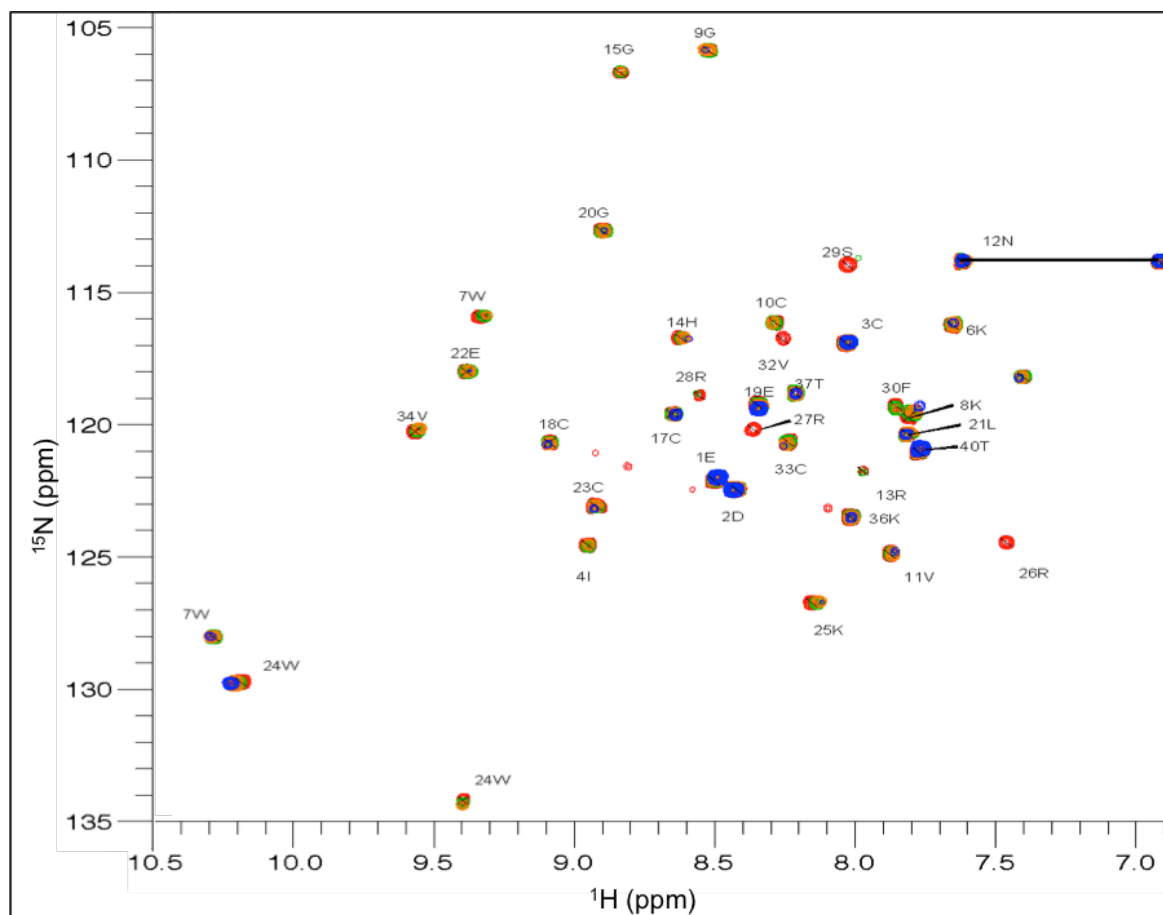


Figure 4.9. Overlay of 2D ^1H - ^{15}N HSQC spectra of 50 μM ^{15}N -labelled PcTx1 in the absence (red) and presence of 25 μM (green), 50 μM (orange) or 150 μM (blue) BSA. Residues R26, R27 and V32 undergo the greatest intensity perturbation as peaks corresponding to these residues became broadened beyond recognition upon addition of 25 μM BSA. (Spectra were collected at the IMB by Dr Carus Lau, who is now at the Victor Chang Cardiac Research Institute, Australia.)

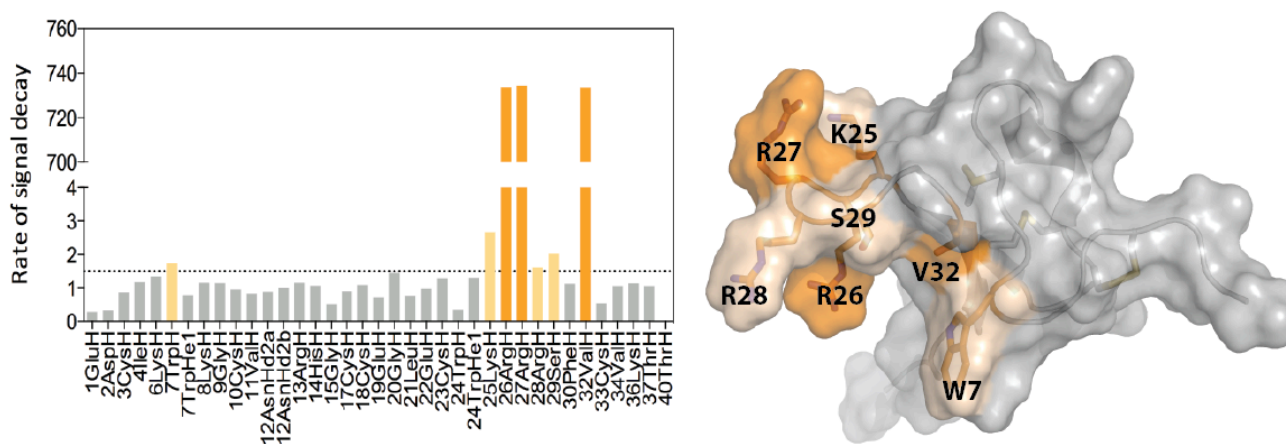


Figure 4.10. **Left panel:** Rate of signal decay (K) as a function of residue position when PcTx1 was titrated with BSA. The greatest diminution in peak intensity was observed for R26, R27 and V32. **Right panel:** Surface representation of PcTx1 (PDB: 2KNI) with residues most affected by the addition of albumin highlighted in orange. NMR CSM experiments were performed and analysed by Dr Carus Lau.

4.3.9 Radiolabelling of Tyr_NPcTx1

Tyr_NPcTx1 (~200 µg of peptide) was labelled with ¹²⁴I using iodogen tubes. The radiochemical purity (RCP) of the product was >96% as indicated using both thin layer chromatography (TLC) (**Fig. 4.11, left panel**) and RP-HPLC (**Fig. 4.11, right panel**). The final radiolabelled product, ¹²⁴I-PcTx1, was reconstituted in phosphate-buffered saline (PBS) to a final concentration of 0.5 µg/µL. The iodination was highly efficient and resulted in mainly mono-iodinated product as indicated by the single peak obtained in the RP-HPLC chromatogram (**Fig. 4.11, right panel**).

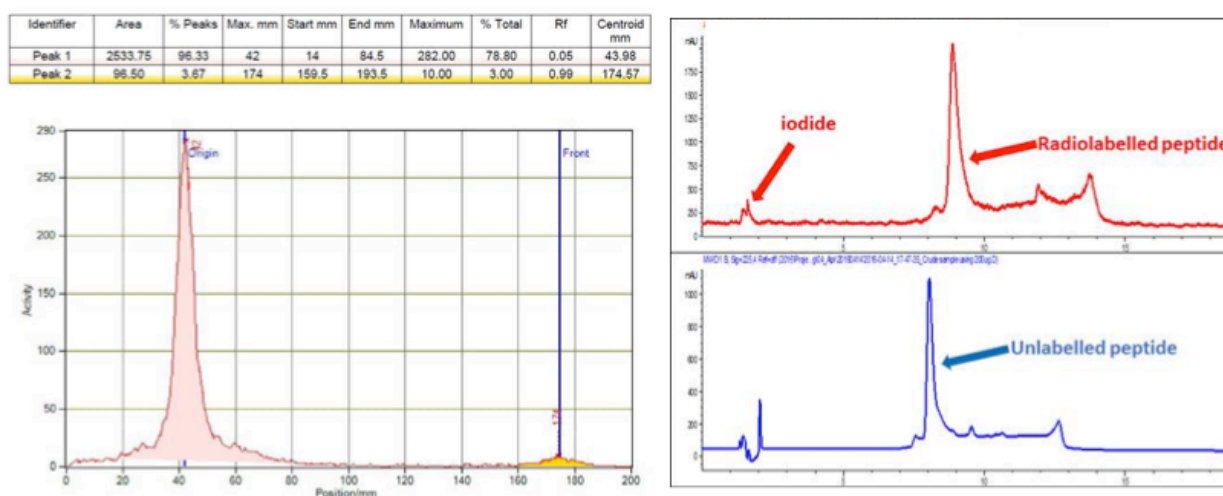


Figure 4.11. Labelling efficiency and radiochemical purity of iodinated Tyr_NPcTx1. **Left:** TLC trace of crude product after iodination. **Right:** RP-HPLC chromatograms of iodinated (red) and non-iodinated (blue) Tyr_NPcTx1 eluted over a gradient of 15–35% Solvent B (90% CH₃CN/0.01% TFA in water) in 20 min (Radioiodination, HPLC and data acquisition were performed by Dr Rajiv Bhalla, Centre for Advanced Imaging, University of Queensland, Australia.)

4.3.10 Pharmacokinetics of ¹²⁴I-PcTx1 after intravenous administration

The uptake of intravenously administered ¹²⁴I-PcTx1 (1.6–2.1 MBq, ~9–25 µg) was monitored using PET/CT imaging (**Fig. 4.12A**). Radioactivity in various organs was measured and calculated over a time course of 90 min to obtain time–activity curves (TACs) (**Fig. 4.12B**). A biodistribution study of ¹²⁴I-PcTx1 was also performed in various organs at different time points after intravenous injection (IV) of the radiotracer. Data is shown in **Fig. 4.12C**.

The dynamic PET imaging (**Fig. 4.12B**) revealed a brief initial peak (0–1.75 min) of ¹²⁴I-PcTx1 in the heart and liver, as expected from a transient increase in blood-pool activity

following IV administration. A peak uptake of 9.9 %ID/g was observed in the heart (surrogate for blood concentration) at 1.75 min after administration which then declined rapidly to ~50% after 6.5 min. The concentration subsequently remained largely unchanged at ~3.5 %ID/g for up to 90 min. Similarly, a rapid increase in ^{124}I -PcTx1 concentration (6.2 %ID/g) was observed in the liver at 1.75 min which then gradually increased to 8.9%ID/g over 90 min. A large proportion of the ^{124}I -PcTx1 accumulated in the kidneys, increasing from 6.8 %ID/g at 1.75 min to 16.8 %ID/g at 27.5 min, then slowly decreased to 11.2 %ID/g at 87.5 min. Increasing uptake was also observed in the thyroid (2.3–5.7 %ID/g) from 1.75–8.75 min. There was also increasing accumulation of ^{124}I -PcTx1 in the bladder over the 90 min time course. The low observed uptake (0.7 %ID/g) in the brain indicates that the peptide is unlikely to cross the BBB in any appreciable amount.

The uptake of ^{124}I -PcTx1 in different organs at different time points after injection of the radiotracer was assessed using PET is shown in **Fig. 4.12C**. The uptake of ^{124}I -PcTx1 in the heart remained largely consistent from 15–240 min. Similarly, liver uptakes were consistent between 15–120 min, followed by a rapid decline from 120–240 min. In the kidneys, there was a high initial accumulation followed by a gradual decline. In agreement with this observation, there was also a gradual accumulation of radioactivity in the bladder which increased over time, indicating that the peptide is eliminated via renal clearance. Low uptake in the brain was observed across all time points, further highlighting that ^{124}I -PcTx1 is unlikely to cross the BBB. Accumulation of ^{124}I -PcTx1 was also observed in the thyroid and stomach. However, this is likely a result of dehalogenation and iodide sequestration in these organs and not peptide uptake.

The results obtained from the PET imaging data were supported by *ex vivo* biodistribution studies using gamma counting of the dissected tissues. As summarised in **Figure 4.12D**, the average uptakes (90 min, 120 min, 150 min, 240 min and 270 min) in various tissues were largely consistent, in the blood (4.1 ± 0.5 %ID/g), heart (1.7 ± 0.3 %ID/g), lungs (3.6 ± 0.8 %ID/g), spleen (2.2 ± 0.7 %ID/g) and brain (0.18 ± 0.04 %ID/g). The high amount of ^{124}I -PcTx1 measured in the kidneys indicates that renal clearance is the main route of elimination of the radiotracer.

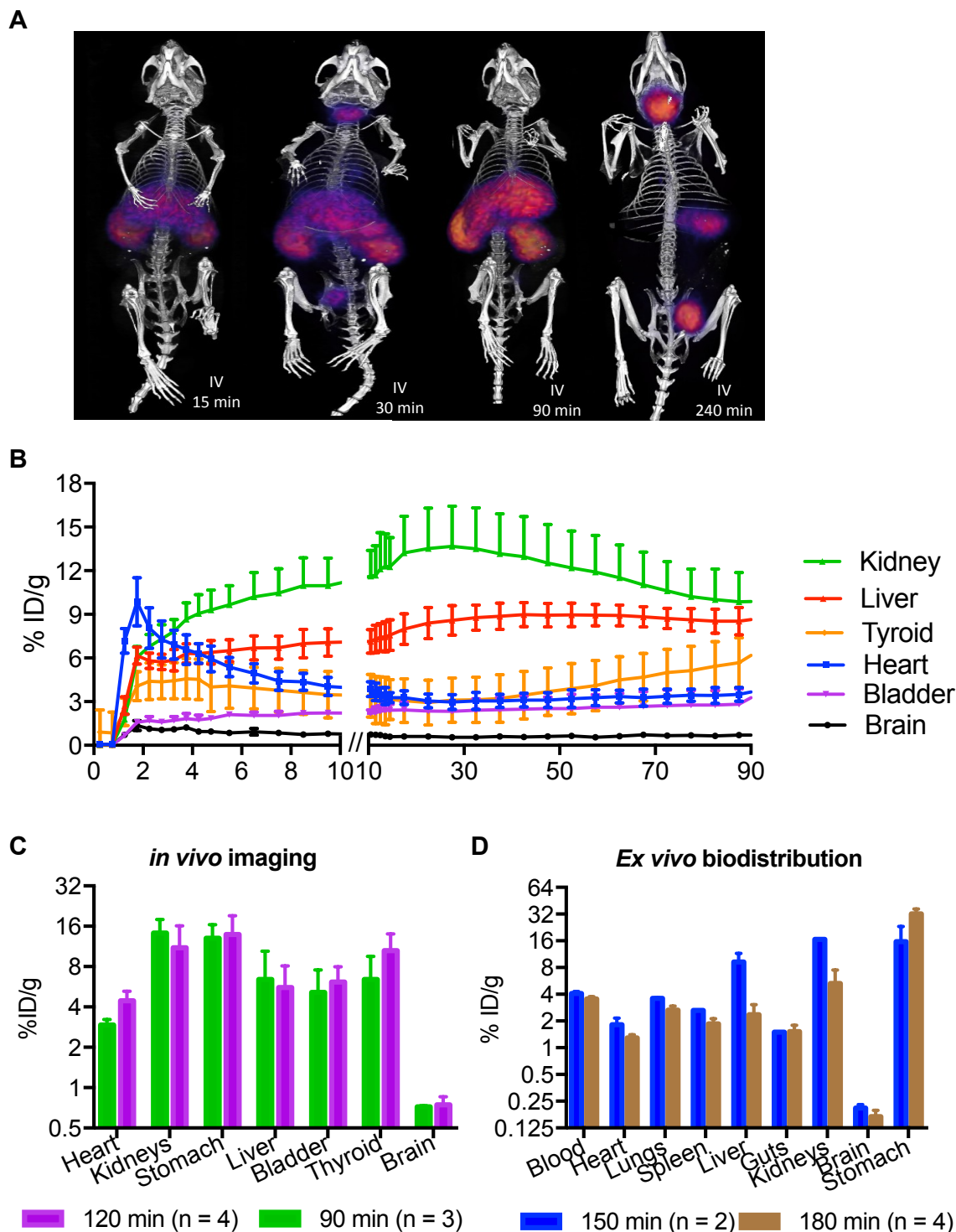


Figure 4.12 Pharmacokinetics of ^{124}I -PcTx1 following IV administration. **(A)** Representative whole-body PET/CT images of *C57BL6* mice showing peptide distribution after IV administration at various time points. **(B)** Time-activity curves (TACs) of ^{124}I -PcTx1 in various tissues over 90 min. **(C)** The *in vivo* distribution of ^{124}I -PcTx1 assessed using PET/CT imaging (paired t-test, $p = 0.5824$, n.s.). **(D)** *Ex vivo* biodistribution of ^{124}I -PcTx1 determined using gamma counting of dissected tissues (paired t-test, $p = 0.8460$, n.s.). Data for PET/CT images are measured using ROI-based analysis in mice. All uptake values are expressed as %ID/g. (Data are mean \pm S.D., $n = 1$ –4). PET/CT images, time activity curves and biodistribution studies were performed by Dr Karine Mardon.

4.3.11 Pharmacokinetics of ^{124}I -PcTx1 after IN administration

We studied the pharmacokinetics of intranasally administered ^{124}I -PcTx1 (~0.3 MBq, ~5 μg) using PET imaging (**Fig. 4.13A,B**) and biodistribution at 30 min, 110 min and 220 min after injection of the radiotracer (**Fig. 4.13C,D**). Static PET images were taken 90 min and 180 min after administration (**Fig. 4.13A**). There was no significant difference in the biodistribution at 90 min or 180 min post intranasal administration ($p = 0.3335$, n.s.). The majority of the peptide appears to be still in the nasal cavity at 90 min (133.5 %ID/g) and 180 min (~30.48 %ID/g) post-injection of ^{124}I -PcTx1. Systemic uptake is evident as indicated by radioactivity in the whole body, heart and lungs. Interestingly, CNS uptake was also observed with ~2.8 and ~1.9 %ID/g in the brain at 90 min and 180 min, respectively. Similar to IV administration of ^{124}I -PcTx1, renal clearance is likely the main route of elimination as indicated by accumulation of peptide in the bladder at 90 min (16.0 %ID/g) and 180 min (44.8 %ID/g) (**Fig. 4.13B**).

The results from static PET imaging were supported by the data obtained with the in vivo biodistribution studies of ^{124}I -PcTx1 at 30 min, 110 min and 220 min post IN administration (**Fig. 4.13C,D**). Similarly, there was no significant difference in the distribution of ^{124}I -PcTx1 in various organs over time ($p = 0.4091$, n.s.). A large proportion of the peptide remained in the nasal cavity as indicated by the high radioactivity at 30 min, 110 min and 220 min, with an average %ID/g of 14.8 ± 7.0 . In good agreement with PET imaging, systemic exposure of ^{124}I -PcTx1 is evident based on the average uptake over time (30, 110 and 220 min) in the blood (2.7 ± 0.2 %ID/g) and peripheral organs including the heart (1.3 ± 0.3 %ID/g), lungs (1.6 ± 0.4 %ID/g), spleen (1.6 ± 0.9 %ID/g), liver (0.9 ± 0.2 %ID/g), gastrointestinal tract (guts) (3.1 ± 1.0 %ID/g), and muscle (0.9 ± 0.6 %ID/g) (**Fig. 4.13C**). The brain was further dissected to characterise the distribution of peptide within the brain (**Fig. 4.13D**). There was no significant difference in the distribution of ^{124}I -PcTx1 in different regions of the brain over time ($p = 0.2522$, n.s.). In comparison to IV, higher brain uptake was observed following IN with the highest concentrations found in the olfactory bulb in all three groups (1.12 ± 0.66 %ID/g). Radioactivity was also detected in other parts of the brain including the medulla/pons, cerebellum, frontal cortex, and posterior cortex; however, the uptake values for these brain regions were similar to the level of whole-brain uptake observed with IV administration.

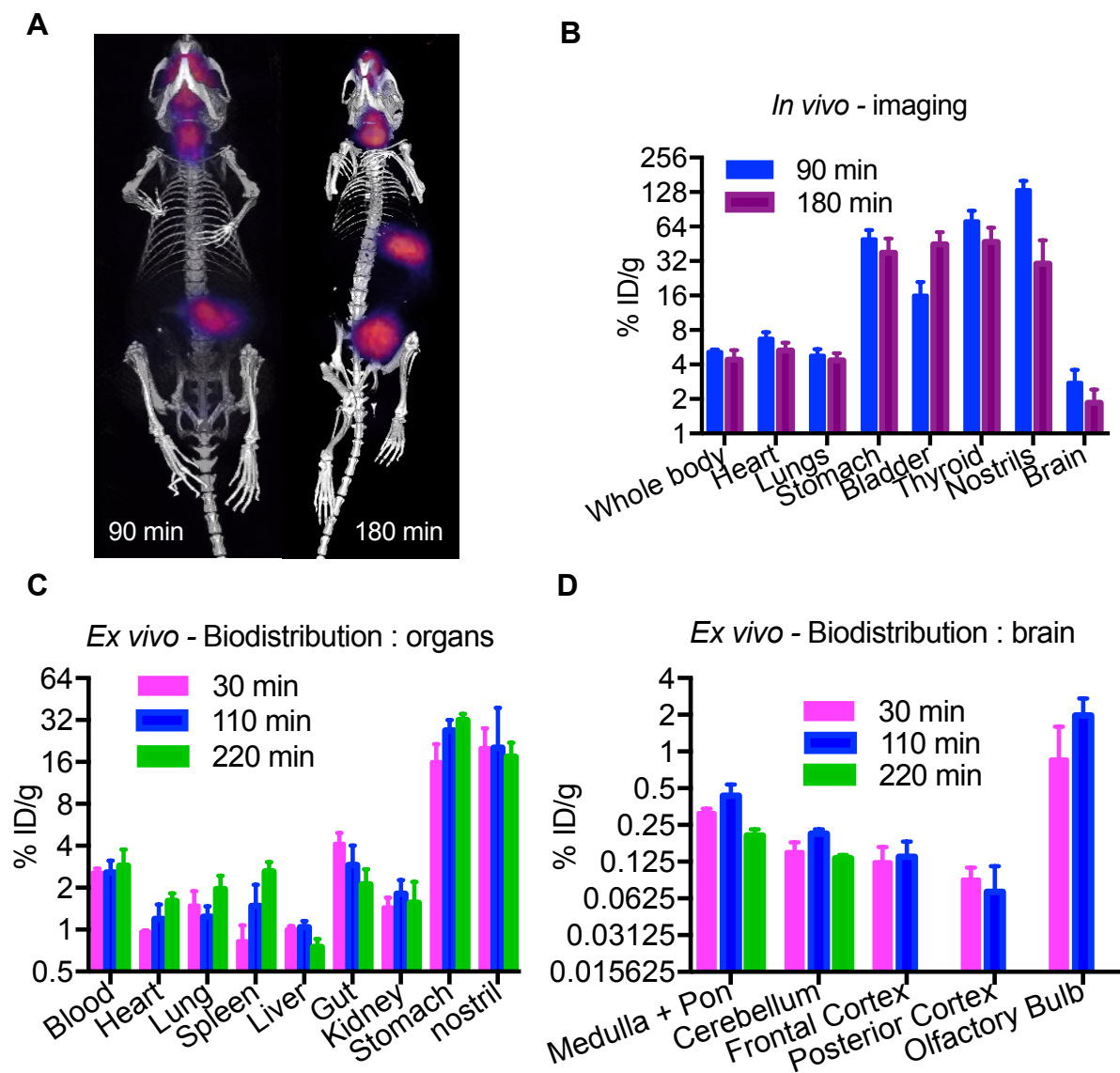


Figure 4.13. Uptake (%ID/g) of ^{124}I -PcTx1 after IN administration. (A) Example PET/CT image of mice at 90 min and 180 min post IN administration of ^{124}I -PcTx1. (B) *In vivo* PET imaging data at 90 min and 180 min after IN administration. Measurements were obtained using ROI-based analysis of PET data sets in mice (paired t-test, $p = 0.3335$, n.s.). *Ex vivo* biodistribution data of (C) organs (one-way ANOVA, $p = 0.4091$, n.s.) and (D) brain section (one-way ANOVA, $p = 0.2522$, n.s.) at 30 min, 110 min, 220 min after injection. All uptake values are expressed as % ID/g. Data are mean \pm S.D., $n = 3-4$. PET/CT images, time activity curves and biodistribution studies were performed by Dr Karine Mardon.

4.4 Discussion

4.4.1 Production and characterisation of labelled PcTx1 variants for PET, MRI and fluorescence imaging

In the present study, variants of PcTx1 labelled with different imaging moieties were produced and characterised. These peptides were produced to facilitate pharmacokinetic and biodistribution studies of PcTx1 as a model SVP. Labelled PcTx1 variants were obtained through two main approaches: recombinant production of a tyrosine-containing mutant for iodination, and chemical synthesis of an azide-functionalised mutant (azPcTx1) for bioconjugation with different alkyne-functionalised imaging moieties. These labelled peptides were made for complementary PET, MR and fluorescence imaging to enable visualisation of the peptide *in vivo*.

PET has unrivalled sensitivity (at pM range) compared to other imaging modalities (μM to mM range), thus making it a method of choice for molecular imaging in drug development studies. In a typical PET study, the compound (in this case, Tyr_N_PcTx1) is labelled with a PET tracer (radioisotope) for visualisation. Due to the uncertainty in the pharmacokinetic properties of PcTx1 (*i.e.* clearance rates), ¹²⁴I was chosen as the tracer due to its relatively long half-life of ~4.2 days, thereby allowing an extended period of study, if needed. In comparison, the half-life of ¹⁸F (another common PET tracer) is ~110 min, restricting the length of the study to only several hours²⁵². Moreover, ¹²⁴I-labelled peptides can be produced through iodination of tyrosine (and to a lesser extent, histidine) without the need for modification with large functional groups that might have affect the peptide's physicochemical properties.

Iodination of tyrosine residue is a commonly used method for radiolabelling peptides or proteins²⁵¹. Although PcTx1 contains a histidine residue that could potentially be iodinated, the reaction is 30–100 times slower than with tyrosine, requiring harsher conditions, longer reaction times, and excessive iodine²⁵³. Due to the lack of tyrosine in the sequence of PcTx1, a variant containing a non-native tyrosine was produced, based on the success of this approach for radioligand binding assays where the authors demonstrated that incorporating a tyrosine residue at either N- or C-terminus and iodination of PcTx1 had minimal effects on its ability to inhibit ASIC1a¹⁰⁸. Moreover, our

lab has conducted extensive structure-activity relationship studies showing that the N-terminal region of PcTx1 is not involved in its interaction with ASIC1a^{104, 110}.

The potency of Tyr_NPcTx1 was assessed using TEVC on *X. laevis* oocytes expressing rASIC1a. Tyr_NPcTx1 was slightly less potent than WT PcTx1 on rASIC1a. The decline in potency was more pronounced for iodinated variants of the peptide (3–8 fold decrease), suggesting that additions to the N-terminus may affect peptide activity, contrary to co-crystal structures and MD studies showing that the N-terminus points away from the channel, and does not engage in channel interactions¹⁰⁴. Moreover, electrophysiology experiments of other labelled PcTx1 variants with bulkier additions at the N-terminus were more potent than iodinated Tyr_NPcTx1. Given these observations, it is possible that the stock concentration of the iodinated variants might have been overestimated based on UV absorbance. In support of this presumption, a positive correlation was observed in the absorptivity of tyrosine (at 280 nm) with increasing iodination²⁵⁴. This may have contributed to the erroneous quantification of the iodinated Tyr_NPcTx1, thereby resulting in the subsequent underestimation of peptide activity. Nevertheless the iodinated Tyr_NPcTx1 still potently inhibited ASIC1a, with an IC₅₀ in the low nanomolar range.

azPcTx1 was synthesised for site-specific N-terminal labelling with alternative imaging moieties via click chemistry. The triazole formed between an azide and alkyne is irreversible and chemically inert to reactive conditions (e.g. oxidation, reduction, and hydrolysis) thus ensuring the stability of the complex in an *in vivo* environment. As verified using mass spectrometry and TEVC, the various alkyne-activated imaging moieties (up to 2.3 kDa) were successfully attached to the azPcTx1 via CuAAC or SPAAC with minimal effects on its ASIC1a inhibitory activity. Electrophysiology experiments performed on both rASIC1a and hASIC1a showed that all variants inhibited ASIC1a with low nanomolar potency.

As an alternative to radioiodination, DOTA-conjugated variants of PcTx1 were produced to facilitate chelation of radiometals as PET tracers or lanthanides for magnetic resonance imaging. DOTA consists of a macrocyclic ring structure that functions as an octadentate ligand for chelating metal ions (especially lanthanide ions, Ln³⁺) through its four amine and carboxylate groups forming highly stable complexes with extraordinary

thermodynamic stability and kinetic inertness²⁵⁵. Peptide-DOTA complexes are commonly used in magnetic resonance imaging (gadolinium), nuclear imaging (indium-111, gallium-68, copper-64/67), and as therapeutic radiopharmaceuticals (yttrium-90, lutetium-177)²⁵⁵. In an attempt to improve the sensitivity of PET or MR imaging, two azide-reactive DOTA tags were synthesised which could coordinate either one or four metal ions. The syntheses were achieved with high yield and purity. The DOTA tags were shown to coordinate one (Gd-DOTA) or four (4x-Gd-DOTA) gadolinium ions respectively, as verified using mass spectrometry.

MRI was also explored as a potential complement to PET imaging, as it provides greater spatial resolution. Contrast in MRI is largely generated based on differences in proton (mainly water) relaxation. Gadolinium complexes are clinically used to enhance contrast in T_1 -weighted MRI by altering ^1H relaxation properties, causing regions with higher concentration of the gadolinium complex to appear brighter. We hypothesised that the interaction with DOTA-Gd-azPcTx1 conjugates may also induce changes in relaxation properties in regions with higher peptide concentration, particularly in areas with high ASIC1a expression (e.g. brain), thus providing information regarding peptide uptake, localisation, as well as the distribution/relative expression levels of ASIC1a. There was an overall marked enhancement in r_1 and r_2 relativity of the DOTA-Gd-azPcTx1 complexes as compared to azPcTx1. Moreover, the metallated PcTx1-DOTA complexes have higher r_1 values ($4.6\text{--}9.4\text{ mM}^{-1}\text{s}^{-1}$) than clinically used MRI T_1 contrast agents such as DOTAREM[®] (Gadoterate meglumine, Gd-DOTA, r_1 of $3.9\text{ mM}^{-1}\text{s}^{-1}$), and Magnevist[®] (Gadopentetate Dimeglumine, Gd-DPTA [diethylenetriaminepentaacetic acid], r_1 of $4.1\text{ mM}^{-1}\text{s}^{-1}$ at 9.4 T)²⁵⁶. However, the inherently low sensitivity of MRI (requiring high μM to mM concentrations for contrast), made the use of MR imaging for pharmacokinetics and biodistribution study impractical at this stage due to the high quantities of peptide conjugates necessary for statistical significance.

4.4.2 Stability of PcTx1

Assessment of thermal and metabolic stability is imperative prior to radiolabelling and *in vivo* experiments. As such, PcTx1 was incubated at high temperature (55°C) and in human serum or CSF to establish its stability profile under these conditions (**Chapter 3**). Oxytocin, a nonapeptide containing a single disulfide bond, was used as a comparison

as it is known to be relatively heat labile²⁵⁷. The thermal stability observed for oxytocin at 55°C (~40% remaining at 48 h) was in good agreement with published data²⁵⁸.

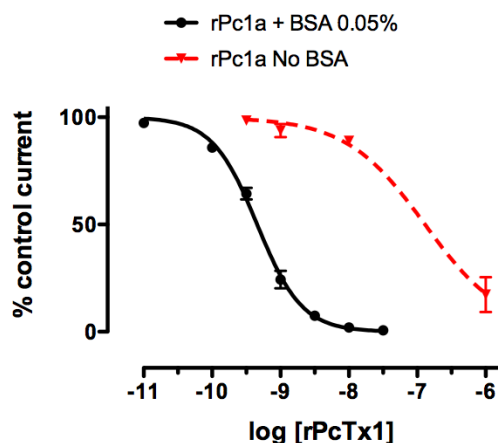
The ICK scaffold is regularly claimed to provide high thermal stability and resistance to proteolytic degradation^{10, 13} and this has been demonstrated for several spider-venom ICK peptides^{12, 259}. Surprisingly, PcTx1 was less stable than expected. A plausible explanation could be the highly dynamic and cationic nature of the β -hairpin loop of PcTx1¹⁰⁴, which might enhance susceptibility to serum and CSF proteases. Curiously, Hm3a (a close homolog of PcTx1, described in Chapter 3), was more stable than PcTx1, with ~90% peptide intact after 48 h at 55°C. Based on sequence homology, it can be presumed that Hm3a has similar structural features such as the flexible β -hairpin loop. Thus, there may be other factors accounting for the differences in thermal stability. From an inspection of the amino acid sequences, a possible degradation-contributing site could be Asp2 of PcTx1, which is replaced by a proline in Hm3a. Aspartate is highly susceptible to isomerisation, forming intermediates such as isoaspartate (β -Asp). In support of this hypothesis, degradation products containing β -Asp were observed following incubation of the growth hormone–releasing hormone (GHRH) at 55°C in acidic solution²⁶⁰. Thus, at high temperature, the accelerated isomerisation of Asp2 in PcTx1 could result in the formation of side products, accounting for the loss of native peptide as observed on RP-HPLC.

Metabolic stability is an important factor that affects a peptide's efficacy *in vivo* as there are a multitude of proteases and peptidases in plasma that could lead to degradation of the peptide²⁶¹. Compared to thermal stress, PcTx1 was more resistant to metabolic degradation when incubated in human serum and CSF, with >76% of peptide remaining intact even after 48 h. Thus, it can be safely predicted that PcTx1 would remain largely intact throughout the course of the imaging study.

4.4.3 Interaction with serum albumin

It is common practice in *in vitro* functional studies to include some kind of protein in the physiological saline solutions in order to minimise adsorptive losses of peptide to plastic surfaces. Indeed, when PcTx1 is assayed using TEVC, the presence or absence of BSA has a dramatic effect on inhibition of rASIC1a at pH 7.45 (**Supp. Fig. 4.1**). In the context of understanding the pharmacokinetics of a drug lead, serum binding is an

important factor. Thus we characterised the interaction of PcTx1 with BSA using two techniques.



Supplementary Figure. 4.1. Influence of BSA on PcTx1 inhibition of rASIC1a when tested at pH 7.45 ($p < 0.001$, $F = 28.85$).

Serum albumin (66.5 kDa) is a monomeric, globular protein that is synthesised in the liver. It constitutes about 50% of serum proteins (35–50 g/L) and has an average serum half-life of ~19 days. Serum albumin is a multifunctional protein that is involved in the maintenance of oncotic pressure (type of osmotic pressure contributed by proteins), plasma pH, and transport of hydrophobic molecules such as hormones and fatty acids. Albumin is able to bind a wide variety of molecules via interactions with many different amino acid side chains²⁶². Hence, it also binds to numerous drugs and metal ions and can act as a depot and transport vehicle for these molecules in the blood. Thus, albumin binding can be an important determinant of the pharmacokinetics of a drug as it influences the amount of “free” molecule that reaches its intended target²⁶³. It also has implications for the clearance of a drug from the blood²⁶⁴. In rats, IV administered analogs of the 39-residue anti-diabetic drug exenatide that contain albumin-binding domains (K_d of 8.2–18.3 nM for rat albumin) have extended plasma half-lives of 11–16 h as compared to 30 min for the wild-type peptide drug²⁶⁴.

ITC experiments indicated that PcTx1 binds to BSA with a K_d of 9.96 μ M. The interaction site on PcTx1 was mapped using NMR-CSM, which showed a massive diminution in the peak intensity of resonances from Arg26, Arg27 and Val32 with increasing BSA concentration. Changes in peak intensity, as opposed to chemical shift

perturbations, are typical for interactions with moderate affinity (μM range)²⁶⁵, which is consistent with the ITC results. Curiously, these residues are part of the pharmacophore of PcTx1 involved in its interaction with ASIC1a (**Fig. 4.14**). However, as PcTx1 binds to ASIC1a with low nanomolar affinity ($K_d \sim 0.20\text{--}0.37 \text{ nM}$)¹⁰⁸, the interaction between PcTx1 and BSA is unlikely to affect its intrinsic activity on the channel, as seen in TEVC experiments. However, the interaction of PcTx1 with serum albumin may improve its pharmacokinetic properties by extending its plasma half-life, reducing glomerular filtration and renal clearance²⁶³.

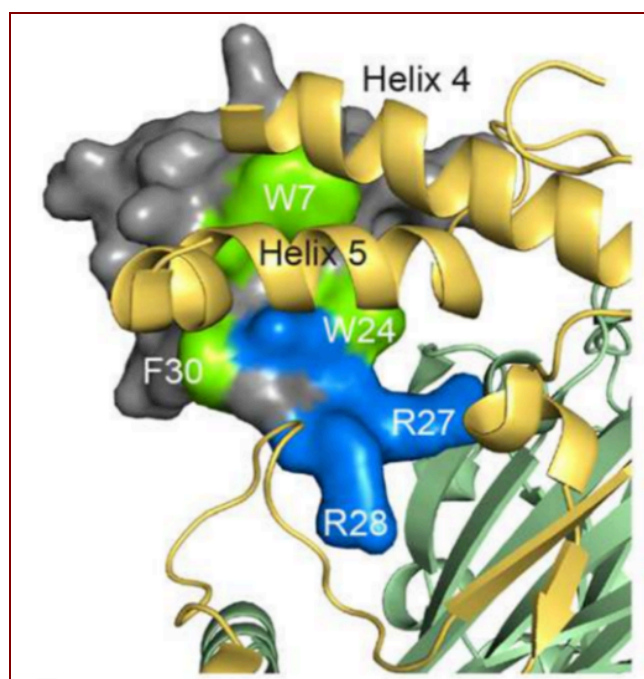


Figure 4.14. Interaction between residues of the PcTx1 pharmacophore ((W7, W24, R26, R27 and F30) and Helix 5 of cASIC1 (figure from Saez *et. al.*, 2015¹¹⁰).

4.4.5 Pharmacokinetics of PcTx1

A combined PET imaging and conventional *ex vivo* tissue sampling approach was undertaken to compare the pharmacokinetics and biodistribution of PcTx1 after IV and IN administration. Following IV administration, PcTx1 was largely eliminated through glomerular filtration based on the observed accumulation of peptide in the kidney and bladder. High radioactivity was also observed in the stomach, liver and thyroid. However, this is likely due to the dehalogenation and the high expression of the sodium-iodide symporter (NIS) in these organs, resulting in the sequestration and accumulation of ¹²⁴I (Ref. ²⁶⁶⁻²⁶⁷). The interaction between PcTx1 and serum albumin, as we observed

using ITC and NMR-CSM, may have contributed to its relatively long blood half-life (3.54 ± 0.22 %ID/g) and kidney half-life (5.28 ± 2.21 %ID/g). IV administration of PcTx1, even at a high dose of ~ 0.5 mg/kg, caused no obvious adverse side-effects (e.g., no sedation, paralysis or neurological symptoms), indicating that the peptide is likely to be well-tolerated with minimal toxicity issues. However, an important observation relevant to development of PcTx1 as a neuroprotective agent was that the peptide did not cross the BBB following IV administration, at least in healthy animals.

IN administration of PcTx1 resulted in higher uptake in the brain as compared to IV administration.. The highest concentration of ^{124}I -PcTx1 was found in the olfactory bulb, medulla and pons, corresponding to the entry points for the olfactory and trigeminal nerves, respectively. This indicates that the peptide is likely to travel along the olfactory and trigeminal nerve pathways to the brain following IN administration as previously discussed in **Section 1.18** and illustrated in **Figs 1.6 and 1.7**. Although the level of brain uptake was quite low, the high potency of PcTx1 and its lack of systemic toxicity suggests that IN administration is a promising strategy for disorders in which brain ASIC1a is implicated, such as ischemic stroke. However, it remains to be determined whether IN administration of PcTx1 would provide sufficient peptide to the infarcted partial region of the brain to be therapeutically useful after stroke. Future imaging and biodistribution studies will be helpful in dissecting the uptake of IN administered PcTx1 after ischemic stroke in which the BBB is also known compromised¹⁷⁶.

Based on the highest average uptake observed in the olfactory bulb (2.885 %ID/g or 0.026 %ID/organ) with 5 μg of peptide administered via IN, the amount of the PcTx1 in the olfactory bulb will be ~ 1.3 ng. McCarthy *et al.* found that a single dose of PcTx1 at 1 ng/kg administered ICV at 2 h post-stroke reduced brain infarct size in rats by $\sim 70\%$ ¹⁴²; this roughly equates to 30 pg of PcTx1 needed for a 30 g mouse to achieve similar results. Hence, IN administration of 5 μg of peptide would be more than sufficient to induce similar therapeutic effects. Curiously, IN administration of crude “PcTx1 venom” was shown to elicit $\sim 50\%$ reduction in infarct size when given to mice at 1–4 h post stroke¹⁴¹. In this latter study, 25 ng of “PcTx1 venom” was administered intranasally in mice¹⁴¹. Given that PcTx1 constitutes $\sim 0.4\%$ of venom¹⁴², the amount of PcTx1 administered via IN (based on our results) would be ~ 0.1 ng, equating to ~ 0.026 pg of peptide in the olfactory bulb, considerably less than the amount

administered via ICV. This indicates that the neuroprotective effect observed by Pignataro *et al.*¹⁴¹ was more likely due to a combined effect from other unknown components in the venom and not PcTx1 alone.

Intranasal administration is a promising method for CNS drug delivery of peptidic molecules such as PcTx1. However, adsorption across the nasal epithelium is a major caveat for IN, severely limiting the uptake of drugs to the target site. Based on this study, only a small percentage (maximum of 2.83 %ID/g) was able to reach the target whilst most of the peptide remained in the nasal cavity even after extended periods of time (up to 220 min). There are numerous limiting factors that can influence nasal absorption. These include the presence of nasal mucociliary clearance mechanisms, metabolising enzymes, efflux transporters, and reduced availability due to absorption in to the circulation instead of the nasal epithelium²⁶⁸. In order to improve the low absorptivity across the nasal epithelium, several formulation strategies have been assessed (**Table 4.5**)²⁶⁸. Such formulation strategies could be explored to improve uptake of PcTx1 (and other peptidic drug leads) to the CNS following IN administration.

Table 4.4. Formulation strategies for improving absorption across the nasal epithelium²⁶⁸.

Strategy	Mechanism
Nasal permeation enhancers <ul style="list-style-type: none"> • cyclodextrin • fusidic acid derivatives • Phosphatidylcholines • microspheres and liposomes • bile salts and surfactants 	<ul style="list-style-type: none"> • Increase in the membrane fluidity • Create transient hydrophilic pores, decreasing the viscosity of mucous layer • Opening of tight junctions in the epithelium
Mucoadhesive <ul style="list-style-type: none"> • Mucoadhesive polymers (e.g. polyacrylic acid, carbopol, and carboxymethylcellulose) • Mucoadhesive gel formulation 	<ul style="list-style-type: none"> • Enhances the nasal residence time of the drug molecule and hence enhances absorption and bioavailability
Enzyme inhibitors <ul style="list-style-type: none"> • Various peptidase and protease inhibitors 	<ul style="list-style-type: none"> • Increase bioavailability of drug by reducing enzymatic degradation
Particulate drug delivery system <ul style="list-style-type: none"> • Microspheres, nanoparticles, and liposome 	<ul style="list-style-type: none"> • Formulation with nasal permeation enhancers or mucoadhesion to enhance uptake and/or bioavailability

4.5 Conclusion

This chapter described the development, production and characterisation of PcTx1 variants with attached imaging moieties for complementary pharmacokinetics and biodistribution studies using advanced imaging techniques such as PET, NIRF and MRI. An azPcTx1 analog was synthesised and ligated with various imaging moieties via click chemistry methods. A recombinant Tyr_N-PcTx1 analog was successfully produced and radioiodinated. Based on TEVC characterisation of the PcTx1 variants, the various N-terminal modifications had minimal effect on the intrinsic activity of PcTx1 on both rat and human ASIC1a. PcTx1 is moderately stable at high temperature, and in human serum and human CSF. PcTx1 also interacts with serum albumin with moderate affinity as demonstrated using ITC and NMR-CSM.

We studied the pharmacokinetics and biodistribution of ¹²⁴I-PcTx1 following IV and IN administration using PET/CT imaging. Rapid renal clearance, typical for small peptides, was observed following IV administration with the highest PET signal coming from the liver, kidneys and bladder. Uptake in the brain was low, as expected due to restricted access across the BBB. Significantly increased brain uptake of PcTx1 was achieved following IN administration as evident from PET/CT imaging and biodistribution studies. Radioactivity from the labelled peptide was observed in multiple parts of the brain, particularly the olfactory bulb and medulla pons, corresponding to the proposed uptake routes associated with the olfactory and trigeminal nerves. Radioactivity was also detected in several other parts of the brain including the frontal cortex, posterior cortex and cerebellum indicating possible wide spread distribution in the brain. Accumulation of the peptide in blood and peripheral organs also suggest systemic uptake.

To the best of our knowledge, this chapter describes the first pharmacokinetic and biodistribution studies undertaken for a spider-venom peptide using a multimodal imaging approach. The information from this study will be valuable for the development of spider venom peptides as therapeutics. In particular, we have shown that IN administration is a plausible method to deliver spider venom peptides into the CNS.

Chapter Five

Final conclusion and future directions

The ultimate aim of this thesis was to characterise spider venom peptides that could be developed as eco-friendly bioinsecticides or as therapeutic leads targeting ASIC1a.

Development of OAIPs as bioinsecticides

OAIP3 is one of five insecticidal peptides that were previously discovered through assay-guided fractionation²⁰⁰. The insecticidal activity observed when the peptides were injected or fed has garnered commercial interest in their development as bioinsecticides. However, only OAIP1 had been characterised thus far; moreover, it was produced via chemical synthesis which is less pragmatic for commercialisation due to its high cost and limited scalability. In this work, I used a bacterial expression system for production of recombinant OAIP3 in sufficient yield and purity for further characterisation of the peptide. Heteronuclear NMR studies revealed that OAIP3 has a canonical ICK fold, which indicates that it is likely to be stable under stressful environmental conditions such as high temperature and the protease-rich gut environment of targeted insect pests. However, recombinant OAIP3 is less potent than WT OAIP3 when injected into mealworms which I attribute to the lack of C-terminal amidation in the recombinant peptide. Hence, production of amidated OAIP3 will be imperative for functional characterisation in future experiments. The peptide should also be tested against different target and non-target insect species from various orders such as Lepidoptera, Diptera and Hymenoptera to determine its phyletic specificity. It is also imperative to study its effect on vertebrates to identify potential toxicity liabilities as this is a major concern for insecticide development.

From a biotechnology standpoint, the need for post-translational modification of a bioactive peptide would grossly increase the complexity and cost of production, rendering the compound less commercially viable. This is especially important for development of field-applied insecticides given the large quantities required. Thus, methods to functionally mimic critical post-translation modifications should be explored, as previously described for mimicry of the C-terminal amidation in μ -TRTX-Hh2a²²⁴, in order to enhance the commercial viability of OAIP3 as a bioinsecticide.

The establishment of an efficient method for production of recombinant OAIPs paves the way for future characterisation of other OAIPs, including deciphering their molecular

target(s). Whilst my initial study indicates that OAIP3 is not a good candidate for insecticide development, OAIP2, OAIP4 and OAIP5 remained to be characterised.

Development of spider venom peptides as therapeutics

Hm3a is a close homolog of PcTx1, sharing similar pharmacological profiles on ASICs and most likely having a very similar 3D structure. Despite these similarities, Hm3a is markedly more stable at high temperature and in the protease-rich environment of human serum. Through analysis of the peptide sequences, we hypothesised that the difference in stability might be due to the Asp to Pro mutation at position 2, removal of lysines, and incorporation of Pro at the C-terminal of Hm3a. Thus, future work should include mutagenesis of the aforementioned residues in PcTx1 to examine their influence on peptide stability. Comparing the structure of Hm3a and PcTx1 will also aid in the development of other therapeutically-relevant peptide analogues to improve their inherent stability.

Despite the immense potential of spider venom peptides as therapeutics, particularly those with an ICK fold, very few studies have been undertaken to elucidate their pharmacokinetics and biodistribution properties. In this work, we used advance imaging and traditional tissue sampling to address this lack of information. In the interest of developing SVPs as therapeutics for stroke or other CNS diseases, we demonstrated a direct nose-to-brain delivery of PcTx1 via IN administration, bypassing the BBB. In contrast, minimal brain uptake was observed following IV administration, indicating that PcTx1 is unable to cross the BBB in healthy mice. The knowledge gained from this study is likely to be applicable to delivery of other venom-derived peptides targeting the CNS.

The high potency of many SVPs make them well suited for IN administration. Although only modest brain uptake was observed following IN administration, an effective dose could be achieved relatively easily given the nanomolar potency of SVPs such as PcTx1. Notably, the majority of the IN-administered peptide remained in the nasal cavity and therefore it should be beneficial to explore formulation strategies designed to improve uptake of molecules across the nasal epithelium.

A major caveat of PET or MR imaging is cost and the need for high technical expertise. Moreover, in the current PET study, high radioactivity was detected in the thyroid and

stomach, which is commonly associated with dehalogenation and sequestration of iodide in these organs, which could confound the biodistribution study. Thus, it will be crucial to determine the metabolic stability of the iodinated or labelled peptides for future experiments. From our study of PcTx1, clearance of peptide was evident within several hours. Thus, short-lived radioisotopes such as ^{18}F instead of ^{124}I might be more suitable for PET imaging of peptides for biodistribution studies.

Overall, this thesis has demonstrated that spider venoms provide a huge source of bioactive peptides with biotechnological potential that could potentially be utilised for the development of novel agrochemical or therapeutic compounds.

References

1. Brodie, E. D., Predator-prey arms races. Asymmetrical selection on predators and prey may be reduced when prey are dangerous. *BioScience* **1999**, *49* (7), 557–568.
2. Escoubas, P.; Sollod, B.; King, G. F., Venom landscapes: mining the complexity of spider venoms via a combined cDNA and mass spectrometric approach. *Toxicon* **2006**, *47* (6), 650–663.
3. Escoubas, P.; Quinton, L.; Nicholson, G. M., Venomics: unravelling the complexity of animal venoms with mass spectrometry. *J Mass Spectrom* **2008**, *43* (3), 279–295.
4. Escoubas, P.; Diochot, S.; Corzo, G., Structure and pharmacology of spider venom neurotoxins. *Biochimie* **2000**, *82* (9–10), 893–907.
5. Dutertre, S.; Lewis, R. J., Use of venom peptides to probe ion channel structure and function. *J Biol Chem* **2010**, *285* (18), 13315–13320.
6. Lewis, R. J.; Garcia, M. L., Therapeutic potential of venom peptides. *Nat Rev Drug Discov* **2003**, *2* (790–802), 790–802.
7. King, G. F., Venoms as a platform for human drugs: translating toxins into therapeutics. *Expert Opin Biol Th* **2011**, *11* (11), 1469–1484.
8. Vetter, I.; Davis, J. L.; Rash, L. D.; Anangi, R.; Mobli, M.; Alewood, P. F.; Lewis, R. J.; King, G. F., Venomics: a new paradigm for natural products-based drug discovery. *Amino Acids* **2011**, *40* (1), 15–28.
9. King, G., Venoms to drugs: Translating venom peptides into therapeutics. *Australian Biochemist* **2013**, *44* (3), 13–16.
10. King, G. F.; Hardy, M. C., Spider-venom peptides: Structure, pharmacology, and potential for control of insect pests. *Annu Rev Entomol* **2013**, *58*, 475–496.
11. Palagi, A.; Koh, J. M. S.; Leblanc, M.; Wilson, D.; Dutertre, S.; King, G. F.; Nicholson, G. M.; Escoubas, P., Unravelling the complex venom landscapes of lethal Australian funnel-web spiders (Hexathelidae: Atracinae) using LC-MALDI-TOF mass spectrometry. *J Proteomics* **2013**, *80*, 292–310.
12. Herzig, V.; King, G. F., The cystine knot is responsible for the exceptional stability of the insecticidal spider toxin ω -Hexatoxin-Hv1a. *Toxins* **2015**, *7*, 4366–4380.
13. Craik, D. J.; Daly, N. L.; Waite, C., The cystine knot motif in toxins and implications for drug design. *Toxicon* **2001**, *39* (1), 43–60.
14. Tilman, D.; Balzer, C.; Hill, J.; Befort, B. L., Global food demand and the sustainable intensification of agriculture. *Proc Natl Acad Sci U S A* **2011**, *108* (50), 20260–20264.
15. Peng, S.; Huang, J.; Sheehy, J. E.; Laza, R. C.; Visperas, R. M.; Zhong, X.; Centeno, G. S.; Khush, G. S.; Cassman, K. G., Rice yields decline with higher night temperature from global warming. *Proc Natl Acad Sci U S A* **2004**, *101* (27), 9971–9975.
16. Porter, J. H.; Parry, M. L.; Carter, T. R., The potential effects of climatic change on agricultural insect pests. *Agr Forest Meteorol* **1991**, *57* (1–3), 221–240.

17. Khasnis, A. A.; Nettleman, M. D., Global warming and infectious disease. *Arch Med Res* **2005**, *36* (6), 689–696.
18. Oerke, E. C., Crop losses to pests. *J Agr Sci* **2006**, *144*, 31–43.
19. Diffenbaugh, N. S.; Krupke, C. H.; White, M. A.; Alexander, C. E., Global warming presents new challenges for maize pest management. *Environ Res Lett* **2008**, *3* (4).
20. Aragón, P.; Lobo, J. M., Predicted effect of climate change on the invasibility and distribution of the Western corn root-worm. *Agric. For. Entomol.* **2011**, *14* (1), 13–18.
21. Tabachnick, W. J., Challenges in predicting climate and environmental effects on vector-borne disease epistemics in a changing world. *J Exp Biol* **2010**, *213* (6), 946–954.
22. Mehlhorn, H.; Al-Rasheid, K. A.; Al-Quraishy, S.; Abdel-Ghaffar, F., Research and increase of expertise in arachno-entomology are urgently needed. *Parasitol Res* **2012**, *110* (1), 259–265.
23. Benelli, G., Research in mosquito control: current challenges for a brighter future. *Parasitol Res* **2015**, *114* (8), 2801–2085.
24. Hemingway, J.; Ranson, H., Insecticide resistance in insect vectors of human disease. *Annu Rev Entomol* **2000**, *45*, 371–391.
25. Ranson, H.; N'Guessan, R.; Lines, J.; Moiroux, N.; Nkuni, Z.; Corbel, V., Pyrethroid resistance in African anopheline mosquitoes: what are the implications for malaria control? *Trends Parasitol* **2011**, *27* (2), 91–98.
26. Pates, H.; Curtis, C., Mosquito behavior and vector control. *Annu Rev Entomol* **2005**, *50*, 53–70.
27. Bass, C.; Field, L. M., Gene amplification and insecticide resistance. *Pest Manag Sci* **2011**, *67* (8), 886–890.
28. Pasteur, N.; Raymond, M., Insecticide resistance genes in mosquitoes: Their mutations, migration, and selection in field population. *J Hered* **1996**, *87* (6), 444–449.
29. Lai, T.; Su, J., Assessment of resistance risk in *Spodoptera exigua* (Hübner) (Lepidoptera: Noctuidae) to chlorantraniliprole. *Pest Manag Sci* **2011**, *67* (11), 1468–1472.
30. Ffrench-Constant, R. H.; Pittendrigh, B.; Vaughan, A.; Anthony, N., Why are there so few resistance-associated mutations in insecticide target genes? *Philos Trans R Soc Lond B Biol Sci* **1998**, *353*, 1685–1693.
31. Williamson, M. S.; Martinez-Torres, D.; Hick, C. A.; Devonshire, A. L., Identification of mutations in the housefly para -type sodium channel gene associated with knockdown resistance (kdr) to pyrethroid insecticides. *Mol Gen Genet* **1996**, *252* (1-2), 51–60.
32. Ffrench-Constant, R. H.; Rocheleau, T. A.; Steichen, J. C.; Chalmers, A. E., A point mutation in a *Drosophila* GABA receptor confers insecticide resistance. *Nature* **1993**, *363* (6428), 449–451.
33. Menozzi, P.; Shi, M. A.; Lougarre, A.; Tang, Z. H.; Fournier, D., Mutations of acetylcholinesterase which confer insecticide resistance in *Drosophila melanogaster* populations. *Bmc Evol Biol* **2004**, *4* (4), 1–7.

34. Hardy, M. C., Resistance is not futile: It shapes insecticide discovery. *Insects* **2014**, *5*, 227-242.
35. Weisenburger, D. D., Human health effects of agrichemical use. *Human Pathology* **1993**, *24* (6), 571–576.
36. Eskenazi, B.; Bradman, A.; Castorina, R., Exposures of children to organophosphate pesticides and their potential adverse health effects. *Environ Health Persp* **1999**, *107*, 409–419.
37. Greenop, K. R.; Peters, S.; Bailey, H. D.; Fritschi, L.; Attia, J.; Scott, R. J.; Glass, D. C.; de Klerk, N. H.; Alvaro, F.; Armstrong, B. K.; Milne, E., Exposure to pesticides and the risk of childhood brain tumors. *Cancer Causes Control* **2013**, *24* (7), 1269–1278.
38. Haynes, D.; Johnson, J. E., Organochlorine, heavy metal and polyaromatic hydrocarbon pollutant concentrations in the Great Barrier Reef (Australia) environment: a review. *Mar Pollut Bull* **2000**, *41* (7-12), 267–278.
39. Vives, I.; Grimalt, J. O.; Ventura, M.; Catalan, J.; Rosseland, B. O., Age dependence of the accumulation of organochlorine pollutants in brown trout (*Salmo trutta*) from a remote high mountain lake (Redó, Pyrenees). *Environ Pollut* **2005**, *133* (2), 343–350.
40. Casida, J. E.; Kimmel, E. C.; Elliott, M.; Janes, N. F., Oxidative metabolism of pyrethrins in mammals. *Nature* **1971**, *230* (5292), 326–327.
41. Isman, M. B.; Koul, O.; Luczynski, A.; Kaminski, J., Insecticidal and antifeedant bioactivities of neem oils and their relationship to azadirachtin content. *J Agr Food Chem* **1990**, *38* (6), 1406–1411.
42. Putter, I.; Connell, G. M.; Preiser, A.; Haidri, A.; Ristich, S. S.; Dybas, R. A., Avermectins: novel insecticides, acaricides and nematocides from a soil microorganism. *Experientia* **1981**, *37* (6), 963–964.
43. Thompson, G. D.; Dutton, R.; Sparks, T. C., Spinosad – a case study: an example from a natural products discovery programme. *Pest Manag Sci* **2000**, *56* (8), 695–702.
44. Höfte, H.; Whiteley, H. R., Insecticidal crystal proteins of *Bacillus thuringiensis*. *Microbiol Rev* **1989**, *53* (2), 242–255.
45. Knowles, B. H., Mechanism of action of *Bacillus thuringiensis* insecticidal δ -endotoxins. *Adv in Insect Physio* **1994**, *24*, 275–308.
46. Tabashnik, B. E.; Brévault, T.; Carrière, Y., Insect resistance to Bt crops: lessons from the first billion acres. *Nat Biotechnol* **2013**, *31* (6), 510–521.
47. Lereclus, D.; Vallade, M.; Chaufaux, J.; Arantes, O.; Rambaud, S., Expansion of insecticidal host range of *Bacillus thuringiensis* by *in vivo* genetic recombination. *Nat Biotechnol* **1992**, *10* (4), 418–421.
48. Herzig, V.; Wood, D. L.; Newell, F.; Chaumeil, P. A.; Kaas, Q.; Binford, G. J.; Nicholson, G. M.; Gorse, D.; King, G. F., ArachnoServer 2.0, an updated online resource for spider toxin sequences and structures. *Nucleic Acids Res* **2011**, *39* (Database issue), D653–D657.
49. Atkinson, R. K.; Howard, M. E. H.; Tyler, M. I.; Vornarx, E. J., Insecticidal toxins derived from funnel web (Atrax or Hadronyche) spiders. *U.S. Patent No. 5763568, 09-JUN-1998*.

50. Wang, X.-h.; Connor, M.; Smith, R.; Maciejewski, M. W.; Howden, M. E. H.; Nicholson, G. M.; Christie, M. J.; King, G. F., Discovery and characterization of a family of insecticidal neurotoxins with a rare vicinal disulfide bridge. *Nat Struct Biol* **2000**, *7* (6), 505–513.
51. King, G. F.; Tedford, H. W.; Maggio, F., Structure and function of insecticidal neurotoxin from Australian funnel-web spiders. *Toxin Reviews* **2002**, *21* (4), 361–389.
52. Hardy, M. C.; Daly, N. L.; Mobli, M.; Morales, R. A.; King, G. F., Isolation of an orally active insecticidal toxin from the venom of an Australian Tarantula. *PLoS ONE* **2013**, *8* (9), e73136.
53. Mukherjee, A. K.; Sollod, B. L.; Wikel, S. K.; King, G. F., Orally active acaricidal peptide toxins from spider venom. *Toxicon* **2006**, *47* (2), 182–187.
54. Lee, J. D.; Park, H. J.; Chae, Y.; Lim, S., An overview of bee venom acupuncture in the treatment of arthritis. *Evid Based Complement Alternat Med* **2005**, *2* (1), 79–84.
55. Qi, J.; Tan, C. K.; Hashimi, S. M.; Zulfiker, A. H. M.; Good, D.; Wei, M. Q., Toad glandular secretions and skin extractions as anti-inflammatory and anticancer agents. *Evid-Based Compl Alt* **2014**, 312684.
56. Craik, D. J.; Fairlie, D. P.; Liras, S.; Price, D., The future of peptide-based drugs. *Chem Biol Drug Des* **2012**, *81* (1), 136–147.
57. Vlieghe, P.; Lisowski, V.; Martinez, J.; Khrestchatsky, M., Synthetic therapeutic peptides: science and market. *Drug Discov Today* **2010**, *15* (1-2), 40–56.
58. Fosgerau, K.; Hoffmann, T., Peptide therapeutics: current status and future directions. *Drug Discov Today* **2015**, *20* (1), 122–128.
59. Kovalainen, M.; Monkare, J.; Riikonen, J.; Pesonen, U.; Vlasova, M.; Salonen, J.; Lehto, V. P.; Jarvinen, K.; Herzig, K. H., Novel delivery systems for improving the clinical use of peptides. *Pharmacol Rev* **2015**, *67* (3), 541–561.
60. Hamzeh-Mivehroud, M.; Alizadeh, A. A.; Morris, M. B.; Church, W. B.; Dastmalchi, S., Phage display as a technology delivering on the promise of peptide drug discovery. *Drug Discov Today* **2013**, *18* (23/24), 1144–1157.
61. Jarvis, L. M., The year in new drugs. *Chem Eng News* **2016**, *94* (51), 12–17.
62. Harvey, A. L., Toxins and drug discovery. *Toxicon* **2014**, *92*, 193–200.
63. Pennington, M. W.; Chang, S. C.; Chauhan, S.; Huq, R.; Tajhya, R. B.; Chhabra, S.; Norton, R. S.; Beeton, C., Development of highly selective Kv1.3-blocking peptides based on the sea anemone peptide ShK. *Mar Drugs* **2015**, *13* (1), 529–542.
64. Dardevet, L.; Rani, D.; Aziz, T. A.; Bazin, I.; Sabatier, J. M.; Fadl, M.; Brambilla, E.; De Waard, M., Chlorotoxin: a helpful natural scorpion peptide to diagnose glioma and fight tumor invasion. *Toxins* **2015**, *7* (4), 1079–1101.
65. Gründer, S.; Pusch, M., Biophysical properties of acid-sensing ion channels (ASICs). *Neuropharmacology* **2015**, *94*, 9–18.
66. Wemmie, J. A.; J. Taugher, R.; J. Kreple, C., Acid-sensing ion channels in pain and disease. *Nat Rev Neurosci* **2013**, *14* (7), 461–471.

67. Kellenberger, S.; Schild, L., International union of basic and clinical pharmacology. XCI. Structure, function, and pharmacology of acid-sensing ion channels and the epithelial Na⁺ channel. *Pharmacol Rev* **2015**, *67* (1), 1–35.
68. Kellenberger, S.; Schild, L., Epithelial sodium channel/degenerin family of ion channels: A variety of functions for a shared structure. *Physiol Rev* **2002**, *82* (3), 735–767.
69. Jasti, J.; Furukawa, H.; Gonzales, E. B.; Gouaux, E., Structure of acid-sensing ion channel 1 at 1.9 Å resolution and low pH. *Nature* **2007**, *449*, 316–323.
70. Carnally, S. M.; Dev, H. S.; Stewart, A. P.; Barrera, N. P.; Van Bemmelen, M. X.; Schild, L.; Henderson, R. M.; Edwardson, J. M., Direct visualization of the trimeric structure of the ASIC1a channel, using AFM imaging. *Biochem Biophys Res Commun* **2008**, *372* (4), 752–755.
71. Lingueglia, E.; de Weille, J. R.; Bassilana, F.; Heurteaux, C.; Sakai, H.; Waldmann, R.; Lazdunski, M., A modulatory subunit of acid sensing ion channels in brain and dorsal root ganglion cells. *J Biol Chem* **1997**, *272* (29778–29783), 29778–83.
72. Baron, A.; Waldmann, R.; Lazdunski, M., ASIC-like, proton-activated currents in rat hippocampal neurons. *J Physiol* **2002**, *539* (Pt 2), 485–494.
73. Benson, C. J.; Xie, J.; Wemmie, J. A.; Price, M. P.; Henss, J. M.; Welsh, M. J.; Snyder, P. M., Heteromultimers of DEG/ENaC subunits form H⁺-gated channels in mouse sensory neurons. *Proc Natl Acad Sci U S A* **2002**, *99* (4), 2338–2343.
74. Yermolaieva, O.; Leonard, A. S.; Schnizler, M. K.; Abboud, F. M.; Welsh, M. J., Extracellular acidosis increases neuronal cell calcium by activating acid-sensing ion channel 1a. *Proc Natl Acad Sci U S A* **2003**, *101* (17), 6752–6757.
75. Askwith, C. C.; Wemmie, J. A.; Price, M. P.; Rokhlina, T.; Welsh, M. J., Acid-sensing ion channel 2 (ASIC2) modulates ASIC1 H⁺-activated currents in hippocampal neurons. *J Biol Chem* **2004**, *279* (18), 18296–18305.
76. Babinski, K.; Catarsi, S.; Biagini, G.; Séguéla, P., Mammalian ASIC2a and ASIC3 subunits co-assemble into heteromeric proton-gated channels sensitive to Gd³⁺. *J Biol Chem* **2000**, *275* (37), 28519–28525.
77. Price, M. P.; Snyder, P. M.; Welsh, M. J., Cloning and expression of a novel human brain Na⁺ channel. *J Biol Chem* **1996**, *271* (14), 7879–7882.
78. Waldmann, R.; Champigny, G.; Voilley, N.; Lauritzen, I.; Lazdunski, M., The Mammalian Degenerin MDEG, an amiloride-sensitive cation channel activated by mutations causing neurodegeneration in *Caenorhabditis elegans*. *J Biol Chem* **1996**, *271* (18), 10433–10436.
79. Waldmann, R.; Champigny, G.; Bassilana, F.; Heurteaux, C.; Lazdunski, M., A proton-gated cation channel involved in acid-sensing. *Nature* **1997**, *386* (6621), 173–177.
80. Chen, X.; Grunder, S., Permeating protons contribute to tachyphylaxis of the acid-sensing ion channel (ASIC) 1a. *J Physiol* **2007**, *579* (Pt 3), 657–670.

81. Wemmie, J. A.; Price, M. P.; Welsh, M. J., Acid-sensing ion channels: advances, questions and therapeutic opportunities. *Trends Neurosci* **2006**, *29* (10), 578–586.
82. Akopian, A. N.; Chen, C. C.; Ding, Y.; Cesare, P.; Wood, J. N., A new member of the acid-sensing ion channel family. *Neuroreport* **2000**, *11* (10), 2217–2222.
83. Bassler, E. L.; Ngo-Anh, T. J.; Geisler, H. S.; Ruppersberg, J. P.; Grunder, S., Molecular and functional characterization of acid-sensing ion channel (ASIC) 1b. *J Biol Chem* **2001**, *276* (36), 33782–33787.
84. Chen, C. C.; England, S.; Akopian, A. N.; Wood, J. N., A sensory neuron-specific, proton-gated ion channel. *Proc Natl Acad Sci U S A* **1998**, *95* (17), 10240–10245.
85. Gründer, S.; Geissler, H.-S.; Bässler, E.-L.; Ruppersberg, P. J., A new member of acid-sensing ion channels from pituitary gland. *NeuroReport* **2000**, *11* (18), 1607–1611.
86. Meng, Q.-Y.; Wang, W.; Chen, X.-N.; Xu, T.-L.; Zhou, J.-N., Distribution of acid-sensing ion channel 3 in the rat hypothalamus. *Neuroscience* **2008**, *159* (3), 1126–1134.
87. Waldmann, R.; Bassilana, F.; Weille, J. d.; Champigny, G.; Heurteaux, C.; Lazdunski, M., Molecular cloning of a non-inactivating proton-gated Na⁺ channel specific for sensory neurons. *J Biol Chem* **1997**, *272* (34), 20975–20978.
88. Gonzales, E. B.; Kawate, T.; Gouaux, E., Pore architecture and ion sites in acid-sensing ion channels and P2X receptors. *Nature* **2009**, *460* (7255), 599–604.
89. Ramaswamy, S. S.; MacLean, D. M.; Gorfe, A. A.; Jayaraman, V., Proton-mediated conformational changes in an acid-sensing ion channel. *J Biol Chem* **2013**, *288* (50), 35896–35903.
90. Sherwood, T. W.; Frey, E. N.; Askwith, C. C., Structure and activity of the acid-sensing ion channels. *Am J Physiol Cell Physiol* **2012**, *303* (7), C699–C710.
91. Bacongus, I.; Gouaux, E., Structural plasticity and dynamic selectivity of acid-sensing ion channel-spider toxin complexes. *Nature* **2012**, *489* (7416), 400–405.
92. Dawson, R. J.; Benz, J.; Stohler, P.; Tetaz, T.; Joseph, C.; Huber, S.; Schmid, G.; Hugin, D.; Pflimlin, P.; Trube, G.; Rudolph, M. G.; Hennig, M.; Ruf, A., Structure of the acid-sensing ion channel 1 in complex with the gating modifier Psalmotoxin 1. *Nat Commun* **2012**, *3*, 936.
93. Bohlen, C. J.; Chesler, A. T.; Sharif-Naeini, R.; Medzihradzky, K. F.; Zhou, S.; King, D.; Sanchez, E. E.; Burlingame, A. L.; Basbaum, A. I.; Julius, D., A heteromeric Texas coral snake toxin targets acid-sensing ion channels to produce pain. *Nature* **2011**, *479* (7373), 410–414.
94. Baron, A.; Lingueglia, E., Pharmacology of acid-sensing ion channels - Physiological and therapeutical perspectives. *Neuropharmacology* **2015**, *94*, 19–35.
95. Chu, X.-P.; Wemmie, J. A.; Wang, W.-Z.; Zhu, X.-M.; Saugstad, J. A.; Price, M. P.; Simon, R. P.; Xiong, Z.-G., Subunit-dependent high-affinity zinc inhibition of acid-sensing ion channels. *J Neurosci* **2003**, *24* (40), 8678–8689.

96. Babini, E.; Paukert, M.; Geisler, H. S.; Gründer, S., Alternative splicing and interaction with di- and polyvalent cations control the dynamic range of acid-sensing ion channel 1 (ASIC1). *J Biol Chem* **2002**, *277* (44), 41597–41603.
97. Immke, D. C.; McCleskey, E. W., Protons open acid-sensing ion channels by catalyzing relief of Ca²⁺ blockade. *Neuron* **2003**, *37* (1), 75–84.
98. Holland, P. R.; Akerman, S.; Andreou, A. P.; Karsan, N.; Wemmie, J. A.; Goadsby, P. J., Acid-sensing ion channel 1: A novel therapeutic target for migraine with aura. *Ann Neurol* **2012**, *72* (4), 559–563.
99. Dubé, G. R.; Lehto, S. G.; Breese, N. M.; Baker, S. J.; Wang, X.; Matulenko, M. A.; Honoré, P.; Stewart, A. O.; Moreland, R. B.; Brioni, J. D., Electrophysiological and in vivo characterization of A-317567, a novel blocker of acid sensing ion channels. *Pain* **2005**, *117* (1–2), 88–96.
100. Voilley, N., Acid-sensing ion channels (ASICs): New targets for the analgesic effects of non-steroid anti-inflammatory drugs (NSAIDs). *Curr Drug Targets Inflamm Allergy* **2004**, *3* (1), 71–76.
101. Mango, D.; Barbato, G.; Piccirilli, S.; Panico, M. B.; Feligioni, M.; Schepisi, C.; Graziani, M.; Porrini, V.; Benarese, M.; Lanzillotta, A.; Pizzi, M.; Pieraccini, S.; Sironi, M.; Blandini, F.; Nicoletti, F.; Mercuri, N. B.; Imbimbo, B. P.; Nisticò, R., Electrophysiological and metabolic effects of CHF5074 in the hippocampus: protection against *in vitro* ischemia. *Pharmacol Res* **2014**, *61*, 83–90.
102. Yu, Y.; Chen, Z.; Li, W.-G.; Cao, H.; Feng, E.-G.; Yu, F.; Liu, H.; Jiang, H.; Xu, T.-L., A nonproton ligand sensor in the acid-sensing ion channel. *Neuron* **2010**, *68* (1), 61–72.
103. Escoubas, P.; De Weille, J. R.; Lecoq, A.; Diochot, S.; Waldmann, R.; Champigny, G.; Moinier, D.; Menez, A.; Lazdunski, M., Isolation of a tarantula toxin specific for a class of proton-gated Na⁺ channels. *J Biol Chem* **2000**, *275* (33), 25116–25121.
104. Saez, N. J.; Mobli, M.; Bier, M.; Chassagnon, I. R.; Malde, A. K.; Gamsjaeger, R.; Mark, A. E.; Gooley, P. R.; Rash, L. D.; King, G. F., A dynamic pharmacophore drives the interaction between Psalmotoxin-1 and the putative drug target acid-sensing ion channel 1a. *Mol Pharmacol* **2011**, *80* (5), 796–808.
105. Sherwood, T. W.; Lee, K. G.; Gormley, M. G.; Askwith, C. C., Heteromeric acid-sensing ion channels (ASICs) composed of ASIC2b and ASIC1a display novel channel properties and contribute to acidosis-induced neuronal death. *J Neurosci* **2011**, *31* (26), 9723–9734.
106. Chen, X.; Kalbacher, H.; Grunder, S., The tarantula toxin psalmotoxin 1 inhibits acid-sensing ion channel (ASIC) 1a by increasing its apparent H⁺ affinity. *J Gen Physiol* **2005**, *126* (1), 71–79.
107. Chen, X.; Kalbacher, H.; Gründer, S., Interaction of Acid-sensing ion channel (ASIC) 1 with the tarantula toxin Psalmotoxin 1 is state dependent. *J Gen Physiol* **2006**, *127* (3), 267–176.
108. Salinas, M.; Rash, L. D.; Baron, A.; Lambeau, G.; Escoubas, P.; Lazdunski, M., The receptor site of the spider toxin PcTx1 on the proton-gated cation channel ASIC1a. *J Physiol* **2006**, *570* (2), 339–354.
109. Qadri, Y. J.; Berdiev, B. K.; Song, Y.; Lipton, H. L.; Fuller, C. M.; Benos, D. J., Psalmotoxin-1 docking to human acid-sensing ion channel-1. *J Biol Chem* **2009**, *284* (26), 17625–17633.
110. Saez, N. J.; Deplazes, E.; Cristofori-Armstrong, B.; Chassagnon, I. R.; Lin, X.; Mobli, M.; Mark, A. E.; Rash, L. D.; King, G. F., Molecular dynamics and functional studies define a hot spot of crystal

- contacts essential for PcTx1 inhibition of acid-sensing ion channel 1a. *Br J Pharmacol* **2015**, *172* (20), 4985–4995.
111. Diochot, S.; Baron, A.; Rash, L. D.; Deval, E.; Escoubas, P.; Scarzello, S.; Salinas, M.; Lazdunski, M., A new sea anemone peptide, APETx2, inhibits ASIC3, a major acid-sensitive channel in sensory neurons. *EMBO J* **2004**, *23* (7), 1516–1525.
112. Blanchard, M. G.; Rash, L. D.; Kellenberger, S., Inhibition of voltage-gated Na(+) currents in sensory neurones by the sea anemone toxin APETx2. *Br J Pharmacol* **2012**, *165* (7), 2167–2177.
113. Peigneur, S.; Béress, L.; Möller, C.; Marí, F.; Forssmann, W.-G.; Tytgat, J., A natural point mutation changes both target selectivity and mechanism of action of sea anemone toxins. *Faseb Journal* **2012**, *26* (12), 5141–5151.
114. Jensen, J. E.; Cristofori-Armstrong, B.; Anangi, R.; Rosengren, K. J.; Lau, C. H.; Mobli, M.; Brust, A.; Alewood, P. F.; King, G. F.; Rash, L. D., Understanding the molecular basis of toxin promiscuity: The analgesic sea anemone peptide APETx2 interacts with acid-sensing ion channel 3 and hERG channels via overlapping pharmacophores. *J Med Chem* **2014**, *57* (21), 9195–9203.
115. Osmakov, D. I.; Kozlov, S. A.; Andreev, Y. A.; Koshelev, S. G.; Sanamyan, N. P.; Sanamyan, K. E.; Dyachenko, I. A.; Bondarenko, D. A.; Murashev, A. N.; Mineev, K. S.; Arseniev, A. S.; Grishin, E. V., Sea Anemone peptide with uncommon β -hairpin structure inhibits acid-sensing ion channel 3 (ASIC3) and reveals analgesic activity. *J Biol Chem* **2013**, *288* (32), 23116–23127.
116. Rodríguez, A. A.; Salceda, E.; Garateix, A. G.; Zaharenko, A. J.; Peigneur, S.; López, O.; Pons, T.; Richardson, M.; Díaz, M.; Hernández, Y.; Ständker, L.; Tytgat, J.; Soto, E., A novel sea anemone peptide that inhibits acid-sensing ion channels. *Peptides* **2014**, *53*, 5–12.
117. Diochot, S.; Baron, A.; Salinas, M.; Douguet, D.; Scarzello, S.; Dabert-Gay, A. S.; Debayle, D.; Friend, V.; Alloui, A.; Lazdunski, M.; Lingueglia, E., Black mamba venom peptides target acid-sensing ion channels to abolish pain. *Nature* **2012**, *490* (7421), 552–555.
118. Baron, A.; Diochot, S.; Salinas, M.; Deval, E.; Noël, J.; Lingueglia, E., Venom toxins in the exploration of molecular, physiological and pathophysiological functions of acid-sensing ion channels. *Toxicon* **2013**, *75*, 187–204.
119. Salinas, M.; Besson, T.; Delettre, Q.; Diochot, S.; Boulakirba, S.; Douguet, D.; Lingueglia, E., Binding site and inhibitory mechanism of the Mambalgin-2 pain-relieving peptide on acid-sensing ion channel 1a. *J Biol Chem* **2014**, *289* (19), 13363–13373.
120. Schroeder, C. I.; Rash, L. D.; Vila-Farrés, X.; Rosengren, K. J.; Mobli, M.; King, G. F.; Alewood, P. F.; Craik, D. J.; Durek, T., Chemical synthesis, 3D structure, and ASIC binding site of the toxin Mambalgin-2. *Angew Chem Int Ed Engl* **2014**, *53* (4), 1017–020.
121. Bacongus, I.; Bohlen, C. J.; Goehring, A.; Julius, D.; Gouaux, E., X-ray structure of acid-sensing ion channel 1-snake toxin complex reveals open state of a Na⁽⁺⁾-selective channel. *Cell* **2014**, *156* (4), 717–729.
122. Diochot, S.; Salinas, M.; Baron, A.; Escoubas, P.; Lazdunski, M., Peptides inhibitors of acid-sensing ion channels. *Toxicon* **2007**, *49* (2), 271–284.

123. Gaskin, D. J.; Richard, P., The Economic Costs of Pain in the United States. In *Relieving Pain in America: A Blueprint for Transforming Prevention, Care, Education, and Research*, Institute of Medicine (US) Committee on Advancing Pain Research, C., and Education, Ed. National Academies Press: Washinton (DC), 2011; pp 301-338.
124. Benyamin, R.; Trescot, A. M.; Datta, S.; Buenaventura, R.; Adlaka, R.; Sehgal, N.; Glaser, S. E.; Vallejo, R., Opioid complications and side effects. *Pain Physician* **2008**, *11* (2 Suppl), S105–S120.
125. Woolf, C. J., Pain: moving from symptom control toward mechanism-specific pharmacologic management. *Ann Intern Med* **2004**, *140* (6), 441–451.
126. Olson, T. H.; Riedl, M. S.; Vulchanova, L.; Ortiz-Gonzalez, X. R.; Elde, R., An acid sensing ion channel (ASIC) localizes to small primary afferent neurons in rats. *NeuroReport* **1998**, *9* (6), 1109–1113.
127. Sutherland, S. P.; Benson, C. J.; Adelman, J. P.; McCleskey, E. W., Acid-sensing ion channel 3 matches the acid-gated current in cardiac ischemia-sensing neurons. *Proc Natl Acad Sci U S A* **2001**, *98* (2), 711–716.
128. Ugawa, S.; Ueda, T.; Ishida, Y.; Nishigaki, M.; Shibata, Y.; Shimada, S., Amiloride-blockable acid-sensing ion channels are leading acid sensors expressed in human nociceptors. *J Clin Invest* **2002** *110* (8), 1185–1190.
129. Jones, N. G.; Slater, R.; Cadiou, H.; McNaughton, P.; McMahon, S. B., Acid-induced pain and Its modulation in humans. *J Neurosci* **2004**, *24* (48), 10974–10979.
130. Mazzuca, M.; Heurteaux, C.; Alloui, A.; Diochot, S.; Baron, A.; Voilley, N.; Blondeau, N.; Escoubas, P.; Gelot, A.; Cupo, A.; Zimmer, A.; Zimmer, A. M.; Eschalier, A.; Lazdunski, M., A tarantula peptide against pain via ASIC1a channels and opioid mechanisms. *Nat Neurosci* **2007**, *10* (8), 943–945.
131. Duan, B.; Wu, L. J.; Yu, Y. Q.; Ding, Y.; Jing, L.; Xu, L.; Chen, J.; Xu, T. L., Upregulation of acid-sensing ion channel ASIC1a in spinal dorsal horn neurons contributes to inflammatory pain hypersensitivity. *J Neurosci* **2007**, *27* (41), 11139–11148.
132. Deval, E.; Noël, J.; Lay, N.; Alloui, A.; Diochot, S.; Friend, V.; Jodar, M.; Lazdunski, M.; Lingueglia, E., ASIC3, a sensor of acidic and primary inflammatory pain. *EMBO J* **2008**, *27* (22), 3047–3055.
133. Xiong, Z.-G.; Chu, X.-P.; Simon, R. P., Ca²⁺-permeable acid-sensing Ion channels and ischemic brain injury. *J Membr Biol* **2006**, *209* (1), 59–68.
134. Xiong, Z.-G.; Zhu, X.-M.; Chu, X.-P.; Minami, M.; Hey, J.; Wei, W.-L.; MacDonald, J. F.; Wemmie, J. A.; Price, M. P.; Welsh, M. J.; Simon, R. P., Neuroprotection in ischemia: blocking calcium-permeable acid-sensing ion channels. *Cell* **2004**, *118* (6), 687–698.
135. Woodruff, T. M.; Thundyil, J.; Tang, S.-C.; Sobey, C. G.; Taylor, S. M.; Arumugam, T. V., Pathophysiology, treatment, and animal and cellular models of human ischemic stroke. *Mol Neurodegener* **2011**, *6* (1), 11.
136. Liu, R.; Yuan, H.; Yuan, F.; Yang, S. H., Neuroprotection targeting ischemic penumbra and beyond for the treatment of ischemic stroke. *Neurol Res* **2013**, *34* (4), 331–337.

137. Prabhakaran, S.; Ruff, I.; Bernstein, R. A., Acute stroke intervention: a systematic review. *JAMA* **2015**, *313* (14), 1451–1462.
138. Mozaffarian, D.; Benjamin, E. J.; Go, A. S.; Arnett, D. K.; Blaha, M. J.; Cushman, M.; Das, S. R.; Ferranti, S. d.; Després, J.-P.; Fullerton, H. J.; Howard, V. J.; Huffman, M. D.; Isasi, C. R.; Jiménez, M. C.; Judd, S. E.; Kissela, B. M.; Lichtman, J. H.; Lisabeth, L. D.; Liu, S.; Mackey, R. H.; Magid, D. J.; McGuire, D. K.; III, E. R. M.; Moy, C. S.; Muntner, P.; Mussolino, M. E.; Nasir, K.; Neumar, R. W.; Nichol, G.; Palaniappan, L.; Pandey, D. K.; Reeves, M. J.; Rodriguez, C. J.; Rosamond, W.; Sorlie, P. D.; Stein, J.; Towfighi, A.; Turan, T. N.; Virani, S. S.; Woo, D.; Yeh, R. W.; Turner, M. B., Heart disease and stroke statistics--2015 update: a report from the American Heart Association. *Circulation* **2015**, *131* (4), e29–e322.
139. O'Bryant, Z.; Vann, K. T.; Xiong, Z. G., Translational strategies for neuroprotection in ischemic stroke—focusing on Acid Sensing Ion Channel 1a. *Transl Stroke Res* **2014**, *5* (1), 59–68.
140. Wardlaw, J. M.; Murray, V.; Berge, E.; Zoppo, G. d.; Sandercock, P.; Lindley, R. L.; Cohen, G., Recombinant tissue plasminogen activator for acute ischaemic stroke: an updated systematic review and meta-analysis. *Lancet* **2012**, *379* (9834), 2364–2372.
141. Pignataro, G.; Simon, R. P.; Xiong, Z.-G., Prolonged activation of ASIC1a and the time window for neuroprotection in cerebral ischaemia *Brain* **2007**, *130* (1), 151–158.
142. McCarthy, C. A.; Rash, L. D.; Chassagnon, I. R.; King, G. F.; Widdop, R. E., PcTx1 affords neuroprotection in a conscious model of stroke in hypertensive rats via selective inhibition of ASIC1a. *Neuropharmacology* **2015**, *99*, 650–657.
143. Kaur, C.; Foulds, W. S.; Ling, E. A., Hypoxia-ischemia and retinal ganglion cell damage. *Clin Ophthalmol* **2008**, *2* (4), 879–889.
144. Ettaiche, M.; Deval, E.; Cougnon, M.; Lazdunski, M.; Voilley, N., Silencing acid-sensing ion channel 1a alters cone-mediated retinal function. *J Neurosci* **2006**, *26* (21), 5800–5809.
145. Tan, J.; Ye, X. H.; Xu, Y. P.; Wang, H.; Sheng, M. J.; Wang, F., Acid-sensing ion channel 1a is involved in retinal ganglion cell death induced by hypoxia. *Mol Vis* **2011**, *17* (354–55), 3300–3308.
146. Hu, R.; Duan, B.; Wang, D.; Yu, Y.; Li, W.; Luo, H.; Lu, P.; Lin, J.; Zhu, G.; Wan, Q.; Feng, H., Role of acid-sensing ion channel 1a in the secondary damage of traumatic spinal cord injury. *Ann Surg* **2011**, *254* (2), 353–362.
147. Prince, M.; Wimo, P. A.; Guerchet, M.; Ali, G.-C.; Wu, Y.-T.; Prina, M. *World Alzheimer Report 2015*; Alzheimer's Disease International London, 2015.
148. Wong, H. K.; Bauer, P. O.; Kurosawa, M.; Goswami, A.; Washizu, C.; Machida, Y.; Tosaki, A.; Yamada, M.; Knopfel, T.; Nakamura, T.; Nukina, N., Blocking acid-sensing ion channel 1 alleviates Huntington's disease pathology via an ubiquitin-proteasome system-dependent mechanism. *Hum Mol Genet* **2008**, *17* (20), 3223–3235.
149. Arias, R. L.; Sung, M. L.; Vasylyev, D.; Zhang, M. Y.; Albinson, K.; Kubek, K.; Kagan, N.; Beyer, C.; Lin, Q.; Dwyer, J. M.; Zaleska, M. M.; Bowlby, M. R.; Dunlop, J.; Monaghan, M., Amiloride is neuroprotective in an MPTP model of Parkinson's disease. *Neurobiol Dis* **2008**, *31* (3), 334–341.

150. Friese, M. A.; Craner, M. J.; Etzensperger, R.; Vergo, S.; Wemmie, J. A.; Welsh, M. J.; Vincent, A.; Fugger, L., Acid-sensing ion channel-1 contributes to axonal degeneration in autoimmune inflammation of the central nervous system. *Nat Med* **2007**, *13* (12), 1483–1489.
151. Vig, P. J. S.; Hearst, S. M.; Shao, Q.; Lopez, M. E., Knockdown of acid-sensing ion channel 1a (ASIC1a) suppresses disease phenotype in SCA1 mouse model. *Cerebellum* **2014**, *13* (4), 479–490.
152. Vergo, S.; Craner, M. J.; Etzensperger, R.; Attfield, K.; Friese, M. A.; Newcombe, J.; Esiri, M.; Fugger, L., Acid-sensing ion channel 1 is involved in both axonal injury and demyelination in multiple sclerosis and its animal model. *Brain* **2011**, *134*, 571–584.
153. Bowen, B. C.; Block, R. E.; Sanchez-Ramos, J.; Pattany, P. M.; Lampman, D. A.; Murdoch, J. B.; Quencer, R. M., Proton MR spectroscopy of the brain in 14 patients with Parkinson disease. *AJNR Am J Neuroradiol* **1995**, *16* (1), 61–68.
154. Pidoplichko, V. I.; Dani, J. A., Acid-sensitive ionic channels in midbrain dopamine neurons are sensitive to ammonium, which may contribute to hyperammonemia damage. *Proc Natl Acad Sci U S A* **2006**, *103* (30), 11376–11380.
155. Wemmie, J. A.; Askwith, C. C.; Laman, E.; Cassell, M. D.; Jr, J. H. F.; Welsh, M. J., Acid-sensing ion channel 1 is localized in brain regions with high synaptic density and contributes to fear conditioning. *J Neurosci* **2003**, *23* (13), 5496–5502.
156. Wemmie, J. A.; Chen, J.; Askwith, C. C.; Hruska-Hageman, A. M.; Price, M. P.; Nolan, B. C.; Yoder, P. G.; Laman, E.; Hoshi, T.; Jr, J. H. F.; Welsh, M. J., The acid-activated ion channel ASIC contributes to synaptic plasticity, learning, and memory. *Neuron* **2002**, *34* (3), 463–477.
157. Wemmie, J. A.; Coryell, M. W.; Askwith, C. C.; Laman, E.; Leonard, S.; Sigmund, C. D.; Welsh, M. J., Overexpression of acid-sensing ion channel 1a in transgenic mice increases acquired fear-related behavior. *Proc Natl Acad Sci U S A* **2004**, *101* (10), 3621–3626.
158. Coryell, M. W.; Wunsch, A. M.; Haenfler, J. M.; Allen, J. E.; Schnizler, M.; Ziemann, A. E.; Cook, M. N.; Dunning, J. P.; Price, M. P.; Rainier, J. D.; Liu, Z.; Light, A. R.; Langbehn, D. R.; Wemmie, J. A., Acid-Sensing Ion Channel-1a in the amygdala, a novel therapeutic target in depression-related behavior. *J Neurosci* **2009**, *29* (17), 5381–5388.
159. Dwyer, J. M.; Rizzo, S. J.; Neal, S. J.; Lin, Q.; Jow, F.; Arias, R. L.; Rosenzweig-Lipson, S.; Dunlop, J.; Beyer, C. E., Acid sensing ion channel (ASIC) inhibitors exhibit anxiolytic-like activity in preclinical pharmacological models. *Psychopharmacology* **2009**, *203* (1), 41–52.
160. Ali, A.; Pillai, K. P.; Ahmad, F. J.; Dua, Y.; Vohora, D., Anticonvulsant effect of amiloride in pentetrazole-induced status epilepticus in mice. *Pharmacol Rep* **2006**, *58* (2), 242–245.
161. Xiong, Z.-G.; Pignataro, G.; Li, M.; Chang, S.-y.; Simon, R. P., Acid-sensing ion channels (ASICs) as pharmacological targets for neurodegenerative diseases. *Curr Opin Pharmacol* **2008**, *8* (1), 25–32.
162. Torre, L. A.; Bray, F.; Siegel, R. L.; Ferlay, J.; Lortet-Tieulent, J.; Jemal, A., Global cancer statistics, 2012. *CA Cancer J Clin* **2015**, *65* (2), 87–108.
163. Gatenby, R. A.; Gillies, R. J., Why do cancers have high aerobic glycolysis? *Nat Rev Cancer* **2004**, *4*, 891–899.

164. Lacroix, M.; Abi-Said, D.; Fourney, D. R.; Gokaslan, Z. L.; Shi, W.; DeMonte, F.; Lang, F. F.; McCutcheon, I. E.; Hassenbusch, S. J.; Holland, E.; Hess, K.; Michael, C.; Miller, D.; Sawaya, R., A multivariate analysis of 416 patients with glioblastoma multiforme: prognosis, extent of resection, and survival. *J Neurosurg* **2001**, *95* (2), 190–198.
165. Bubien, J. K.; Keeton, D. A.; Fuller, C. M.; Gillespie, G. Y.; Reddy, A. T.; Mapstone, T. B.; Benos, D. J., Malignant human gliomas express an amiloride-sensitive Na⁺ conductance. *Am J Physiol* **1999**, *276* (6 Pt 1), C1405–C1410.
166. Berdiev, B. K.; Xia, J.; McLean, L. A.; Markert, J. M.; Gillespie, G. Y.; Mapstone, T. B.; Naren, A. P.; Jovov, B.; Bubien, J. K.; Ji, H. L.; Fuller, C. M.; Kirk, K. L.; Benos, D. J., Acid-sensing ion channels in malignant gliomas. *J Biol Chem* **2003**, *278* (17), 15023–15034.
167. Kapoor, N.; Lee, W.; Clark, E.; Bartoszewski, R.; McNicholas, C. M.; Latham, C. B.; Bebok, Z.; Parpura, V.; Fuller, C. M.; Palmer, C. A.; Benos, D. J., Interaction of ASIC1 and ENaC subunits in human glioma cells and rat astrocytes. *Am J Physiol Cell Physiol* **2011**, *6* (6), C1246–C1259.
168. Ross, S. B.; Fuller, C. M.; Bubien, J. K.; Benos, D. J., Amiloride-sensitive Na⁺ channels contribute to regulatory volume increases in human glioma cells. *Am J Physiol Cell Physiol* **2007**, *293* (3), C1181–C1185.
169. Rooj, A. K.; McNicholas, C. M.; Bartoszewski, R.; Bebok, Z.; Benos, D. J.; Fuller, C. M., Glioma-specific cation conductance regulates migration and cell cycle progression. *J Biol Chem* **2011**, *287* (6), 4053–4065.
170. Gupta, S. C.; Singh, R.; Asters, M.; Liu, J.; Zhang, X.; Pabbidi, M. R.; Watabe; Mo, Y.-Y., Regulation of breast tumorigenesis through acid sensors. *Oncogene* **2015**, 1–10.
171. Renukuntla, J.; Vadlapudi, A. D.; Patel, A.; Boddu, S. H. S.; Mitra, A. K., Approaches for enhancing oral bioavailability of peptides and proteins. *Int J Pharm* **2013**, *447* (1-2), 75–93.
172. Pardridge, W. M., The blood-brain barrier: Bottleneck in brain drug development. *NeuroRX* **2005**, *2* (1), 3–14.
173. Abbott, N. J., Blood-brain barrier structure and function and the challenges for CNS drug delivery. *J Inherit Metab Dis* **2013**, *36* (3), 437–449.
174. Wang, C. K.; Stalmans, S.; Spiegeleer, B. D.; Craik, D. J., Biodistribution of the cyclotide MCoTI-II, a cyclic disulfide-rich peptide drug scaffold. *J Pept Sci* **2016**, *22* (305–310), 305–10.
175. Everts, S., Brain barricade. *Chem Eng News* **2007**, *85* (23), 33–36.
176. Daneman, R.; Prat, A., The blood-brain barrier. *Cold Spring Harb Perspect Biol* **2015**, *7* (1), a020412.
177. Obermeier, B.; Daneman, R.; Ransohoff, R. M., Development, maintenance and disruption of the blood-brain barrier. *Nat Med* **2013**, *19* (12), 1584–1596.
178. Lochhead, J. J.; Thorne, R. G., Intranasal delivery of biologics to the central nervous system. *Adv Drug Deliv Rev* **2012**, *64* (7), 614–628.
179. Bobo, R. H.; Laske, D. W.; Akbasak, A.; Morrison, P. F.; Dedrick, R. L.; Oldfield, E. H., Convection-enhanced delivery of macromolecules in the brain. *Proc Natl Acad Sci U S A* **1994**, *91* (6), 2076–2080.

180. Lajoie, J. M.; Shusta, E. V., Targeting receptor-mediated transport for delivery of biologics across the blood-brain barrier. *Annu Rev Pharmacol Toxicol* **2015**, *55*, 613–631.
181. Lochhead, J. J.; Thorne, R. G., Intranasal drug delivery to the brain. In *Drug Delivery to the Brain*, Hammarlund-Udenaes, M.; Lange, E. d.; Thorne, R. G., Eds. Springer: New York, 2014; pp 401-431.
182. Born, J.; Lange, T.; Kern, W.; McGregor, G. P.; Bickel, U.; Fehm, H. L., Sniffing neuropeptides: a transnasal approach to the human brain. *Nat Neurosci* **2002**, *5* (6), 514–516.
183. Thorne, R. G.; Pronk, G. J.; Padmanabhan, V.; Frey, W. H., 2nd, Delivery of insulin-like growth factor-I to the rat brain and spinal cord along olfactory and trigeminal pathways following intranasal administration. *Neuroscience* **2004**, *127* (2), 481–496.
184. Renner, D. B.; Svitak, A. L.; Gallus, N. J.; Ericson, M. E.; Frey, W. H., 2nd; Hanson, L. R., Intranasal delivery of insulin via the olfactory nerve pathway. *J Pharm Pharmacol* **2012**, *64* (12), 1709–1714.
185. Ross, T. M.; Martinez, P. M.; Renner, J. C.; Thorne, R. G.; Hanson, L. R.; Frey, W. H., 2nd, Intranasal administration of interferon beta bypasses the blood–brain barrier to target the central nervous system and cervical lymph nodes: a non-invasive treatment strategy for multiple sclerosis. *J Neuroimmunol* **2004**, *151* (1-2), 66–77.
186. Thorne, R. G.; Hanson, L. R.; Ross, T. M.; Tung, D.; Frey, W. H., 2nd, Delivery of interferon- β to the monkey nervous system following intranasal administration. *Neuroscience* **2008**, *152* (3), 785–797.
187. Brines, M. L.; Ghezzi, P.; Keenan, S.; Agnello, D.; de Lanerolle, N. C.; Cerami, C.; Itri, L. M.; Cerami, A., Erythropoietin crosses the blood-brain barrier to protect against experimental brain injury. *Proc Natl Acad Sci U S A* **2000**, *97* (19), 10526–10531.
188. Liu, X. F.; Fawcett, J. R.; Thorne, R. G.; DeFor, T. A.; Frey, W. H., 2nd, Intranasal administration of insulin-like growth factor-I bypasses the blood–brain barrier and protects against focal cerebral ischemic damage. *J Neurol Sci* **2001**, *187* (1-2), 91–97.
189. Hanson, L. R.; Roeytenberg, A.; Martinez, P. M.; Coppes, V. G.; Sweet, D. C.; Rao, R. J.; Marti, D. L.; Hoekman, J. D.; Matthews, R. B.; Frey, W. H., 2nd; Panter, S. S., Intranasal deferoxamine provides increased brain exposure and significant protection in rat ischemic stroke. *J Pharmacol Exp Ther* **2009**, *330* (3), 679–686.
190. Novak, V.; Milberg, W.; Hao, Y.; Munshi, M.; Novak, P.; Galica, A.; Manor, B.; Roberson, P.; Craft, S.; Abduljalil, A., Enhancement of vasoreactivity and cognition by intranasal insulin in Type 2 Diabetes. *Diabetes Care* **2014**, *37* (3), 751–759.
191. Reger, M. A.; Watson, G. S.; Frey, W. H., 2nd; Baker, L. D.; Cholerton, B.; Keeling, M. L.; Belongia, D. A.; Fishel, M. A.; Plymate, S. R.; Schellenberg, G. D.; Cherrier, M. M.; Craft, S., Effects of intranasal insulin on cognition in memory-impaired older adults: Modulation by APOE genotype. *Neurobiol Aging* **2006**, *27* (3), 451–458.
192. Kosfeld, M.; Heinrichs, M.; Zak, P. J.; Fischbacher, U.; Fehr, E., Oxytocin increases trust in humans. *Nature* **2005**, *435* (7042), 673–676.

193. Rilling, J. K.; DeMarco, A. C.; Hackett, P. D.; Thompson, R.; Ditzen, B.; Patelh, R.; Pagnoni, G., Effects of intranasal oxytocin and vasopressin on cooperative behavior and associated brain activity in men. *Psychoneuroendocrinology* **2012**, *37* (4), 447–461.
194. Lalatsa, A.; Schatzlein, A. G.; Uchegbu, I. F., Strategies to deliver peptide drugs to the brain. *Mol Pharm* **2014**, *11* (4), 1081–1093.
195. Jansson, B.; Björk, E., Visualization of *in vivo* olfactory uptake and transfer using fluorescein dextran. *J Drug Target* **2002**, *10* (5), 379–386.
196. Boyer, S.; Zhang, H.; Lemperiere, G., A review of control methods and resistance mechanisms in stored-product insects. *Bull Entomol Res* **2012**, *102* (2), 213–229.
197. Smith, J. J.; Herzig, V.; King, G. F.; Alewood, P. F., The insecticidal potential of venom peptides. *Cell Mol Life Sci* **2013**, *70* (19), 3665–3693.
198. Cantrell, C. L.; Dayan, F. E.; Duke, S. O., Natural products as sources for new pesticides. *J. Nat. Prod* **2012**, *75* (6), 1231–1242.
199. Hardy, M. C., Isolation and characterization of orally active insecticidal peptides from spider venoms. (*Doctoral dissertation*), Retrieved from <https://espace.library.uq.edu.au/> **2011**.
200. King, G. F.; Hardy, M. C., Pest-controlling agents isolated from spider venom and uses thereof. . *Patent No. WO2013026105 (A1)*, 28-FEB-2013.
201. Gentz, M. C.; Jones, A.; Clement, H.; King, G. F., Comparison of the peptidome and insecticidal activity of venom from a taxonomically diverse group of theraphosid spiders. *Toxicon* **2009**, *53* (5), 496–502.
202. Klint, J. K.; Senff, S.; Saez, N. J.; Seshadri, R.; Lau, H. Y.; Bende, N. S.; Undheim, E. A.; Rash, L. D.; Mobli, M.; King, G. F., Production of recombinant disulfide-rich venom peptides for structural and functional analysis via expression in the periplasm of *E. coli*. *PLoS ONE* **2013**, *8* (5), e63865.
203. Mobli, M.; Stern, A. S.; Bermel, W.; King, G. F.; Hoch, J. C., A non-uniformly sampled 4D HCC(CO)NH-TOCSY experiment processed using maximum entropy for rapid protein sidechain assignment. *J Magn Reson* **2010**, *204* (1), 160–164.
204. Shen, Y.; Delaglio, F.; Cornilescu, G.; Bax, A., TALOS+: a hybrid method for predicting protein backbone torsion angles from NMR chemical shifts. *J Biomol NMR* **2009**, *44* (4), 213–233.
205. Guntert, P., Automated NMR structure calculation with CYANA. *Methods Mol Biol* **2004**, *278*, 353–78.
206. Fletcher, J. I.; Smith, R.; O'Donoghue, S. I.; Nilges, M.; Connor, M.; Howden, M. E. H.; Christie, M. J.; King, G. F., The structure of a novel insecticidal neurotoxin, omega-atracotoxin-HV1, from the venom of an Australian funnel web spider. *Nat Struct Biol* **1997**, *4* (7), 559-566.
207. Kapust, R. B.; Tözsér, J.; Copeland, T. D.; Waugh, D. S., The P1' specificity of tobacco etch virus protease. *Biochem Biophys Res Commun* **2002**, *294* (5), 949–955.
208. Bartels, C.; Xia, T. H.; Billeter, M.; Guntert, P.; Wuthrich, K., The program XEASY for computer-supported NMR spectral analysis of biological macromolecules. *J Biomol NMR* **1995**, *6* (1), 1–10.

209. Chen, V. B.; Arendall, W. B., 3rd; Headd, J. J.; Keedy, D. A.; Immormino, R. M.; Kapral, G. J.; Murray, L. W.; Richardson, J. S.; Richardson, D. C., MolProbity: all-atom structure validation for macromolecular crystallography. *Acta Crystallogr D Biol Crystallogr* **2010**, *66* (Pt 1), 12–21.
210. Chen, J.; Deng, M.; He, Q.; Meng, E.; Jiang, L.; Liao, Z.; Rong, M.; Liang, S., Molecular diversity and evolution of cystine knot toxins of the tarantula *Chilobrachys jingzhao*. *Cell Mol Life Sci* **2008**, *65* (15), 2431–2444.
211. Nason, D. M. I.; Phillips, D.; Saccomano, N. A.; Volkmann, R. A., Calcium channel blocking polypeptides from theraphosidae aphonopelma. *Patent No. WO1994010196, 11-MAY-2013*.
212. Liang, S., An overview of peptide toxins from the venom of the Chinese bird spider *Selenocosmia huwena* Wang [= *Ornithoctonus huwena* (Wang)]. *Toxicon* **2004**, *43* (5), 575–585.
213. Holm, L.; Rosenstrom, P., Dali server: conservation mapping in 3D. *Nucleic Acids Res* **2010**, *38* (Web Server issue), W545–W549.
214. Peng, K.; Shu, Q.; Liu, Z.; Liang, S., Function and solution structure of huwentoxin-IV, a potent neuronal tetrodotoxin (TTX)-sensitive sodium channel antagonist from Chinese bird spider *J Biol Chem* **2002**, *277* (49), 47564–47571.
215. Suchyna, T. M.; Johnson, J. H.; Hamer, K.; Leykam, J. F.; Gage, D. A.; Clemo, H. F.; Baumgarten, C. M.; Sachs, F., Identification of a peptide toxin from *Grammostola spatulata* spider venom that blocks cation-selective stretch-activated channels. *J Gen Physiol* **2000**, *115* (5), 583–598.
216. Redaelli, E.; Cassulini, R. R.; Silva, D. F.; Clement, H.; Schiavon, E.; Zamudio, F. Z.; Odell, G.; Arcangeli, A.; Clare, J. J.; Alagón, A.; Vega, R. C. R. d. I.; Possani, L. D.; Wanke, E., Target promiscuity and heterogeneous effects of tarantula venom peptides affecting Na⁺ and K⁺ ion channels. *J Biol Chem* **2010**, *285* (6), 4130–4142.
217. Merrifield, R. B., Solid phase peptide synthesis. I. The synthesis of a tetrapeptide. *J Am Chem Soc* **1963**, *85* (14), 2149–2154.
218. Inaba, K., Disulfide bond formation system in *Escherichia coli*. *J Biol Chem* **2009**, *146* (5), 591–597.
219. Pal, N.; Yamamoto, T.; King, G. F.; Waite, C.; Bonning, B., Aphicidal efficacy of scorpion- and spider-derived neurotoxins. *Toxicon* **2013**, *70*, 114–122.
220. Fitches, E. C.; Pyati, P.; King, G. F.; Gatehouse, J. A., Fusion to snowdrop lectin magnifies the oral activity of insecticidal omega-Hexatoxin-Hv1a peptide by enabling its delivery to the central nervous system. *PLoS ONE* **2012**, *7* (6), e39389.
221. Nakasu, E. Y. T.; Edwards, M. G.; Fitches, E.; Gatehouse, J. A.; Gatehouse, A. M. R., Transgenic plants expressing ω-ACTX-Hv1a and snowdrop lectin (GNA) fusion protein show enhanced resistance to aphids. *Front Plant Sci* **2014**, *5* (673).
222. Sattler, M.; Schleucher, J.; Griesinger, C., Heteronuclear multidimensional NMR experiments for the structure determination of proteins in solution employing pulsed field gradients. *Prog Nucl Mag Res Sp* **1999**, *34* (2), 93–158.

223. Chow, C. Y.; Cristofori-Armstrong, B.; Undheim, E. A.; King, G. F.; Rash, L. D., Three peptide modulators of the human voltage-gated sodium channel 1.7, an important analgesic target, from the venom of an Australian tarantula. *Toxins* **2015**, *7* (7), 2494–2513.
224. Sermadiras, I.; Revell, J.; Linley, J. E.; Sandercock, A.; Ravn, P., Recombinant expression and *in vitro* characterization of active Huwentoxin-IV. *PLoS ONE* **2013**, *8* (12), e83202.
225. Huang, R. H.; Liu, Z. H.; Liang, S. P., Purification and characterization of a neurotoxic peptide huwentoxin-III and a natural inactive mutant from the venom of the spider *Selenocosmia huwena* Wang (Ornithoctonus huwena Wang). *Sheng Wu Hua Xue Yu Sheng Wu Wu Li Xue Bao* **2003**, *35* (11), 976–980.
226. Simons, C.; Rash, L. D.; Crawford, J.; Ma, L.; Cristofori-Armstrong, B.; Miller, D.; Ru, K.; Baillie, G. J.; Alanay, Y.; Jacquinet, A.; Debray, F.-G.; Verloes, A.; Shen, J.; Yesil, G.; Guler, S.; Yuksel, A.; Cleary, J. G.; Grimmond, S. M.; McGaughran, J.; King, G. F.; Gabbett, M. T.; Taft, R. J., Mutations in the voltage-gated potassium channel gene KCNH1 cause Temple-Baraitser syndrome and epilepsy. *Nat Genet* **2015**, *47*, 73–77.
227. Drenth, J. P.; Waxman, S. G., Mutations in sodium-channel gene SCN9A cause a spectrum of human genetic pain disorders. *J Clin Invest* **2007**, *117* (12), 3603–3609.
228. Lyons, S. A.; O'Neal, J.; Sontheimer, H., Chlorotoxin, a scorpion-derived peptide, specifically binds to gliomas and tumors of neuroectodermal origin. *Glia* **2002**, *39* (2), 162–173.
229. Saez, N. J.; Senff, S.; Jensen, J. E.; Er, S. Y.; Herzig, V.; Rash, L. D.; King, G. F., Spider-venom peptides as therapeutics. *toxins* **2010**, *2* (12), 2851–2871.
230. Alavijeh, M. S.; Chishty, M.; Qaiser, M. Z.; Palmer, A. M., Drug metabolism and pharmacokinetics, the blood-brain barrier, and central nervous system drug discovery. *NeuroRx* **2005**, *2* (4), 554–571.
231. Suenderhauf, C.; Hammann, F.; Huwyler, J., Computational prediction of blood-brain barrier permeability using decision tree induction *Molecules* **2012**, *17* (9), 10429–10445.
232. Richter, M.; Yumul, R.; Saydaminova, K.; Wang, H.; Gough, M.; Baldessari, A.; Cattaneo, R.; Lee, F.; Wang, C.-H. K.; Jang, H.; Astier, A.; Gopal, A.; Carter, D.; Lieber, A., Preclinical safety, pharmacokinetics, pharmacodynamics, and biodistribution studies with Ad35K++ protein: a novel rituximab cotherapeutic. *Mol Ther Methods Clin Dev* **2015**, *5* (16013).
233. Gambhir, S. S., Molecular imaging of cancer with positron emission tomography. *Nat Rev Cancer* **2002**, *2* (9), 683–693.
234. Reddy, S.; Robinson, M. K., Immuno-positron emission tomography in cancer models. *Semin Nucl Med* **2010**, *40* (3), 182–189.
235. Schambach, S. J.; Bag, S.; Schilling, L.; Groden, C.; Brockmann, M. A., Application of micro-CT in small animal imaging. *Methods* **2010**, *50* (1), 2–13.
236. Duyn, J. H., The future of ultra-high field MRI and fMRI for study of the human brain. *NeuroImage* **2012**, *62* (2), 1241–1248.

237. Kapoor, V.; McCook, B. M.; Torok, F. S., An Introduction to PET-CT Imaging. *Radiographics* **2004**, *24* (2), 523–543.
238. Rosenkrantz, A. B.; Friedman, K.; Chandarana, H.; Melsaether, A.; Moy, L.; Ding, Y.-S.; Jhaveri, K.; Beltran, L.; Jain, R., Current status of hybrid PET/MRI in oncologic imaging. *AJR Am J Roentgenol* **2016**, *206* (1), 162–172.
239. Vaquero, J. J.; Kinahan, P., Positron emission tomography: Current challenges and opportunities for technological advances in clinical and preclinical imaging systems. *Annu Rev Biomed Eng* **2015**, *17*, 385–414.
240. Koba, W.; Jelicks, L. A.; Fine, E. J., MicroPET/SPECT/CT imaging of small animal models of disease. *Am J Pathol* **2013**, *182* (2), 319–324.
241. Sevick-Muraca, E. M., Translation of near-infrared fluorescence imaging technologies: emerging clinical applications. *Annu Rev Med* **2012**, *63*, 217–231.
242. Testa, B.; Crivori, P.; Reist, M.; Carrupt, P.-A., The influence of lipophilicity on the pharmacokinetic behavior of drugs: Concepts and examples. *Perspect Drug Discov* **2000**, *19* (1), 179–211.
243. Judenhofer, M. S.; Wehrl, H. F.; Newport, D. F.; Catana, C.; Siegel, S. B.; Becker, M.; Thielscher, A.; Kneilling, M.; Lichy, M. P.; Eichner, M.; Klingel, K.; Reischl, G.; Widmaier, S.; Rocken, M.; Nutt, R. E.; Machulla, H. J.; Uludag, K.; Cherry, S. R.; Claussen, C. D.; Pichler, B. J., Simultaneous PET-MRI: a new approach for functional and morphological imaging. *Nat Med* **2008**, *14* (4), 459–465.
244. Kidwell, C. S.; Chalela, J. A.; Saver, J. L.; Starkman, S.; Hill, M. D.; Demchuk, A. M.; Butman, J. A.; Patronas, N.; Alger, J. R.; Latour, L. L.; Luby, M. L.; Baird, A. E.; Leary, M. C.; Tremwel, M.; Ovbiagele, B.; Fredieu, A.; Suzuki, S.; Villablanca, J. P.; Davis, S.; Dunn, B.; Todd, J. W.; Ezzeddine, M. A.; Haymore, J.; Lynch, J. K.; Davis, L.; Warach, S., Comparison of MRI and CT for detection of acute intracerebral hemorrhage. *JAMA* **2004**, *292* (15), 823–1830.
245. Shenton, M.; Hamoda, H.; Schneiderman, J.; Bouix, S.; Pasternak, O.; Rathi, Y.; M-A, V.; Purohit, M.; Helmer, K.; Koerte, I.; Lin, A.; C-F, W.; Kikinis, R.; Kubicki, M.; Stern, R.; Zafonte, R., A review of magnetic resonance imaging and diffusion tensor imaging findings in mild traumatic brain injury. *Brain Imaging Behav* **2012**, *6* (2), 137–192.
246. Qi, D.; Scholthof, K. B., A one-step PCR-based method for rapid and efficient site-directed fragment deletion, insertion, and substitution mutagenesis. *J Virol Methods* **2008**, *149* (1), 85–90.
247. Alewood, P.; Alewood, D.; Miranda, L.; Love, S.; Meutermans, W.; Wilson, D., Rapid *in situ* neutralization protocols for Boc and Fmoc solid-phase chemistries. *Methods Enzymol* **1997**, *289*, 14–29.
248. Meldal, M.; Tornøe, C. W., Cu-catalyzed azide–alkyne cycloaddition. *Chem Rev* **2008**, *108* (8), 2952–3015.
249. Agard, N. J.; Prescher, J. A.; Bertozzi, C. R., A strain-promoted [3 + 2] azide–alkyne cycloaddition for covalent modification of biomolecules in living systems. *J Am Chem Soc* **2004**, *126* (46), 15046–150467.

250. Schneider, C. A.; Rasband, W. S.; Eliceiri, K. W., NIH Image to ImageJ: 25 years of image analysis. *Nat Methods* **2012**, *9* (7), 671–675.
251. Hunter, W. M.; Greenwood, F. C., Preparation of iodine-131 labelled human growth hormone of high specific activity. *Nature* **1962**, *194*, 495–496.
252. Koehler, L.; Gagnon, K.; McQuarrie, S.; Wuest, F., Iodine-124: A promising positron emitter for organic PET chemistry *Molecules* **2010**, *15* (4), 2686–2718.
253. Ramachandran, L. K., Protein-Iodine interaction. *Chem Rev* **1956**, *56* (2), 199–218.
254. Gemmill, C. L., The iodination of phenolic compounds related to thyroxine. *Arch Biochem Biophys* **1956**, *63* (1), 177–191.
255. De Leon-Rodriguez, L. M.; Kovacs, Z., The synthesis and chelation chemistry of DOTA-peptide conjugates. *Bioconjug Chem* **2008**, *2008* (19), 2.
256. Kittigowittana, K.; Yang, C. T.; Cheah, W. C.; Chuang, K. H.; Tuang, C. Y.; Chang, Y. T.; Golay, X.; Bates, R. W., Development of intravascular contrast agents for MRI using gadolinium chelates. *ChemMedChem* **2011**, *6* (781–787), 781-787.
257. Hawe, A.; Poole, R.; Romeijn, S.; Kasper, P.; van der Heijden, R.; Jiskoot, W., Towards heat-stable oxytocin formulations: Analysis of degradation kinetics and identification of degradation products. *Pharm Res* **2009**, *26* (7), 1679–1688.
258. de Araujo, A. D.; Mobli, M.; Castro, J.; Harrington, A. M.; Vetter, I.; Dekan, Z.; Muttenthaler, M.; Wan, J. J.; Lewis, R. J.; King, G. F.; Brierley, S. M.; Alewood, P. F., Selenoether oxytocin analogues have analgesic properties in a mouse model of chronic abdominal pain. *Nat Commun* **2014**, *5*, 3165.
259. Kikuchi, K.; Sugiura, M.; Kimura, T., High proteolytic resistance of spider-derived inhibitor cystine knots. *Int J Pept* **2015**, *2015* (537508), 537508.
260. Bongers, J.; Heimer, E. P.; Lambros, T.; Pan, Y. C.; Campbell, R. M.; Felix, A. M., Degradation of aspartic acid and asparagine residues in human growth hormone-releasing factor. *Int J Pept Protein Res* **1992**, *39* (4), 364–374.
261. Werle, M.; Bernkop-Schnürch, A., Strategies to improve plasma half life time of peptide and protein drugs. *Amino Acids* **2006**, *4* (4), 351–367.
262. Neumann, E.; Frei, E.; Funk, D.; Becker, M. D.; Schrenk, H. H.; Muller-Ladner, U.; Fiehn, C., Native albumin for targeted drug delivery. *Expert Opin Drug Del* **2010**, *7* (8), 915–925.
263. Dennis, M. S.; Zhang, M.; Meng, Y. G.; Kadkhodayan, M.; Kirchhofer, D.; Combs, D.; Damico, L. A., Albumin binding as a general strategy for improving the pharmacokinetics of proteins. *J Biol Chem* **2002**, *277* (38), 35035–35043.
264. Levy, O. E.; Jodka, C. M.; Ren, S. S.; Mamedova, L.; Sharma, A.; Samant, M.; D'Souza, L. J.; Soares, C. J.; Yuskin, D. R.; Jin, L. J.; Parkes, D. G.; Tatarkiewicz, K.; Ghosh, S. S., Novel exenatide analogs with peptidic albumin binding domains: potent anti-diabetic agents with extended duration of action. *PLoS ONE* **2014**, *9* (2), e87704.

265. Zuiderweg, E. R., Mapping protein-protein interactions in solution by NMR spectroscopy. *Biochemistry* **2002**, *41* (1), 1–7.
266. Dohân, O.; De la Vieja, A.; Paroder, V.; Riedel, C.; Artani, M.; Reed, M.; Ginter, C. S.; Carrasco, N., The sodium/iodide Symporter (NIS): characterization, regulation, and medical significance. *Endocr Rev* **2003**, *24* (1), 48–77.
267. Groot-Wassink, T.; Aboagye, E. O.; Wang, Y.; Lemoine, N. R.; Reader, A. J.; Vassaux, G., Quantitative imaging of Na/I symporter transgene expression using positron emission tomography in the living animal. *Mol Ther* **2004**, *9* (3), 436–442.
268. Bhise, S. B.; Yadav, A. V.; Avachat, A. M.; Malayandi, R., Bioavailability of intranasal drug delivery system. *Asian J. Pharmacol* **2008**, *2* (4), 201–215.